Universität Bonn

Physikalisches Institut

Search for MSSM Higgs Bosons in Di-τ Final States with the ATLAS Experiment

Christoph Anders

A search for neutral MSSM Higgs bosons decaying into a τ lepton pair, $A/H/h \to \tau^+\tau^-$, is presented. The search is based on proton–proton collision events recorded with the ATLAS detector at the Large Hadron Collider at a center-of-mass energy $\sqrt{s} = 7$ TeV, corresponding to an integrated luminosity of 2.1 fb^{-1}. One of the τ leptons is reconstructed in a leptonic, the other in a hadronic final state. The contributions of the main background processes have been estimated using data driven methods. For the $Z/\gamma^* \to \tau^+\tau^-$ background an embedding method has been used, that replaces the muons in reconstructed $Z/\gamma^* \to \mu^+\mu^-$ events with simulated τ leptons. The event yield of the W + jets background has been studied in a sideband control region and the simulation has been normalized to agree with the sideband data. The contribution from QCD multi-jet processes has been estimated from three data control regions. Systematic uncertainties due to these background estimates have been identified and studied as well as systematic uncertainties affecting the simulated signal and background event samples. The dominating systematic uncertainty has been found to be due to the uncertainty on the energy scales of jets and hadronically decaying τ leptons. In total 4065 data events have been selected and the number of expected events from Standard Model background processes has been estimated to be $4151 \pm 66 \pm 796$, where the first error is statistical and the second error is systematic. As no excess over the Standard Model expectation is found, exclusion limits at the 95% confidence level are set on the production cross section of a generic Higgs boson, Φ, in dependence of its mass and on the production of the neutral MSSM Higgs bosons $A/H/h$ as a function of the parameters $\tan\beta$ and m_A in the $m_h^{\max}$ scenario. These exclusion limits represent significant improvements over those obtained by similar searches of other experiments at LEP and the Tevatron.

Physikalisches Institut der
Universität Bonn
Nußallee 12
D-53115 Bonn

BONN-IR-2013-02
February 2013
ISSN-0172-8741

Universität Bonn

Physikalisches Institut

Search for MSSM Higgs Bosons in Di-τ Final States with the ATLAS Experiment

Christoph Anders
aus Dresden

Dieser Forschungsbericht wurde als Dissertation von der Mathematisch-Naturwissenschaftlichen Fakultät der Universität Bonn angenommen und ist auf dem Hochschulschriftenserver der ULB Bonn `http://hss.ulb.uni-bonn.de/diss_online` elektronisch publiziert.

1. Gutachter:	Prof. Dr. Jochen Dingfelder
2. Gutachter:	Prof. Dr. Klaus Desch
Tag der Promotion:	18.12.2012

Contents

Chapter 1

Introduction

For decades the Standard Model of Particle Physics has been studied and tested extensively. It describes the fundamental particles and the forces acting on them, except for gravity. The forces or interactions are the electromagnetic force, known from everyday life, and the weak and the strong interactions, the source of radioactive decays and the force holding together the nuclei, respectively. The particles of the Standard Model that have been observed by experiments are the quarks (up, down, charm, strange, bottom and top), the leptons (electron, muon, tau, electron neutrino, muon neutrino, tau neutrino) and the gauge bosons that are the mediator particles of the forces. The gauge bosons are the photon, the W and Z bosons and the gluons, mediating the electromagnetic, the weak and the strong interaction, respectively.

Since the discovery of the top quark in 1995 [1, 2] and the tau neutrino in 2000 [3], the Higgs boson has been the last missing piece predicted by the Standard Model. The very recent discovery of a particle [4, 5] that is compatible with a Standard Model Higgs boson at the Large Hadron Collider ("LHC") at CERN[1] promises to complete the Standard Model. The Higgs boson is a central particle in the Standard Model as its existence is a direct consequence of electroweak symmetry breaking, the mechanism that can explain the origin of the masses of the fundamental particles.

Albeit the success of the Standard Model in describing experimental data, it is believed to be an effective theory that may not be valid at energies much higher than those probed so far. Therefore, extensions of the Standard Model that can overcome its shortcomings have been proposed by theorists, and evidence for their existence has been searched for by experiments for decades. A popular extension is the concept of Supersymmetry. Introducing new particles as partners to the Standard Model ones, Supersymmetry could solve many problems of the Standard Model and it also provides a promising candidate particle for cold dark matter, which is known to exist from astrophysical measurements, but cannot be explained within the Standard Model. The Higgs sector in Supersymmetry is more complex than in the Standard Model: Five Higgs bosons are expected, three neutral and two charged ones. Interestingly in many Supersymmetry models, one of the neutral Higgs bosons preferentially couples to down-type[2] particles and therefore searches for supersymmetric Higgs bosons in final states with e.g. tau leptons or b quarks are very promising.

In this thesis, a search for neutral Higgs bosons in the Minimal Supersymmetric Standard Model with the ATLAS detector at the Large Hadron Collider is described. As backgrounds from QCD processes to final states including b quarks have large cross sections for proton–proton collisions at the Large Hadron Collider, final states with pairs of tau leptons are analyzed. In the analysis, no requirement on the number of (b) jets in the event is made.

The work presented in this thesis has been an important part of the first ATLAS analysis [6] using LHC data (equivalent to an integrated luminosity of 36 pb^{-1}) published on the topic and of an update

[1] European Organization for Nuclear Research, located near Geneva, Switzerland.

[2] These are the down, strange and bottom quarks and the electron, muon and tau leptons in the Standard Model.

from summer 2011 [7] that used a larger dataset (1fb^{-1}). The analysis presented in this thesis is based on data equivalent to an integrated luminosity of 2.1fb^{-1}.

This thesis starts with a description of the Standard Model of Particle Physics, the Minimal Supersymmetric Standard Model and its Higgs sector in Chapter 2. The experimental environment, the used datasets and relevant physics processes are described in Chapter 3 and 4. In Chapter 5, the event selection applied to the data is described. The understanding and estimation of the different background processes using data control regions, a main part of all particle physics analyses, is described in Chapter 6. Systematic uncertainties that affect the results are discussed and evaluated in Chapter 7. In Chapter 8, the statistical interpretation of the analysis is introduced and the resulting exclusion limits are presented. Results from similar searches at other experiments and at ATLAS are given. A summary of the measurement performed in this thesis is given in Chapter 9.

Chapter 2

Theory

The theoretical framework describing particle physics phenomena, the Standard Model, is one of the most successful theories in physics, that has withstood decades of intense testing and still holds. It describes the interactions of the fundamental spin $s = \frac{1}{2}$ fermions, the quarks and leptons (see Table 2.1). The interactions are mediated by spin $s = 1$ bosons, the massless photon and gluons for the electromagnetic and the strong interaction, respectively, and the massive $W^{\pm}$ and Z^0 bosons for the weak interaction. Gravity, the forth known force, is negligible for most particle physics phenomena and is not included. While the Standard Model describes the phenomena at the energy scales accessible at present it is known not to be valid at higher scales and that the electroweak symmetry needs to be broken somehow. The Higgs mechanism is the easiest and most popular way to achieve this. It predicts an observable Higgs boson that has not been proven to exist yet and is actively searched for at the LHC.

In the following a short overview of the Standard Model is given and the Higgs mechanism is introduced.

Some shortcomings of the Standard Model will be discussed and one of its most popular extensions, Supersymmetry, will be briefly introduced, focusing on the Minimal Supersymmetric Standard Model ("MSSM") and its Higgs sector.

Finally, the phenomenology of physics at a hadron collider, i.e. the LHC, will be introduced.

As the theory of particle physics is a very diverse field only the aspects important for the search described in this thesis will be focused on. A good overview of the electroweak symmetry breaking mechanism and Higgs boson physics is given in [8, 9], which is used as a guideline here.

	Electric	1st Generation		2nd Generation		3rd Generation	
	Charge	Name	Symbol	Name	Symbol	Name	Symbol
Quarks	$2/3e$	up	u	charm	c	top	t
	$-1/3e$	down	d	strange	s	bottom	b
Leptons	0	electron neutrino	ν_e	muon neutrino	ν_μ	tau neutrino	ν_τ
	$-1e$	electron	e	muon	μ	tau	τ

Table 2.1: The fermions of the Standard Model.

2.1 The Standard Model of Particle Physics

The electroweak theory by Glashow, Weinberg and Salam, describes the electromagnetic and weak interactions between quarks and leptons and is a Yang-Mills theory based on the SU(2)×U(1) symmetry group.

In combination with the SU(3) based quantum chromodynamics ("QCD"), which describes strong interactions, it provides the framework of the Standard Model.

Before electroweak symmetry breaking there are two kinds of fields in the Standard Model:

- The matter fields: Three generations of left and right-handed chiral quarks and leptons, $f_{L,R} = \frac{1}{2}(1 \mp \gamma_5)f$, with the left-handed ones in weak isospin doublets and the right-handed ones in isospin singlets:

$$I_f^{3L,3R} = \pm\frac{1}{2}, 0 \qquad \begin{aligned} L_1 &= \begin{pmatrix} \nu_e \\ e^- \end{pmatrix}, e_{R_1} = e_R^-, Q_1 = \begin{pmatrix} u \\ d \end{pmatrix}, u_{R_1} = u_R, d_{R_1} = d_R \\ L_2 &= \begin{pmatrix} \nu_\mu \\ \mu^- \end{pmatrix}, e_{R_2} = \mu_R^-, Q_2 = \begin{pmatrix} c \\ s \end{pmatrix}, u_{R_2} = c_R, d_{R_2} = s_R \\ L_3 &= \begin{pmatrix} \nu_\tau \\ \tau^- \end{pmatrix}, e_{R_3} = \tau_R^-, Q_3 = \begin{pmatrix} t \\ b \end{pmatrix}, u_{R_3} = t_R, d_{R_3} = b_R \end{aligned} \tag{2.1}$$

(2.2)

  With the third component of the weak isospin $I_{f,3}$ and the electric charge Q_f[1] defining the fermion hypercharge

$$Y_f = 2Q_f - 2I_{f,3}. \tag{2.3}$$

  This leads to $\sum_f Y_f = \sum_f Q_f = 0$, which is important for the renormalizability of the electroweak theory.

  In QCD quarks are grouped in color triplets, while leptons form color singlets under $SU(3)_C$ and therefore only quarks take part in the strong interaction.

- The gauge fields: These correspond to the spin $s = 1$ bosons mediating the forces. In the electroweak sector there are the three fields, $W_\mu^{1,2,3}$, corresponding to the generators T^a (with $a = 1, 2, 3$) of the $SU(2)_L$ group, given by the Pauli matrices multiplied by $\frac{1}{2}$:

$$T^a = \frac{1}{2}\sigma^a; \quad \sigma^1 = \begin{pmatrix} 0 & 1 \\ 1 & 0 \end{pmatrix}, \quad \sigma^2 = \begin{pmatrix} 0 & -i \\ i & 0 \end{pmatrix}, \quad \sigma^3 = \begin{pmatrix} 1 & 0 \\ 0 & -1 \end{pmatrix} \tag{2.4}$$

  and the field B_μ corresponding to the generator Y of the $U(1)_Y$ group. The commutation relations are

$$\left[T^a, T^b\right] = i\epsilon^{abc}T_c \text{ and } [Y, Y] = 0, \tag{2.5}$$

  where ϵ^{abc} is the antisymmetric tensor.

  For the strong interaction, an octet of gluon fields $G_\mu^{1,\ldots,8}$ that corresponds to the eight generators T^a of the $SU(3)_C$ group is needed. The generators obey the relations

$$\left[T^a, T^b\right] = if^{abc}T_c, \text{ with } Tr\left[T^aT^b\right] = \frac{1}{2}\delta_{ab}, \tag{2.6}$$

  where f^{abc} stands for the structure constants of the $SU(3)_C$ group.

[1] In units of the proton charge $+e$.

The field strength tensors are

$$\begin{aligned} G^a_{\mu\nu} &= \partial_\mu G^a_\nu - \partial_\nu G^a_\mu + g_s f^{abc} G^b_\mu G^c_\nu, \\ W^a_{\mu\nu} &= \partial_\mu W^a_\nu - \partial_\nu W^a_\mu + g_2 \epsilon^{abc} W^b_\mu W^c_\nu, \\ B_{\mu\nu} &= \partial_\mu B_\nu - \partial_\nu B_\mu. \end{aligned} \tag{2.7}$$

with g_s and g_2 being the coupling constants of $\mathrm{SU}(3)_C$ and $\mathrm{SU}(2)_L$, respectively[2]. Due to the non-Abelian nature of the $\mathrm{SU}(3)_C$ and $\mathrm{SU}(2)_L$ groups there are self interactions between their gauge fields ($V_\mu = W_\mu$ or G_μ), namely triple and quartic gauge boson couplings:

$$ig_i \mathrm{Tr}(\partial_\mu V_\nu - \partial_\nu V_\mu)\left[V_\mu, V_\mu\right] \text{(triple)}, \tag{2.8}$$

$$\frac{1}{2} g_i^2 \left[V_\mu, V_\mu\right]^2 \text{(quartic)}. \tag{2.9}$$

The covariant derivative D_μ defined e.g. for quarks as

$$D_\mu \psi = \left(\partial_\mu - i g_s T_a G^a_\mu i g_2 T_a W^a_\mu - i g_1 \frac{Y_q}{2} B_\mu\right)\psi \tag{2.10}$$

couples matter fields ψ to gauge fields, leading to couplings between fermions and gauge fields V_μ of the form:

$$- i g_i \bar{\psi} V_\mu \gamma^\mu \psi. \tag{2.11}$$

Without mass terms, the Lagrangian[3] is given by

$$\begin{aligned} \mathcal{L}_{\mathrm{GSW}} = \; & -\frac{1}{4} G^a_{\mu\nu} G^{\mu\nu}_a - \frac{1}{4} W^a_{\mu\nu} W^{\mu\nu}_a - \frac{1}{4} B_{\mu\nu} B^{\mu\nu} \\ & + i\bar{L}_i D_\mu \gamma^\mu L_i + i\bar{e}_{R_i} D_\mu \gamma^\mu e_{R_i} + i\bar{Q}_i D_\mu \gamma^\mu Q_i + i\bar{u}_{R_i} D_\mu \gamma^\mu u_{R_i} + i\bar{d}_{R_i} D_\mu \gamma^\mu d_{R_i} \end{aligned} \tag{2.12}$$

and it is invariant under local $\mathrm{SU}(3)_C \times \mathrm{SU}(2)_L \times U(1)_Y$ gauge transformations. All gauge and fermion fields have been kept massless. For the strong interaction the gluons are actually known to be massless and mass terms for the colored quarks could be added in an $\mathrm{SU}(3)_C$ gauge invariant way.

However, in the electroweak sector we know that the $W^\pm$ and the Z gauge bosons are massive, but adding mass terms $\frac{1}{2} M_V^2 W_\mu W^\mu$ for the gauge fields would violate $\mathrm{SU}(2)_L \times U(1)_Y$ gauge invariance.

As just inserting the masses explicitly does not work an alternative way of generating them without violating $\mathrm{SU}(2)_L \times U(1)_Y$ gauge invariance is needed.

The easiest and most popular way to do this is the Higgs mechanism for electroweak symmetry breaking [10–14].

[2] The coupling constant of $U(1)_Y$ is called g_1.

[3] Named after Glashow, Salam and Weinberg.

2.1.1 The Higgs Mechanism

Spontaneous Symmetry Breaking and the Goldstone Theorem

For a simple real scalar field ϕ the usual Lagrangian is

$$\mathcal{L} = \frac{1}{2}\partial_\mu\phi\partial^\mu\phi - V(\phi), \tag{2.13}$$

with the potential

$$V(\phi) = \frac{1}{2}\mu^2\phi^2 + \frac{1}{4}\lambda\phi^4 \tag{2.14}$$

and the mass and the self-coupling terms μ^2 and λ, respectively. The Lagrangian is invariant under the reflexion symmetry $\phi \to -\phi$, as there are no cubic terms. The parameter λ needs to be positive for the potential to be bounded from below, as illustrated in Figure 2.1.

If μ^2 is positive the minimum of the potential is at $\langle 0 \mid \phi \mid 0\rangle = \phi_0 = 0$ (left in Figure 2.1) and the Lagrangian $\mathcal{L}$ is simply the one of a spin $s = 0$ particle with mass μ.

For the more interesting case $\mu^2 < 0$ (right in Figure 2.1) the minimum of $V(\phi)$ is at $\langle 0 \mid \phi^2 \mid 0\rangle = \phi_0^2 = -\frac{\mu^2}{\lambda}v^2$, with the quantity $\pm v = \langle 0 \mid \phi \mid 0\rangle$ being called the vacuum expectation value ("vev") of the scalar field ϕ. To interpret $\mathcal{L}$ it needs to be expanded around the minimum v. By defining the field σ as $\phi = v + \sigma$, the Lagrangian becomes:

$$\mathcal{L} = \frac{1}{2}\partial_\mu\sigma\partial^\mu\sigma - (\mu^2)\sigma^2 - \sqrt{-\mu^2\lambda}\sigma^3 - \frac{\lambda}{4}\sigma^4 + const. \tag{2.15}$$

This is the Lagrangian of a scalar field of mass $m^2 = -2\mu^2$, with self interactions proportional to σ^3 and σ^4. As $\mathcal{L}$ now has cubic terms it is no longer invariant under reflexion symmetry; the symmetry is said to be broken, as it is no longer apparent in $\mathcal{L}$. This is the simplest case of spontaneous symmetry breaking and a reflection of the Goldstone theorem [15] that states:

For every spontaneously broken continuous symmetry, the theory contains massless scalar ($s = 0$) particles called Goldstone bosons, with the number of the Goldstone bosons being equal to the number of broken generators.

The Higgs Mechanism in the Standard Model

In the Standard Model masses for the three gauge bosons $W^\pm$ and Z need to be generated, while the photon remains massless. Hence at least three degrees of freedom are needed for the scalar fields. The simplest choice is a complex SU(2) doublet of scalar fields ϕ

$$\Phi = \begin{pmatrix} \phi^+ \\ \phi^0 \end{pmatrix}, \text{ with } Y_\phi = +1. \tag{2.16}$$

The invariant terms of the scalar field

$$\mathcal{L}_S = (D^\mu\Phi)^\dagger\left(D_\mu\Phi\right) - \mu^2\Phi^\dagger\Phi - \lambda(\Phi^\dagger\Phi)^2 \tag{2.17}$$

are added to the electroweak Lagrangian $\mathcal{L}_{\text{GSW}}$ [4]. The neutral component of the doublet field Φ obtains a non-vanishing vacuum expectation value for $\mu^2 < 0$:

$$\langle\Phi\rangle_0 = \langle 0 \mid \Phi \mid 0\rangle = \begin{pmatrix} 0 \\ \frac{v}{\sqrt{2}} \end{pmatrix}, \text{ with } v = \sqrt{-\frac{\mu^2}{\lambda}}. \tag{2.18}$$

A similar exercise as the one presented in the previous paragraph leads to spontaneous breaking of the $SU(2)_L \times U(1)_Y$ symmetry and the W and Z bosons acquire masses by absorbing the Goldstone bosons, while the photon stays massless:

$$M_W = \frac{1}{2} v g_2 \,, \quad M_Z = \frac{1}{2} v \sqrt{g_2^2 + g_1^2} \,, \quad M_\gamma = 0. \tag{2.19}$$

For the fermions, masses can be generated using the same scalar field Φ and the hypercharge $Y = -1$ isospin doublet $\tilde{\Phi} = i\sigma_2 \Phi^*$ by introducing the $SU(2)_L \times U(1)_Y$ invariant Yukawa Lagrangian

$$\mathcal{L}_{\text{F}} = -\lambda_e \bar{L} \Phi e_R - \lambda_d \bar{Q} \Phi d_R - \lambda_u \bar{Q} \Phi u_R + h.c. \tag{2.20}$$

The masses can be evaluated to be

$$m_e = \frac{1}{2} \frac{\lambda_e v}{\sqrt{2}}, \quad m_u = \frac{1}{2} \frac{\lambda_u v}{\sqrt{2}}, \quad m_d = \frac{1}{2} \frac{\lambda_d v}{\sqrt{2}}. \tag{2.21}$$

Therefore with the same isospin doublet of scalar fields Φ the masses of both the weak vector bosons and the fermions can be generated, while the $SU(2)_L \times U(1)_Y$ symmetry is broken into $SU(2)_{\text{weak}}$ and $U(1)_\gamma$. The color symmetry $SU(3)_C$ stays unbroken.

[4] Ignoring the strong interaction part.

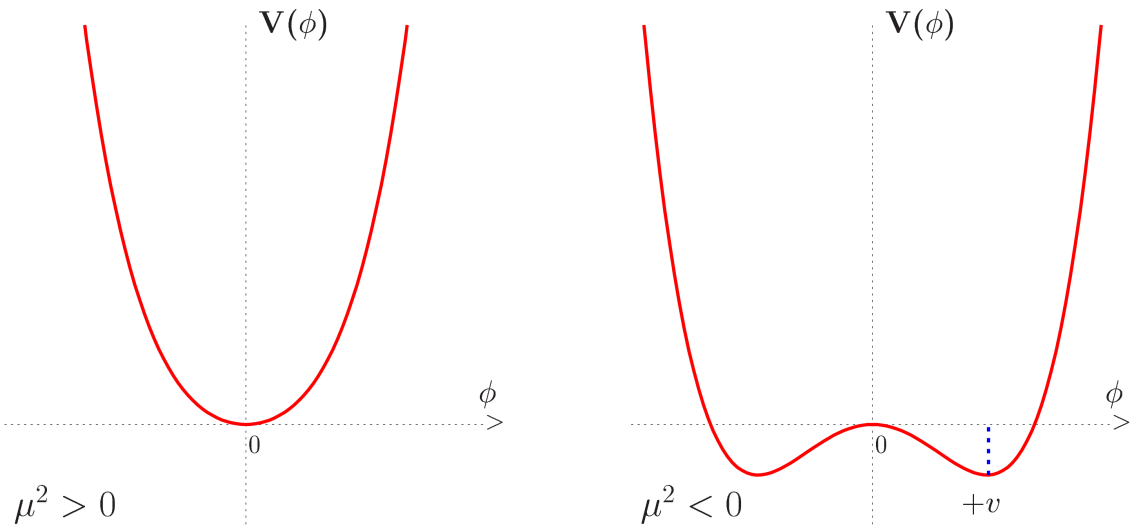

Figure 2.1: The potential V of the scalar field ϕ for the mass term $\mu^2 > 0$ (left) and $\mu^2 < 0$ (right) [8].

The Lagrangian containing the Higgs field H is given by

$$\mathcal{L}_H = \frac{1}{2}(\partial^\mu H)^2 - \lambda v^2 H^2 - \lambda v H^3 - \frac{\lambda}{4} H^4. \tag{2.22}$$

The Higgs boson mass is given by

$$M_H^2 = 2\lambda v = -2\mu^2, \tag{2.23}$$

the Feynman rules for the Higgs self interactions are

$$g_{H^3} = 3i\frac{M_H^2}{v}, \quad g_{H^4} = 3i\frac{M_H^2}{v^2}, \tag{2.24}$$

the couplings to gauge bosons and fermions are

$$g_{Hff} = i\frac{m_f}{v}, \quad g_{HVV} = -2i\frac{M_V}{v}, \quad g_{HHVV} = -2i\frac{M_V}{v^2}. \tag{2.25}$$

The vacuum expectation value v is fixed and can be expressed in dependence of the mass of the W gauge boson or the Fermi constant G_F

$$M_W = \frac{1}{2} g_2 v = \left(\frac{\sqrt{2} g_2^2}{8 G_F}\right)^{\frac{1}{2}} \quad \rightarrow \quad v = \frac{1}{(\sqrt{2} G_F)^{\frac{1}{2}}} \approx 246 \text{ GeV}. \tag{2.26}$$

Higgs Boson Production

At hadron colliders the main production processes of the Higgs boson are the ones where the Higgs boson couples to particles with large masses, i.e. the Z and W bosons, the top quark and to a lesser extent the bottom quark.

These are:

- associated production with W/Z bosons $q\bar{q} \rightarrow V + H$,
- vector boson fusion $qq \rightarrow V^* V^* \rightarrow qq + H$,
- gluon-gluon fusion $gg \rightarrow H$,
- and associated production with heavy quarks $gg \rightarrow Q\bar{Q} + H$,

where Q denotes a heavy quarks. Diagrams of these processes are shown in Figure 2.2 and their cross sections in dependence of the Higgs boson mass M_H for the LHC running at its design center-of-mass energy of 14 TeV are shown in Figure 2.3.

Decays of the Higgs Boson

Since the Higgs couplings to both gauge bosons and fermions are directly proportional to the masses of the particles it will predominantly decay into the heaviest particles kinematically allowed. It can decay into pairs of quarks or leptons or into real and or virtual gauge bosons. A decay into two photons is possible via a fermion loop.

In Figure 2.4 the branching ratios of the Higgs bosons as a function of its mass M_H is shown.

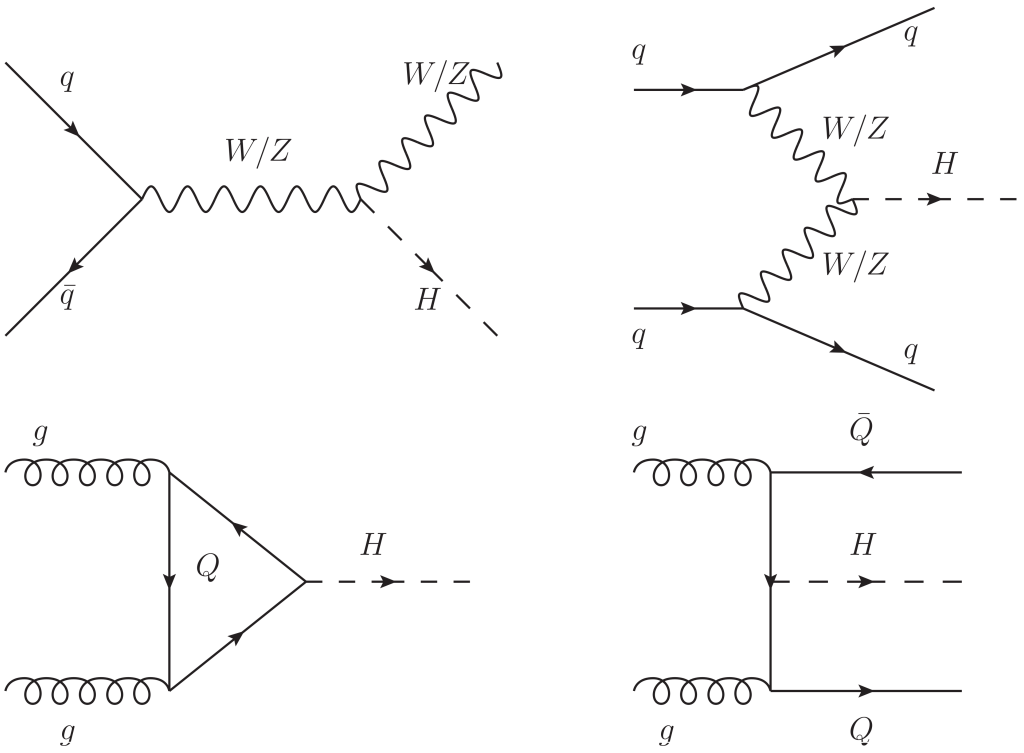

Figure 2.2: Dominant Standard Model Higgs boson production processes in hadronic collisions, from top left to bottom right: associated production with W/Z bosons, vector boson fusion, gluon-gluon fusion and associated production with heavy quarks.

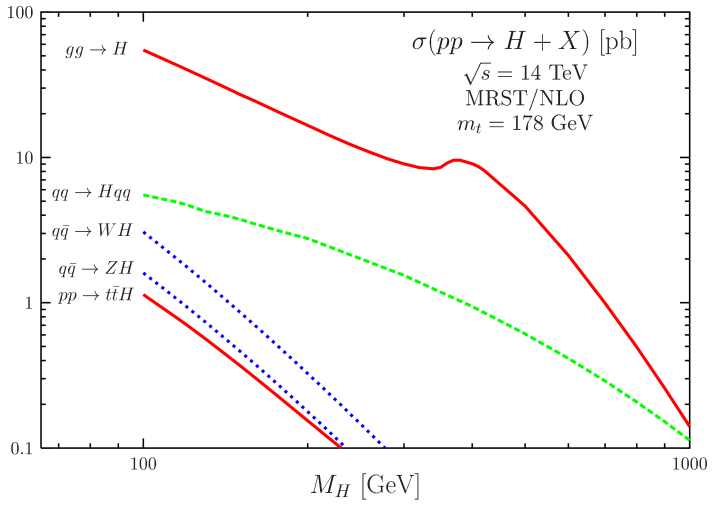

Figure 2.3: Standard Model Higgs boson production cross sections for the dominant production processes in dependence of the Higgs boson mass M_H for the LHC running at its design center-of-mass energy of 14 TeV. The MSTW parton distribution function ("PDF", see also 2.3.) set has been used [8].

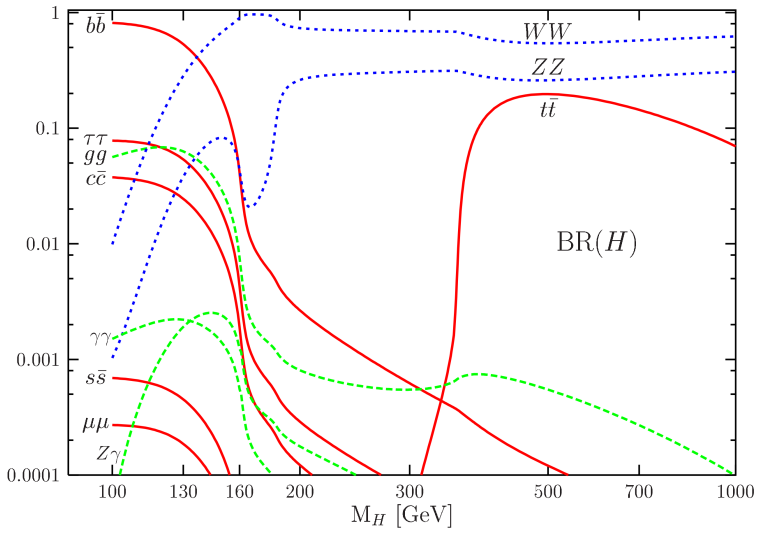

Figure 2.4: The Standard Model Higgs boson decay branching ratios as a function of the Higgs boson mass M_H [8].

Constraints on the Higgs Boson Mass

There are both experimental and theoretical constraints on the Higgs boson mass. The constraints from experiments are from direct searches at the e^+e^--collider LEP [16], the hadron collider Tevatron and lately the LHC and from precise measurements of electroweak observables. All parameters measured in the electroweak sector are influenced by the Higgs boson mass through radiative corrections.

A combined fit of this precision data yields a most likely value of

$$M_H = 114^{+69}_{-45}\ \text{GeV} \tag{2.27}$$

for the Standard Model Higgs boson mass M_H [17].

Recent results of direct searches performed by ATLAS [4] and CMS [5] at the LHC indicate the discovery of a boson with a mass of 125 GeV that seems to be compatible with a Standard Model Higgs boson so far. Further experimental test using the large dataset that will be collected until the end of 2012 at a higher center-of-mass energy will help to better understand the new particle.

In theory, problems arise for example in high energy longitudinal $W^+W^- \rightarrow W^+W^-$ scattering where the cross section rises proportional to the scattering energy and thus violates unitarity unless the effect is canceled by processes involving a scalar particle such as the Higgs boson. From this unitarity argument an upper limit in the range of 1 TeV can be set on M_H. Keeping the vacuum stable and disallowing a non-interacting theory leads to the so-called stability and triviality bounds that restrict the Higgs boson mass M_H in dependence of a new physics cut-off scale Λ. This dependence is shown in Figure 2.5.

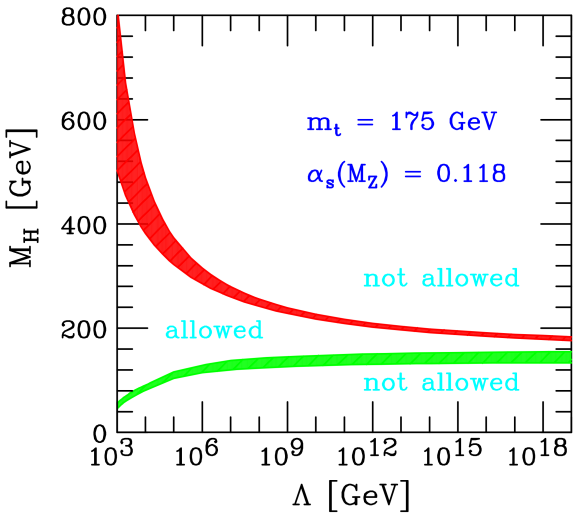

Figure 2.5: Distribution of the triviality and vacuum stability bounds on the Standard Model Higgs boson mass M_H in dependence of the new physics cut-off scale Λ. The allowed region lies within the colored bands, the width of the bands implies the impact of various uncertainties. A top quark mass of $M_t = 175 \pm 6$ and the strong coupling constant at the Z boson mass scale $\alpha_S(M_Z) = 0.118 \pm 0.002$ have been assumed [18].

2.2 Supersymmetry

Although the Standard Model has been extremely successful at describing all experimental data so far it is widely believed to be an effective theory only valid at the energies presently accessible. It cannot be the final answer, as it does not include the fourth force – gravity – and does not explain the mass pattern of the fermions.

In addition, it has at least three major problems:

- The mathematical representation of the Standard Model is the direct product of three gauge groups, but with different coupling constants and does not provide a unification of the electroweak and the strong interactions. This unification is expected to happen at a much larger energy scale, where a single gauge group may describe the three forces in a more fundamental Grand Unified Theory ("GUT", scale: $\Lambda_{\mathrm{GUT}} \approx 10^{16}$ GeV). Based on the measurements performed so far, the extrapolation of the measured coupling constants to higher energies using renormalization group equations show that the couplings do not meet at a common point. This is referred to as the **unification problem**.

- For some time it has been known from cosmological observations that a large part of the energy content of our universe is due to **dark matter**. A particle that could explain the existence of this non-luminous, non-baryonic and most probably non-relativistic ("cold") matter has not been discovered and therefore it has to be electrically neutral and weakly interacting. In particular the Standard Model does not provide a particle that is a candidate for dark matter.

- The radiative corrections to the square of the Higgs boson mass M_H^2 are quadratically divergent in the cut-off scale Λ; at this energy the theory becomes invalid and new physics must appear. The cut-off scale can be chosen to be at the GUT scale but then the Higgs boson mass would preferably be close to the GUT scale. However, due to experimental and theoretical constraints the Higgs

boson mass should be of the order of the electroweak symmetry breaking scale $v \approx 250$ GeV. In the Standard Model this problem can only be solved by an unnatural fine tuning of the parameters involved (order of 10^{16}). This is called the **fine-tuning** or **naturalness problem**. It is related to the hierarchy problem, which refers to the fact that there is no explanation in the Standard Model why the GUT scale is so much larger than the electroweak scale, $\Lambda \gg v$.

Supersymmetry is one, if not the most, popular extension to the Standard Model, that can address the above mentioned problems.

Supersymmetry Fundamentals

Supersymmetry is a symmetry that relates bosons, particles of integer spin ($s = 0, 1, ...$) and fermions, particles of half-integer spin ($s = \frac{1}{2}, \frac{3}{2}, ...$):

$$Q \mid \text{Fermion}\rangle = \mid \text{Boson}\rangle, \quad Q \mid \text{Boson}\rangle = \mid \text{Fermion}\rangle \tag{2.28}$$

with Q being the Supersymmetry generator. Due to the symmetry the particles and their superpartners[5] have the same masses and quantum numbers, except for the spin. This is clearly not the case, as e.g. no particle of spin $s = 0$ with the electron mass and the same properties as the electron (other than the spin) exists, hence Supersymmetry needs to be a broken symmetry. The Supersymmetry breaking needs to occur in such a way that the Supersymmetry particles are not too heavy in order not to reintroduce the hierarchy problem. It needs to conserve gauge invariance and the theory must remain renormalizable.

Supersymmetry can solve the aforementioned problems:

- The added new Supersymmetry particles contribute to the renormalization group evolution of the coupling constants and alter their slopes so that they meet close to the GUT scale.
- As lepton and baryon number violating terms are allowed in the Supersymmetry Lagrangian the discrete and multiplicative R-parity defined as

$$R_P = (-1)^{2s+3B+L} \tag{2.29}$$

  where L and B are the lepton and baryon numbers and s is the spin quantum number, is imposed to enforce lepton and baryon number conservation. Standard Model particles carry $R_P = +1$ while their supersymmetric partners carry $R_P = -1$, hence R-parity conservation implies that Supersymmetry particles can only be produced in pairs and that the lightest one needs to be stable. In many Supersymmetry models this particle is a massive, electrically neutral and weakly interacting particle and hence a good dark matter candidate.
- The new symmetry also prevents the Higgs bosons mass from acquiring large radiative corrections, as the quadratic divergences due to loop contributions of the Standard Model model particles are canceled by the corresponding loop contributions from their supersymmetric partners if their masses are the same. Therefore no unnatural fine-tuning is required.

In the following the Minimal Supersymmetric Standard Model ("MSSM") is discussed and its Higgs boson sector is explored.

[5] The superpartners to the Standard Model fermions are referred to as sfermions, e.g. the partner of the electron is the selectron, which is a slepton, in short it can be written as $\tilde{e}$ and superfields are also marked with a tilde. The superpartners of the Standard Model bosons are getting the suffix "ino". e.g. the partner of the W is called wino, and also marked with a tilde. Note that each chiral Standard Model field obtains a superpartner field, e.g. there are superpartners for each e_R^- and e_L^-.

2.2.1 The Minimal Supersymmetric Standard Model

The MSSM is the most basic supersymmetric extension of the Standard Model, defined by four assumptions:

- Minimal gauge group: The MSSM is based on the Standard Model gauge symmetry, i.e. the $SU(3)_C \times SU(2)_L \times U(1)_Y$ group. Therefore before electroweak symmetry breaking, the spin $s = 1$ gauge boson fields have $s = \frac{1}{2}$ superpartners the gaugino fields (the bino $\tilde{B}$, the three wino $\tilde{W}_{1,2,3}$ and the eight gluino $\tilde{G}_{1-8}$ fields).

- Minimal particle content: As in the Standard Model there are only three generations of spin $s = \frac{1}{2}$ quarks and leptons in the MSSM. Together with their spin $s = 0$ superpartners, the squarks and sleptons, they form chiral superfields $\hat{Q}$, $\hat{U}_R$, $\hat{D}_R$, $\hat{L}$ and $\hat{E}_R$, where e.g. $\hat{Q}$ contains the quark fields (u_L, d_L) and their squark superpartner fields denoted $(\tilde{u}_L, \tilde{d}_L)$. In addition two chiral superfields $\hat{H}_1$, $\hat{H}_2$ of opposite hypercharges -1 and $+1$ are needed. Their scalar components H_1, H_2 give masses to the down and up-type fermions, respectively. This leads to five Higgs particles, discussed below, the two CP-even h and H bosons, a CP-odd A boson and two charged $H^\pm$ bosons. The Higgs field's superpartner fields, the higgsino fields, mix with the wino and bino fields to form mass eigenstates, two charginos $\chi^\pm_{1,2}$ and four neutralinos $\chi^0_{1,2,3,4}$.

- R-parity conservation (see Equation 2.29).

- Minimal Supersymmetry breaking: As mentioned before Supersymmetry is a broken symmetry. It is assumed that some fields at higher mass (in the "hidden sector") scales spontaneously break the symmetry and that this broken symmetry is then observed at the lower mass scale (i.e. the "visible sector") of the MSSM particles. Supersymmetry breaking scenarios are based on how the breaking is mediated from the hidden to the visible sector, e.g. gravity mediated ("mSugra") [19–21] or gauge mediated ("GMSB") [22–27]. Instead of using an explicit breaking scenario in the MSSM only soft breaking terms [28] are added to the Lagrangian. These are mass terms for the gauginos and the scalar fermions, mass and bilinear terms for the Higgs bosons and trilinear couplings between sfermions and Higgs bosons.

These conditions define the so-called unconstrained MSSM that introduces 105 additional unknown parameters to the theory. Using phenomenological assumptions, e.g. about unification at the GUT scale, this can be simplified to the constrained MSSM that needs 22 parameters in addition to the Standard Model parameters. Those are the masses of the bino, wino, the gluinos and the sfermions, the ratio of the vacuum expectation values of the two Higgs doublet fields, $\tan\beta$, the CP-odd Higgs boson's mass M_A[6] and the Higgs-higgsino mass parameter μ [28].

For a given set of these parameters the according MSSM mass spectrum for the sparticles can be predicted. Searches for squarks and sleptons are an important part of the physics program at the LHC. In the following the focus will be on the MSSM Higgs sector.

[6] Within this chapter the masses of the Higgs bosons will be denoted with M, as e.g. M_A, for internal consistency, which is interchangeable with m, e.g. m_A, used in the other chapters.

2.2.2 The MSSM Higgs Sector

Masses of the MSSM Higgs Bosons

In the MSSM two doublets[7] of complex scalar fields of opposite hypercharge

$$H_1 = \begin{pmatrix} H_1^0 \\ H_1^- \end{pmatrix} \text{ with } Y_{H_1} = -1, \quad H_2 = \begin{pmatrix} H_2^+ \\ H_2^0 \end{pmatrix} \text{ with } Y_{H_2} = +1 \tag{2.30}$$

are needed to break the electroweak symmetry. The neutral components of the Higgs fields acquire vacuum expectation values:

$$\langle H_1^0 \rangle = \frac{v_1}{\sqrt{2}}, \quad \langle H_2^0 \rangle = \frac{v_2}{\sqrt{2}}. \tag{2.31}$$

They are related to the Standard Model vacuum expectation value v:

$$v_1^2 + v_2^2 = v^2 = \frac{4M_Z}{g_1^2 + g_2^2} = (246 \text{ GeV})^2, \tag{2.32}$$

and appear in the definition of the important parameter

$$\tan\beta = \frac{v_2}{v_1} = \frac{v \sin\beta}{v \cos\beta}. \tag{2.33}$$

The quantity β can also be interpreted as a rotation angle in the mixing of the fields to the physical CP-odd and charged Higgs bosons and the Goldstone bosons G^0, $G^\pm$

$$\begin{pmatrix} G^0 \\ A \end{pmatrix} = \begin{pmatrix} \cos\beta & \sin\beta \\ -\sin\beta & \cos\beta \end{pmatrix} \begin{pmatrix} \text{Im}\left(H_1^0\right) \\ \text{Im}\left(H_2^0\right) \end{pmatrix}, \tag{2.34}$$

$$\begin{pmatrix} G^\pm \\ H^\pm \end{pmatrix} = \begin{pmatrix} \cos\beta & \sin\beta \\ -\sin\beta & \cos\beta \end{pmatrix} \begin{pmatrix} \text{Re}\left(H_1^\pm\right) \\ \text{Re}\left(H_2^\pm\right) \end{pmatrix}. \tag{2.35}$$

The physical CP-even Higgs bosons are a mixture of the real parts of the fields H_1^0 and H_2^0

$$\begin{pmatrix} H \\ h \end{pmatrix} = \begin{pmatrix} \cos\alpha & \sin\alpha \\ -\sin\alpha & \cos\alpha \end{pmatrix} \begin{pmatrix} \text{Re}\left(H_1^0\right) \\ \text{Re}\left(H_2^0\right) \end{pmatrix}, \tag{2.36}$$

with the mixing angle α given by

$$\alpha = \frac{1}{2} \arctan\left(\tan 2\beta \frac{M_A^2 + M_Z^2}{M_A^2 - M_Z^2} \right). \tag{2.37}$$

[7] Two Higgs-doublet models ("2HDM") are classified in three types, Type-I, where one doublet couples to up and down type quarks simultaneously, Type-II where one doublet couples only to up and the other only to down type particles and Type-III where both doublets couple to up and down type quarks simultaneously. The MSSM Higgs sector is a 2HDM Type-II.

	up-type	down-type	W/Z	AZ	$H^{\pm}W^{\mp}$
Standard Model	1	1	1	0	0
h	$\cos\alpha/\sin\beta$	$-\sin\alpha/\cos\beta$	$\sin(\beta-\alpha)$	$\cos(\beta-\alpha)$	$\mp\cos(\beta-\alpha)$
H	$\sin\alpha/\sin\beta$	$\cos\alpha/\cos\beta$	$\cos(\beta-\alpha)$	$-\sin(\beta-\alpha)$	$\pm\sin(\beta-\alpha)$
A	$\cot\beta$	$\tan\beta$	0	0	1

Table 2.2: Couplings of the MSSM Higgs bosons to fermions and gauge bosons normalized to the Standard Model couplings.

On tree-level the masses of the charged Higgs bosons and the CP-even neutral Higgs bosons can be expressed in dependence of the parameter $\tan\beta$ and the mass of the CP-odd Higgs boson M_A:

$$M_{H^{\pm}}^2 = M_A^2 + M_W^2, \tag{2.38}$$

$$M_{h,H}^2 = \frac{1}{2}\left(M_A^2 + M_Z^2 \mp \sqrt{\left(M_A^2 + M_Z^2\right)^2 - 4M_A^2 M_Z^2 \cos^2 2\beta}\right). \tag{2.39}$$

The theory thus imposes strong constraints on the MSSM Higgs boson masses, most notably

$$M_h \leq \min(M_A, M_Z) \cdot |\cos 2\beta| \leq M_Z. \tag{2.40}$$

A mass smaller than the mass of the Z boson, M_Z, is predicted for the lighter CP-even Higgs boson h at tree-level. However, radiative corrections turn out to be significant and push the mass M_h high enough for it not to be already excluded by experiments. To get an upper bound on M_h the corrections can be evaluated in the limits of $M_A \gg M_Z$ and $\tan\beta \gg 1$ and under the assumption that the two stops[8] have the same mass around the Supersymmetry scale M_S and do not mix with each other ($X_t = A_t - \mu\cot\beta \ll M_S$, where A_t is the trilinear coupling of the Higgs bosons to the stops.).

The corrections can be written as

$$\Delta M_h^2 = \frac{3G_\mu}{\sqrt{2}\pi^2} m_t^4 \log\frac{M_S^2}{m_t^2} \tag{2.41}$$

and shift the mass M_h up to ≈ 140 GeV.

The maximal light Higgs boson mass M_h is realized in the maximal mixing or $M_h^{\max}$ scenario [29], where the stops are heavy and the mixing in the stop sector is maximal ($X_t = \sqrt{6}M_S$). In Figure 2.6 the dependence of $M_{H^{\pm}}$, M_h and M_H on M_A for two values of $\tan\beta$ is shown. For masses M_A above ≈ 150 GeV the mass of the lightest Higgs boson M_H saturates to a maximum value of $M_H \approx 140$ GeV, while the masses of A, H and $H^{\pm}$ become degenerate and are only weakly dependent on $\tan\beta$.

Couplings of the MSSM Higgs Bosons

The couplings of the MSSM Higgs bosons to fermions and gauge bosons depend on $\tan\beta$ and on the mixing angle α for the CP-even Higgs bosons. Normalized to the Standard Model couplings they are listed in Table 2.2. For large values of $\tan\beta$ the coupling of the CP-odd Higgs boson A to down-type particles is enhanced and therefore bottom quarks and τ leptons as the heaviest down-type fermions are coupled to preferentially.

[8] The left- and right handed field components of the stop mix into two different mass eigenstates.

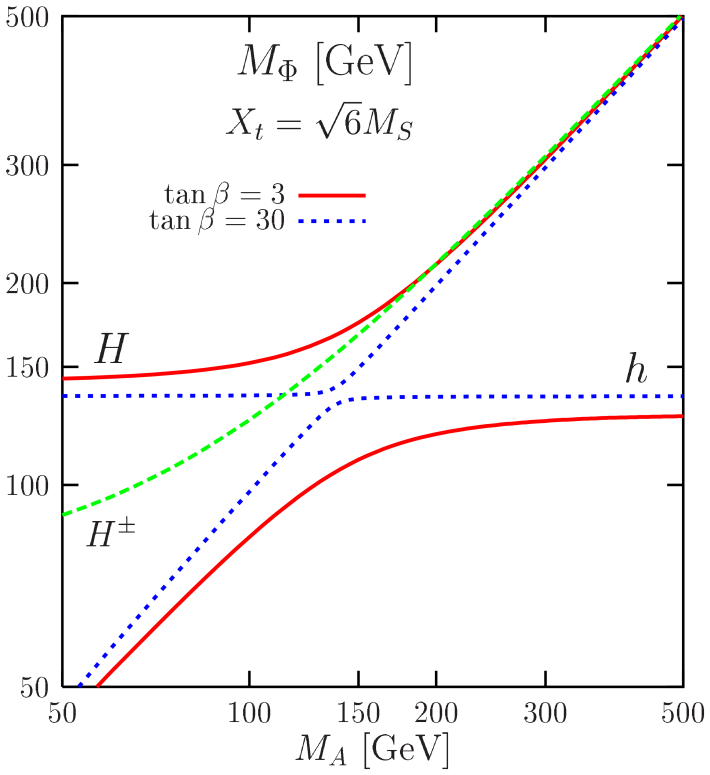

Figure 2.6: Higgs boson masses $M_{H^\pm}$, M_h and M_H in dependence of M_A for $\tan\beta = 3$ (solid line) and $\tan\beta = 30$ (dashed line). [9].

Production of the Neutral MSSM Higgs Bosons

The dominant production processes of the neutral MSSM Higgs bosons at the LHC, which are the main topic of this thesis, are similar to those in the Standard Model (Section 2.1.1), but with the important difference that for large $\tan\beta$ the main contribution to the gluon fusion and the associated production processes is from b instead of top quarks. The Feynman graphs for the production processes are shown in Figure 2.7.

The production cross section in dependence of the masses of the Higgs bosons for $\tan\beta = 3$ and $\tan\beta = 30$ is shown in Figure 2.8. The enhanced coupling for large $\tan\beta$ is reflected in the cross sections being larger by about one order of magnitude. More general, for large $\tan\beta$ the production cross section can approximately be described by $\sigma_A \approx \tan\beta^2$. Thus the parameter space with larger $\tan\beta$ is easier to explore as more potential Higgs bosons are produced.

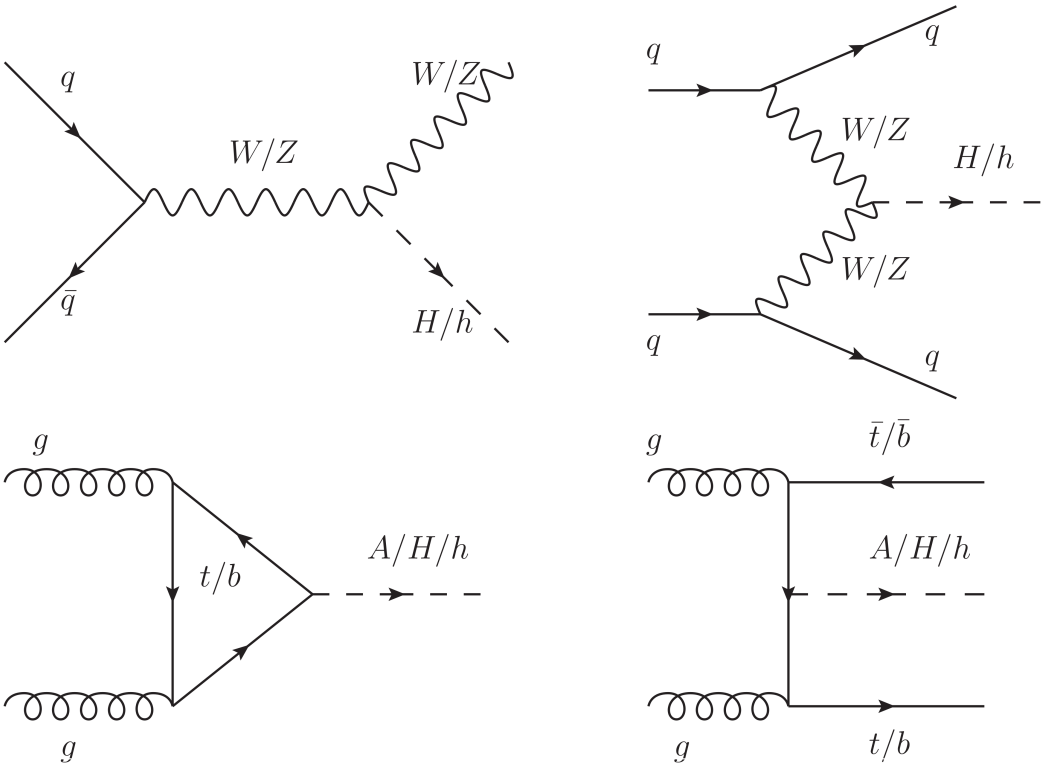

Figure 2.7: Dominant MSSM Higgs boson production processes in hadronic collisions, from top left to bottom right: associated production with W/Z bosons, vector boson fusion, gluon-gluon fusion and associated production with heavy quarks.

Decays of the Neutral MSSM Higgs Bosons

The most important decay modes of the neutral MSSM Higgs bosons are those that are also important in the Standard Model. In addition, depending on the masses of the Higgs bosons and those of the other Supersymmetry particles new decay channels into Supersymmetry particles can open up. In the context of this thesis the most interesting case is for large $\tan\beta$ where the decays into pairs of b quarks and τ leptons become dominant. In Figure 2.9 (2.10) the branching ratios of the CP-even (CP-odd)

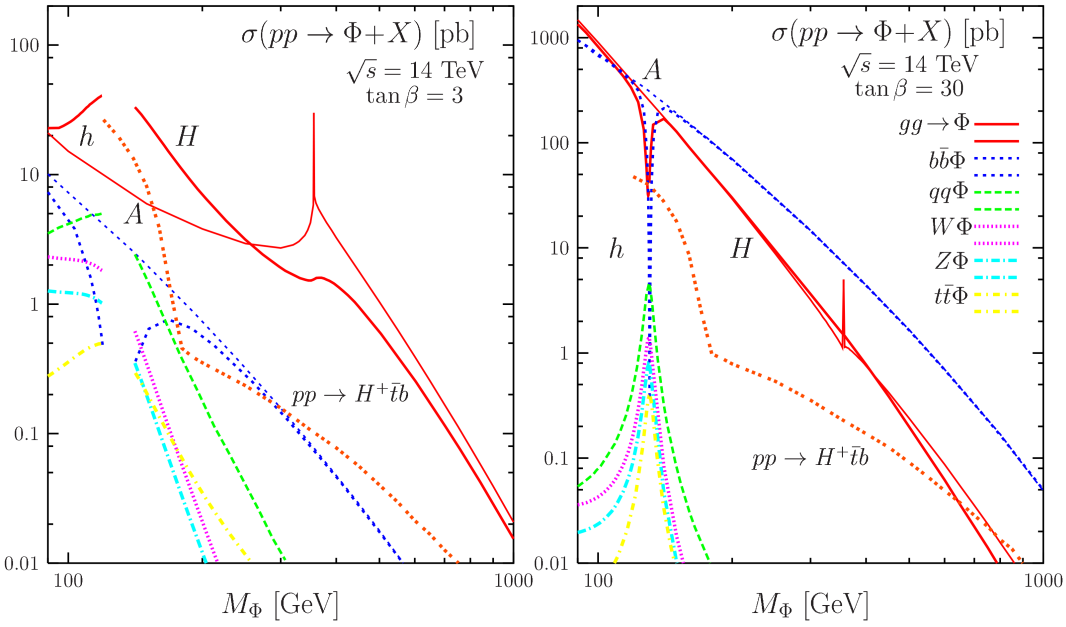

Figure 2.8: MSSM Higgs boson production cross section in hadronic collisions in dependence of the Higgs boson mass M_Φ, where Φ is a placeholder for the different MSSM Higgs bosons, for $\tan\beta = 3$ (left) and $\tan\beta = 30$ (right) [9].

Higgs bosons in dependence of their masses for $\tan\beta = 3$ and $\tan\beta = 30$ is presented. While for the lower value of $\tan\beta$ the behavior is not too different compared with the Standard Model case, for high $\tan\beta$, the Higgs bosons almost exclusively decay into b quarks ($\approx 90\%$) and τ leptons ($\approx 10\%$). Due to the much lower background rates expected from final states with τ leptons compared to the vast QCD multi-jet background for final states with multiple b jets, the di-τ channel is the most promising channel and the search presented here is performed in it.

Constraints on the MSSM Higgs Boson Masses

Out of the two parameters M_A and $\tan\beta$ that govern the MSSM Higgs sector, the second can be constrained, e.g. in models with universal boundary conditions at the GUT scale [30]:

$$1 \leq \tan\beta \leq m_t/m_b, \tag{2.42}$$

which at the Supersymmetry scale $M_S \approx 1$ TeV translates to about $1 \leq \tan\beta \leq 60$.

As mentioned earlier the upper bound on light Higgs boson mass is of the order of

$$M_h^{\max} \approx 140 \text{ GeV}. \tag{2.43}$$

The masses of the heavy Higgs bosons M_H and M_A can in principle not be constrained and therefore can become very large, as unlike in the Standard Model case the CP-even Higgs boson will decouple from the gauge bosons W/Z and the CP-odd Higgs boson does not couple to them at all and therefore unitarity arguments do not apply. However, since the particles are the remnants of electroweak symmetry breaking their masses are not expected to be too far from the breaking scale, i.e. $M_{H,A} \lessapprox 1$ TeV.

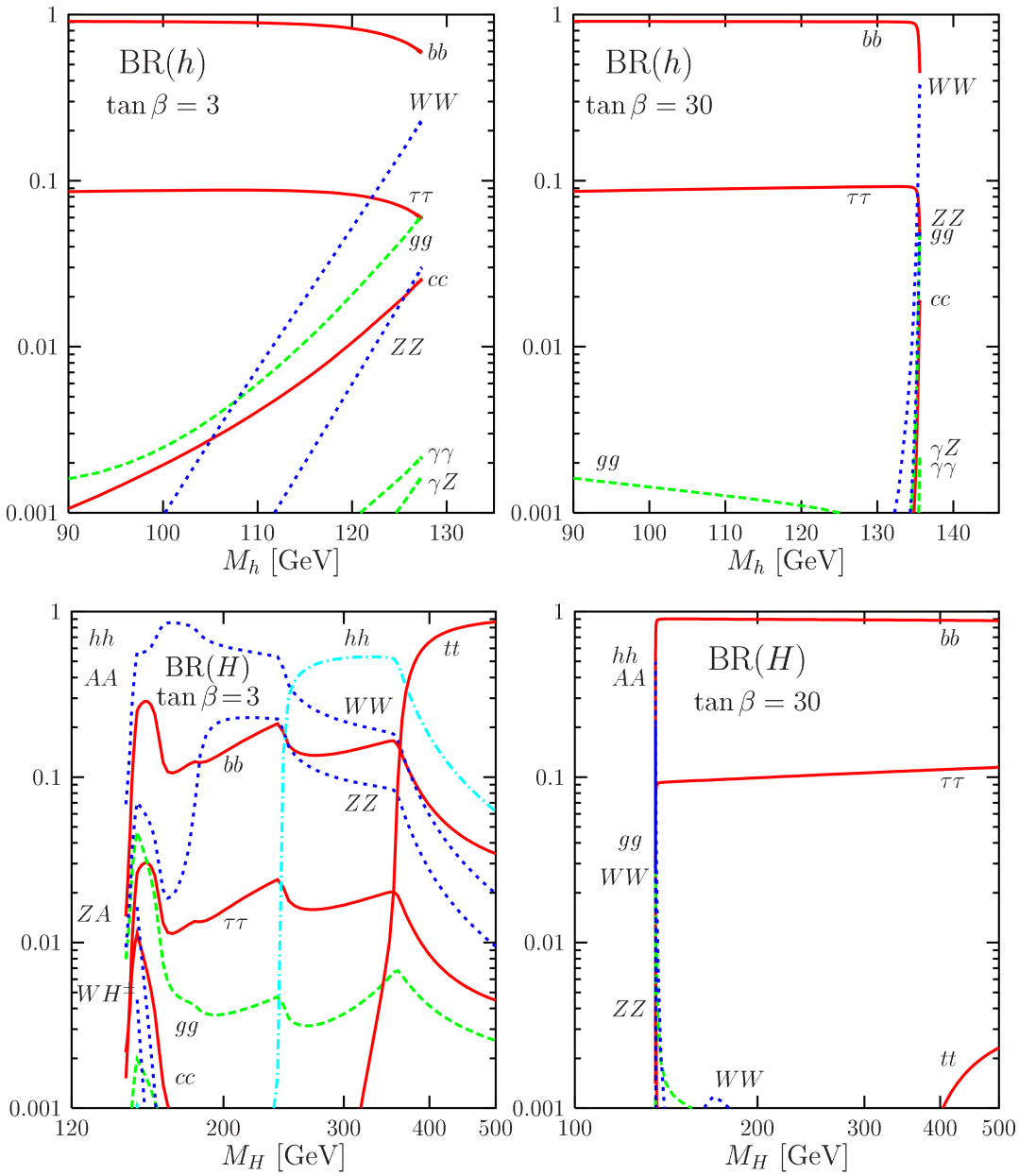

Figure 2.9: Branching ratios of the light (top) and heavy (bottom) CP-even MSSM Higgs bosons in dependence of their masses for $\tan\beta = 3$ (left) and $\tan\beta = 30$ (right). The maximal mixing scenario is used. [9].

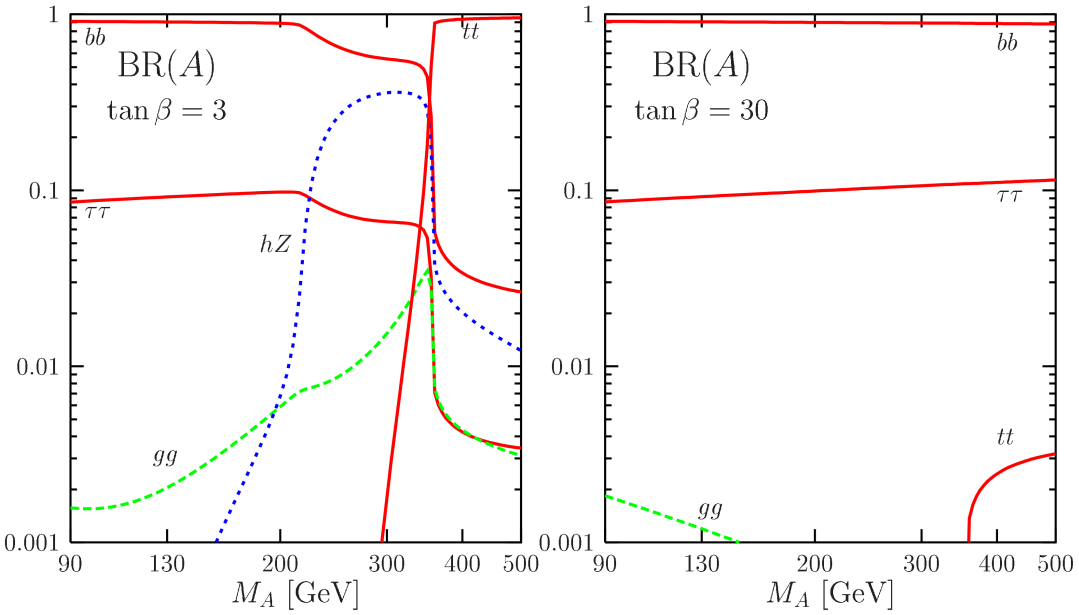

Figure 2.10: Branching ratio of the CP-odd MSSM Higgs boson in dependence of its mass for $\tan\beta = 3$ (left) and $\tan\beta = 30$ (right). The maximal mixing scenario is used [9].

The LEP collaborations have set 95% confidence limits on M_h and M_A [31]

$$M_h > 91.0 \text{ GeV}, \quad \text{and} \quad M_A > 91.9 \text{ GeV}, \tag{2.44}$$

in the $e^+e^- \to hA/HA$ channel in the scenario where the coupling of the Z boson to hA pairs is maximal and for large $\tan\beta$.

Searches for the neutral MSSM Higgs bosons are actively conducted at the LHC and the resulting exclusion limits will be discussed later in this thesis (see Chapter 8).

2.2.3 Decay Channels and Signal Signature of $A/H/h \to \tau^+\tau^-$

In the following a search for neutral MSSM Higgs bosons in final states with τ pairs will be presented. The τ lepton, as the heaviest known lepton, decays not only to electrons or muons but due to is mass also to hadrons. The leptonic branching fractions are $(17.85 \pm 0.05)\%$ for $\tau^- \to e^-\bar{\nu}_e\nu_\tau$[9] and $(17.36 \pm 0.05)\%$ for $\tau^- \to \mu^-\bar{\nu}_\mu\nu_\tau$ [32].

Thus almost 65% of the decays are into hadrons: $\tau^- \to \text{hadrons} + \nu_\tau$.

Hence, when reconstructing di-τ final states one has the choice of three classes of final states:

- the fully leptonic channel, where both τ leptons decay into electrons or muons, i.e. $\tau^+\tau^- \to e^+e^- + 4\nu$ (3%), $\tau^+\tau^- \to \mu^+\mu^- + 4\nu$ (3%) and $\tau^+\tau^- \to e^+\mu^- + 4\nu$ (6%),
- the fully hadronic channel, where both τ leptons decay into hadrons, i.e. $\tau^+\tau^- \to \text{hadrons} + 2\nu$ (42%) and
- the "lepton-hadron" channel, where one τ leptons decays into leptons and the other into hadrons, i.e. $\tau^+\tau^- \to e\,\text{hadrons} + 3\nu$ (23%) and $\tau^+\tau^- \to \mu\,\text{hadrons} + 3\nu$ (23%)

[9] The charge conjugate modes are included implicitly, if not mentioned otherwise.

All three categories have experimental advantages and disadvantages. The two light leptons in the fully leptonic channel are a clean signature at hadron colliders, especially in the final state with an electron and a muon as most potential backgrounds are more likely to produce pairs of electrons or muons and not a mixture. In addition, requiring two light leptons in the final state allows for the use of low kinematic thresholds for the leptons, hence the channel is sensitive to low Higgs boson masses, where the τ leptons and their decay products are of rather low momentum. The fully hadronic channel has the advantage of the large branching fraction and as only two neutrinos are produced in this final state it potentially allows for the most precise reconstruction of the mass of the di-τ system and thus the Higgs boson mass. The main disadvantage is that τ leptons reconstructed in the hadronic final state are hard to differentiate from jets produced in QCD interactions, and therefore stringent kinematic selection criteria and high trigger thresholds must be applied, hence this channel is most sensitive for large Higgs boson masses.

Finally the lepton-hadron channel, that will be used for the search presented here, offers a large branching fraction and one light lepton whose signature is useful to discriminate a potential signal from the vast background from QCD processes. Hence the most sensitive kinematic region explorable by this channel is in between the other two channels and this channel offers the best sensitivity over a much larger range of potential Higgs boson masses then the two other channels.

In conclusion the experimental signatures considered in this analysis are:

- Exactly one light lepton, i.e. an electron or a muon; the channels will be referred to as $e\tau_{\text{had}}$ and $\mu\tau_{\text{had}}$ accordingly.
- Exactly one hadronic τ decay, in the following referred to as τ_{had} decay, or τ_{had} candidate for the actual reconstructed object.
- Missing energy and momentum, due to the three neutrinos that are not detectable within a collider experiment.

In Chapter 5.3 a signal selection exploiting this signal topology will be presented.

2.3 Physics at Hadron Colliders

Measuring physics processes at hadron colliders, e.g. in proton-proton collisions at the LHC, is very challenging for several reasons. Unlike in electron-positron collision experiments where the center-of-mass energy $\sqrt{s}$ of the interacting particles is known very precisely, it is a priori unknown which partons in the protons interact and what part of the total proton momentum they carry. A consequence of the uncertainty on the initial state is that an estimation of the initial energy is not possible in the direction of the colliding beams.

In the following, the calculation of hadron collider processes in the framework of perturbative QCD and the experimental challenges to measure them are briefly introduced. An overview can be found in [33].

2.3.1 Cross Sections for Hadronic Interactions

The Standard Model does not describe the interactions of hadrons but those of elementary particles such as quarks and gluons, which are referred to as partons (as they are the parts that make up hadrons). For the production of heavy particles the so-called “hard interaction”, which involves a high energy scale, can be described by perturbative QCD. However, perturbative QCD is not valid for strong interactions

at low energies. In other words the dynamics of the hard process, e.g. W/Z or Higgs boson production from two hard interacting partons – one from each hadron – can be calculated perturbatively, while the soft processes cannot. To solve this problem a basic property of QCD, factorisation, can be exploited. It allows for a separation of the dynamics at different scales, i.e. hard (short-distance) and soft (long-distance) physics, and the cutoff separating the scales is called factorisation scale μ_f.

The proton–proton cross section can be expressed as a convolution of the hard partonic interaction and the probability to find a parton carrying the fraction x of the proton's momentum [33]:

$$\sigma = \sum \int dx_1 dx_2 f_i(x_1, \mu_f) f_j(x_2, \mu_f) \cdot \hat{\sigma}_{ij} \tag{2.45}$$

where the parton distribution functions ("PDFs") f_i describe the probability to find a quark, anti-quark or gluon i carrying the momentum fraction x_i of the proton momentum. The hard parton cross section $\hat{\sigma}_{ij}$ describes the short distance interaction of the partons from the colliding protons and can be calculated. The PDFs cannot be calculated from first principles, but have to be obtained from fits to experimental data. Many groups provide parametrization of PDFs including uncertainties for the LHC, e.g. the CTEQ [34] and MSTW [35] collaborations. The MSTW PDFs for a four momentum transfer of $Q^2 = 10$ GeV and $Q^2 = 10^4$ GeV are shown in Figure 2.11.

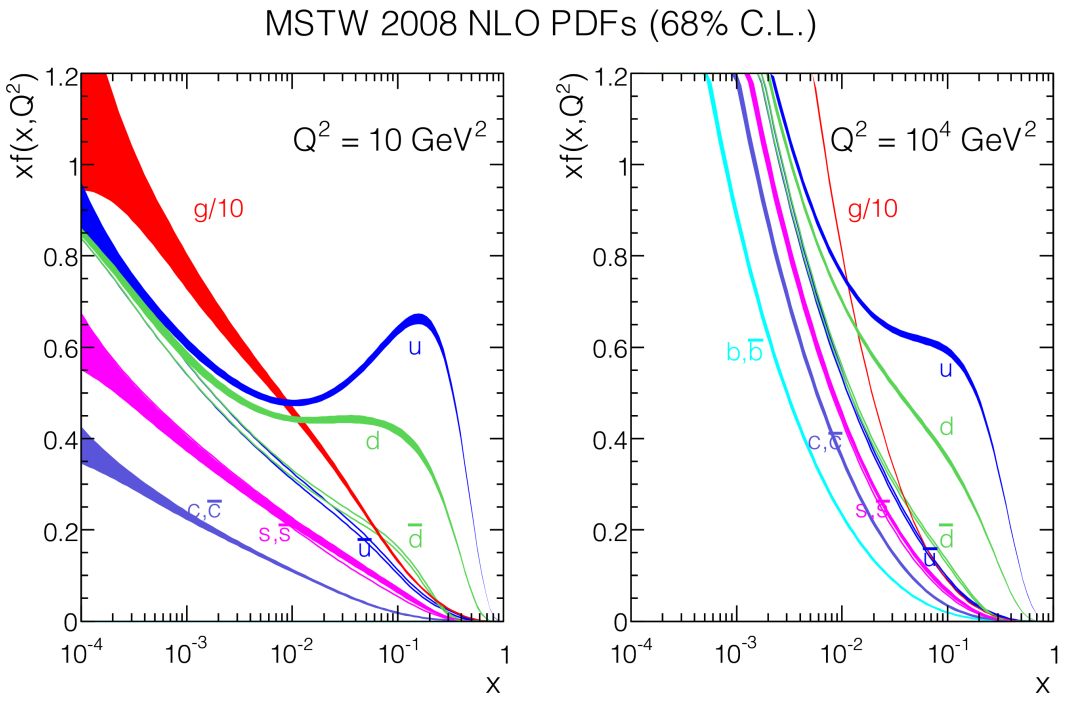

Figure 2.11: MSTW 2008 PDFs for $Q^2 = 10$ GeV and $Q^2 = 10^4$ GeV [35].

In the Standard Model, cross sections can usually not be calculated analytically and therefore need to be expressed in a power series expansion in the coupling constants, i.e. in perturbation theory. Corrections from higher order terms, e.g. loop corrections, can introduce divergences as particles in loops can violate energy and momentum conservation. These unphysical divergences can be absorbed into redefinitions of the coupling constants, masses and fields in a technique referred to as renormalization. The renormalized quantities then correspond to the observable physical ones. The downside of this technique is that an energy scale dependence is introduced and the parameters now depend on the

renormalization scale μ_r. Hence the calculation of the hadronic cross section also depends on μ_r.

In Figure 2.12 the cross sections of important Standard Model processes in dependence of the center-of-mass energy $\sqrt{s}$ is shown. It is noteworthy that for center-of-mass energies of order 10 TeV, rare processes, e.g. Higgs production, happen only in about one out of $\approx 10^{10}$ interactions. Therefore selecting events of interest while rejecting the large backgrounds is of great importance.

2.3.2 Underlying Event and Pileup

In addition to the hard process, the interactions of partons in the proton not involved in the hard process have to be considered to fully describe the events recorded in proton-proton collisions. This is referred to as the "underlying event", e.g. the term underlying event refers to everything of the proton-proton collision but the hard interaction.

Furthermore, as proton beams at the LHC have a bunch structure, more than one proton–proton interaction can occur when two bunches are collided. Hence, more than one hard interaction per "bunch crossing" can happen. This is referred to as ("in-time") "pile-up". On top of this, additional proton-proton interactions from previous bunch crossings can influence the measurement of an event due to overlapping signals in the detector ("out-of-time pile-up").

2.3.3 Hadronization and Jets

The quarks and gluons created in the hard interaction cannot exist freely and need to form color neutral hadrons. The processes in which the partons form hadrons, which then may further decay and can be observed in the detector, is called "hadronization". As it involves non-perturbative aspects of QCD, hadronization can only be described by phenomenological models.

Jets are a concept used to reconstruct the particles resulting from quarks and gluons after the complex process of hadronization. The partons will radiate off other quarks or gluons and the resulting hadrons will in general fly in the same direction as the original quark or gluon. This collimated stream of hadrons is referred to as a jet. Different jet algorithms that group clusters of particles together to form jets exist. In this analysis the so-called "anti-k_T" algorithm [37, 38] is used.

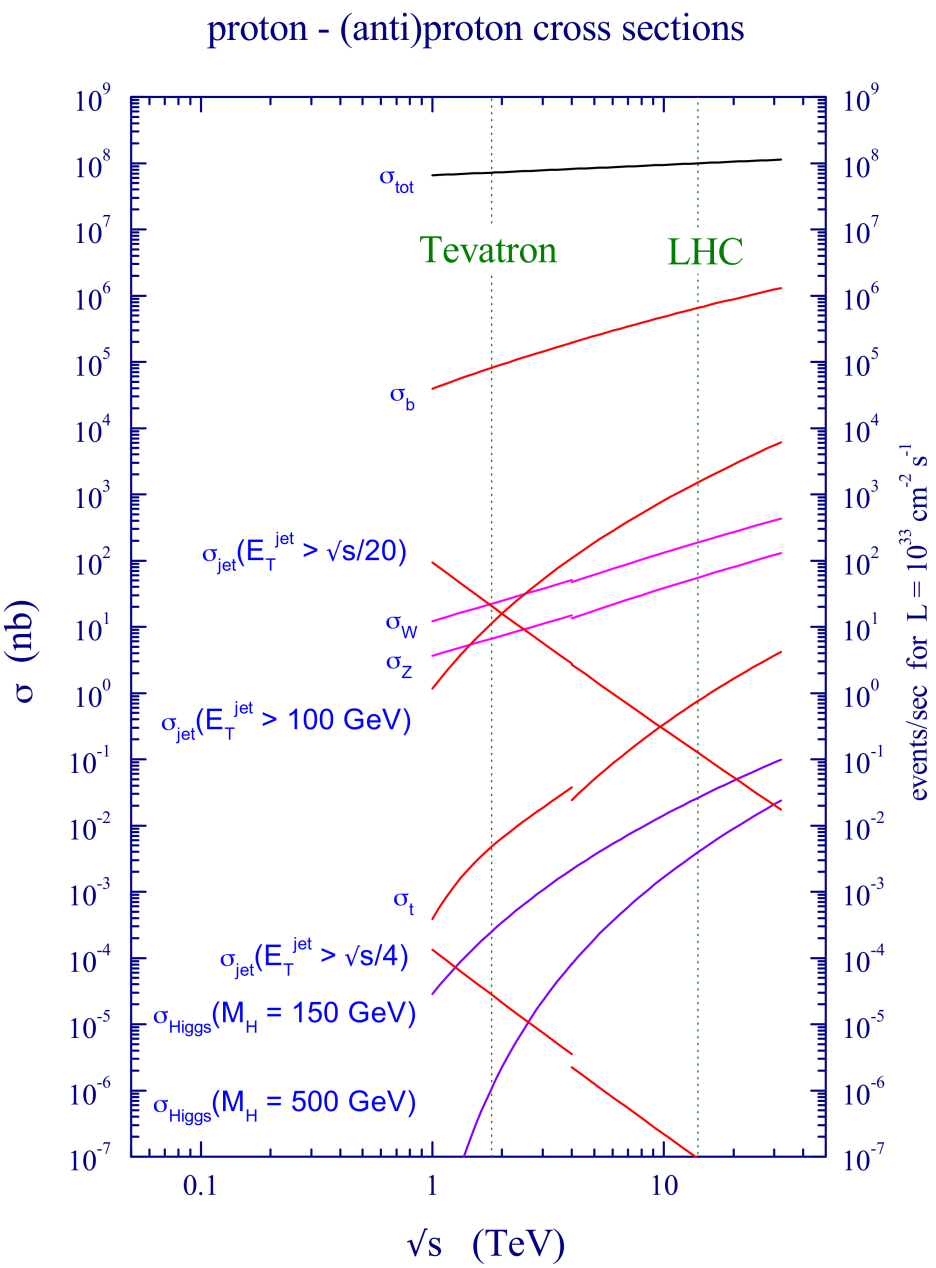

Figure 2.12: Standard Model cross sections at the Tevatron and the LHC colliders as a function of the center-of-mass energy $\sqrt{s}$ [36].

Chapter 3

The ATLAS Experiment at the Large Hadron Collider

The Large Hadron Collider [39] ("LHC") at CERN was designed to deliver high luminosities and unprecedented high energies. Eventually it will collide bunches of up to 10^{11} protons 40 million times per second and provide proton–proton collisions at a center-of-mass energy of $\sqrt{s} = 14$ TeV at a design luminosity of $10^{34}\text{cm}^{-2}\text{s}^{-1}$. In addition, heavy ions, in particular lead nuclei, can be collided. At four interaction points around the accelerator ring large experiments are installed. The two multi-purpose detectors ATLAS [40] ("A Toroidal LHC ApparatuS") and CMS [41] ("Compact Muon Solenoid") have been searching for the Higgs boson and for phenomena of physics beyond the Standard Model like new heavy particles. The LHCb [42] experiment is dedicated to perform precise measurements in the flavor sector of the Standard Model, such as studies of CP violation and the phenomenology of mesons with heavy quarks. ALICE [43] ("A Large Ion Collider Experiment") is designed to investigate heavy-ion collisions and to search for the quark gluon plasma [44].

3.1 The Large Hadron Collider

LHC is installed in the tunnel of the former Large Electron Positron collider [16] (LEP). A schematic overview is shown in Figure 3.1. The tunnel is located about 100 m underground and has a circumference of 27 km. Superconducting dipole magnets that can be kept at a working temperature of 1.9 K using liquid helium cooling are used to keep the protons on bent trajectories. Their nominal magnetic field is 8.3 T, designed for an energy of up to 7 TeV per proton and hence a center-of-mass energy of $\sqrt{s} = 14$ TeV. Quadrupole magnets are used to focus the beams. Using the existing CERN accelerator complex, protons with an energy of 450 GeV are injected into the LHC, where they are further accelerated by superconducting radio-frequency cavities operating at 400 MHz. Bunches of up to 2808 protons with a spacing of about 7.5 m are collided leading to a time of 25 ns between two bunch-crossings or a frequency of about 40 MHz.

In September 2008 the first protons were injected into the LHC, but after only a few days of running a major incident caused by a broken connection between the superconducting magnets cause the machine to be stopped for repairs that took more than a year. Operation restarted in November 2009 and first collisions at $\sqrt{s} = 900$ GeV and $\sqrt{s} = 2.36$ TeV were delivered. First collisions at $\sqrt{s} = 7$ TeV have been provided from March 2010 and to June 2011, only interrupted by a one-month heavy-ion run and a short maintenance period.

The instantaneous luminosities were steadily increased during operation in 2010 and 2011. The highest luminosities achieved were $2 \times 10^{32}\text{cm}^{-2}\text{s}^{-1}$ in 2010 and $3.6 \times 10^{33}\text{cm}^{-2}\text{s}^{-1}$ in 2011 and integrated luminosities of 50 pb^{-1} and 5.6 fb^{-1} were delivered to the ATLAS experiment, respectively. The integrated luminosity over time is shown in Figure 3.2. The average number of interactions per bunch crossing, μ, went up from about $\mu = 3$ in 2010 to above $\mu = 15$ until the end of the 2011 running.

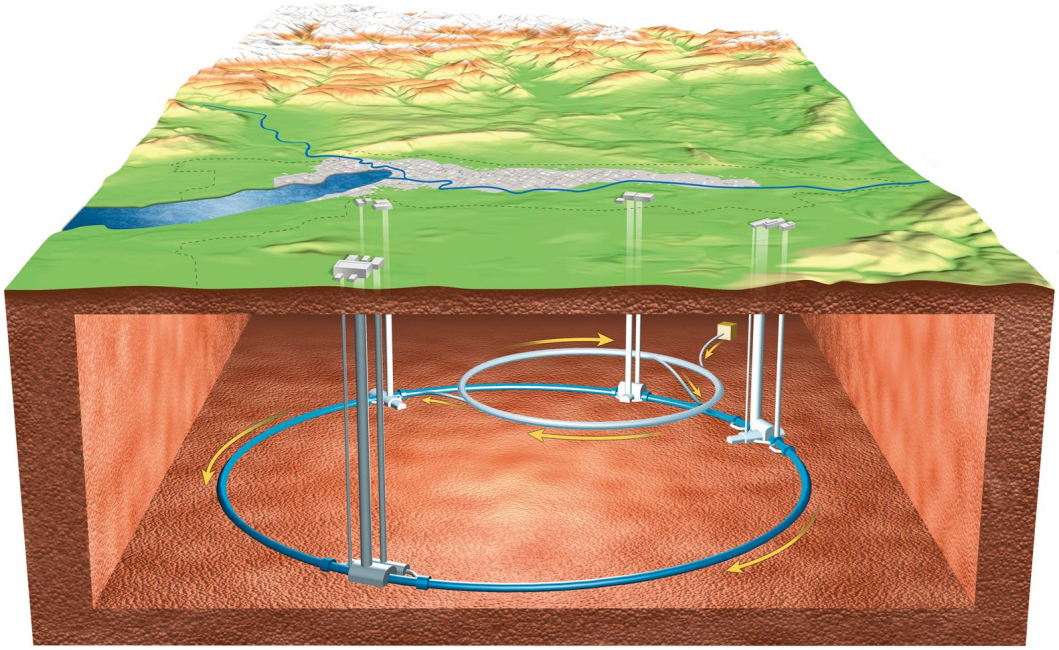

Figure 3.1: Overview of the LHC [45].

In April 2012, the LHC started running at an increased center-of-mass energy of $\sqrt{s} = 8$ TeV and until the beginning of August 2012 an integrated luminosity of 10 fb^{-1} has been delivered by the LHC. The current proton-proton run will continue for the rest of 2012 and be followed by a month of proton–lead collisions in 2013. After that a long technical stop that will last at least until the end of 2014 is planned in order to prepare the machine for $\sqrt{s} = 14$ TeV proton–proton collisions, e.g. by installing additional safety measures to avoid accidents similar to the one that happened in 2008.

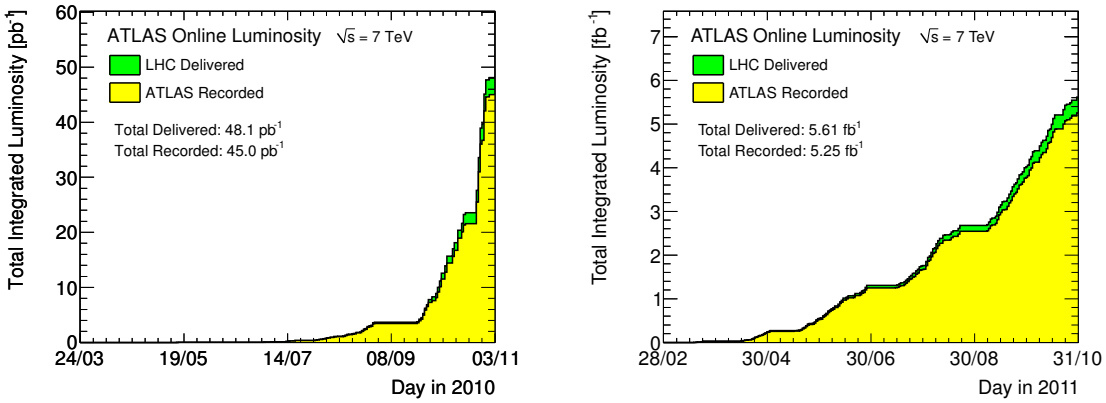

Figure 3.2: Integrated luminosity of proton–proton collisions at a center-of-mass energy of $\sqrt{s} = 7$ TeV delivered to and recorded by the ATLAS experiment for the 2010 (left) and 2011 (right) data taking periods.

3.2 The ATLAS Experiment

The ATLAS experiment is designed as a multi-purpose detector that can be used to measure a wide range of both Standard Model and new physics processes.

As a consequence of the high rate of collisions provided by the LHC, the ATLAS experiment needs to withstand high radiation doses, to resolve vertices from an average of more than 25 pile-up events (at $\sqrt{s} = 14$ TeV) and to be able to trigger events from interesting Standard Model and new physics processes, e.g. Higgs boson production, that have much smaller rates compared to the backgrounds due to Standard Model processes. The ATLAS detector [46] was therefore designed with the following requirements in mind:

- Radiation-hard sensors and electronics; high-granularity sensors.
- Large acceptance in the forward/backward directions with almost full azimuthal coverage.
- Good charged-particle reconstruction efficiency and momentum resolution in the tracking system and vertex detectors close to the interaction region for identifying b-jets and τ leptons via a secondary vertex.
- Very good electromagnetic calorimetry for electron and photon identification/measurements. Full-coverage hadronic calorimetry for accurate jet and missing transverse energy measurements.
- Good muon identification and momentum resolution over a wide momentum range. Reliable charge determination up to highest transverse momenta.
- A fast and flexible trigger system that is highly efficient at selecting events of interest and rejecting the background events.

A brief description of the ATLAS detector is given in the following, focusing on the detector components that are relevant for the analyses. A detailed description of all detector components is given in [40, 46].

The origin of the ATLAS coordinate system is defined by the nominal proton–proton interaction point. The beam direction defines the z-axis and the $x-y$ plane is transverse to the beam direction. The (positive) x-axis points to the center of the LHC ring and the (positive) y-axis points upwards.

The azimuthal angle ϕ is measured around the beam axis and the polar angle θ is the angle with respect to the beam axis. The pseudorapidity is defined as $\eta = -\ln\tan(\theta/2)$, which is equal to the rapidity $y = \ln((E + p_z)/(E - p_z))$ in the limit of massless objects ($E = |\vec{p}|$, where E denotes the energy of the particle and $\vec{p} = (p_x, p_y, p_z)$ is its momentum). The difference in rapidity of two objects is invariant under Lorentz boosts along the beam axis and hence variables that are invariant under boost along the z-axis are preferred. The distance ΔR in the pseudorapidity-azimuthal angle space is defined as $\Delta R = \sqrt{(\Delta\eta)^2 + (\Delta\phi)^2}$.

The transverse momentum p_{T}, is defined with respect to the $x-y$ plane, i.e. $p_{\mathrm{T}} = \sqrt{p_{\mathrm{x}}^2 + p_{\mathrm{y}}^2}$, with p_{x} and p_{y} being the momenta in direction of the x- and y-axis, respectively. Similarly, the missing transverse energy $E_{\mathrm{T}}^{\mathrm{miss}}$ can be defined (see Section 5.2 for more details).

A three dimensional cut-away overview of the ATLAS detector is shown in Figure 3.3. It is forward-backward symmetric with respect to the interaction point and its main sub-detectors extend radially around the beam axis. It consists of three main detector systems:

- The Inner Detector ("ID") is contained in a solenoid magnet which creates a 2 T magnetic field. Trajectories of charged particles are bent in the field and therefore their momenta can be measured

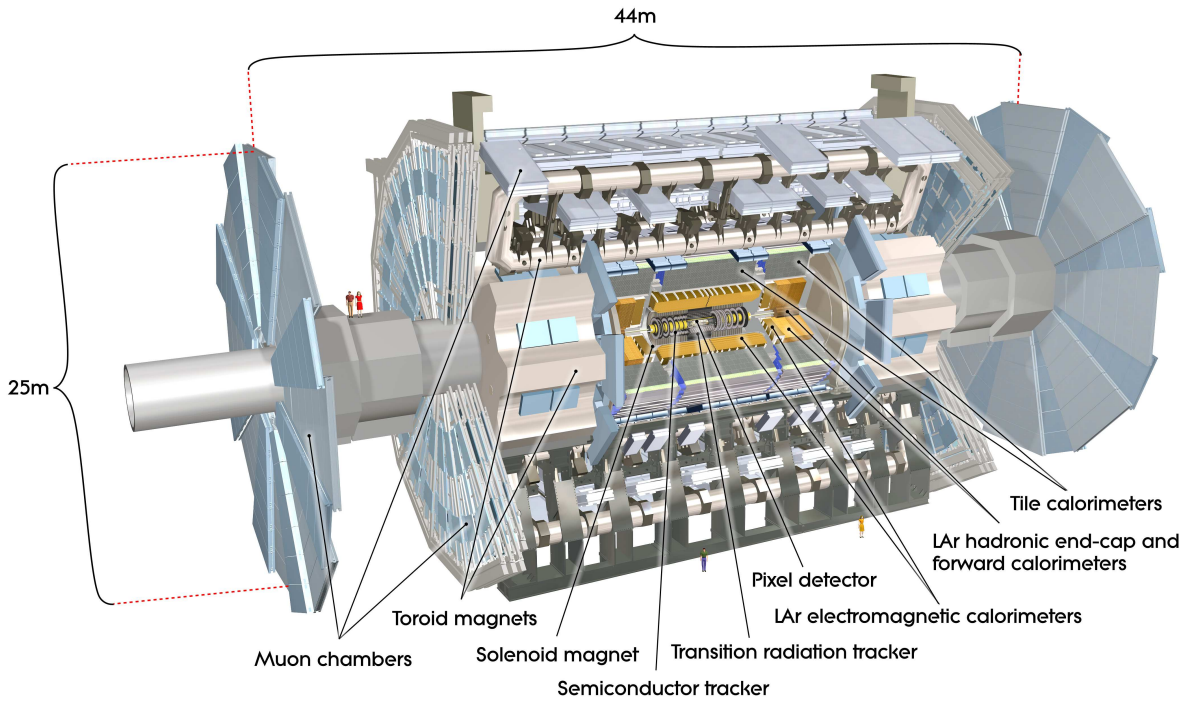

Figure 3.3: Cut-away view of the ATLAS detector [46]. The detector is 25 m high, 40 m long and has a mass of about 7000 tons. The individual components are described in the text.

from three or more space points. A combination of high-resolution semiconductor pixel ("PXD") and silicon microstrip ("SCT") detectors (with a pseudorapidity coverage of $|\eta| < 2.5$) in the innermost part are complemented with a straw-tube tracking detector (with a pseudorapidity coverage of $|\eta| < 2.0$) in the outer part of the tracking volume. The latter is also capable of generating and detecting transition radiation ("TRT"). The ID is used for pattern recognition, momentum and vertex measurements and electron identification.

- The ID is enclosed by high-granularity liquid-argon ("LAr") electromagnetic sampling calorimeters that cover the pseudorapidity range of $|\eta| < 3.2$. In the range of $|\eta| < 1.7$ a scintillator-tile calorimeter is used for hadronic calorimetry. It is complemented by a LAr-based hadronic calorimeter, covering the range of $1.5 < |\eta| < 3.2$. Forward LAr calorimeters covering the pseudorapidity range up to $|\eta| < 4.9$ complete the calorimeter system by providing both electromagnetic and hadronic energy measurements.

- The calorimeter system is surrounded by the muon spectrometer that uses an air-core toroid magnet system to bend the trajectories of charged particles. High precision tracking chambers used to measure the momentum and dedicated fast trigger chambers are installed.

In addition detectors installed in the forward region are used for dedicated luminosity measurements.

To reduce the high event rates from QCD processes, a three-level trigger system is used, consisting of a hardware-based and two subsequent software-based triggers.

3.2.1 Inner Detector

The inner detector is designed to cope with the large track density due to about 1000 particles emerging from the interaction point every 25 ns. To achieve the desired momentum and vertex resolutions (needed to search for new physics phenomena) detectors with a high granularity, in particular close to the interaction point are needed. The space points measured by the PXD and SCT used together with the TRT drift circle measurements at larger distances provide these features. While the TRT is operated at room temperature the silicon based detectors (PXD and SCT) need to be operated at temperatures of approximately $-5°C$ to $-10°C$ and therefore must be cooled. The ID layout is shown in Figure 3.4.

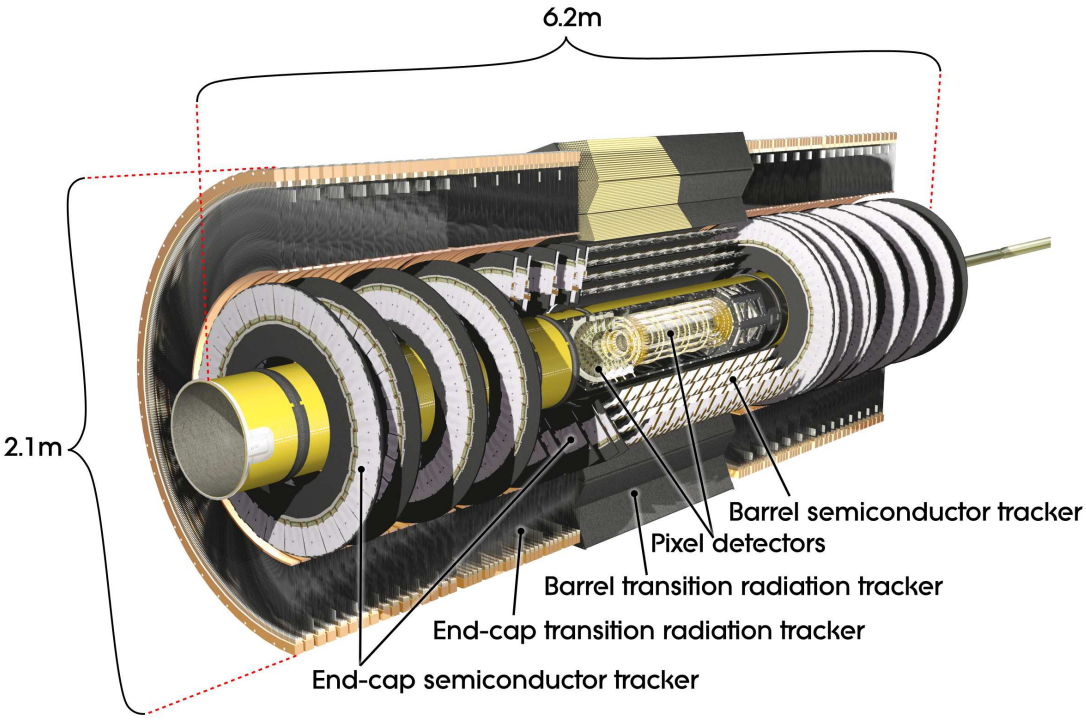

Figure 3.4: Cut-away view of the ATLAS Inner Detector [46].

Pixel Detector

The Pixel detector, located close to the interaction point, has the highest granularity. The detector has approximately 80.4 million readout channels. In the inner central region ($|\eta| < 1.7$, "barrel") the sensors are arranged in layers on three concentric cylinders around the beam axis with radii of 50.5 mm $< R <$ 122.5 mm. In the end-cap region ($1.7 < |\eta| < 2.5$) they are located on three disks in each forward- and backward-direction arranged perpendicular to the beam axis with radii of 88.8 mm $< R <$ 149.9 mm. The layers are segmented in R–ϕ and z, and typically three pixel layers are crossed by each track. All pixel sensors are identical and have a minimum size in R-$\phi \times z$ of 50×400 µm^2. The intrinsic precision of the sensors are 10 µm (R–ϕ) and 115 µm (z) in the barrel and 10 µm (R–ϕ) and 115 µm (R) in the disks.

Silicon Microstrip Detector

Similar to the pixel detector the sensors of the SCT are arranged in cylinders with radii of 299 mm $< R <$ 514 mm in the barrel region ($|\eta| < 1.4$) and on disks with radii of 275 mm $< R <$ 560 mm in the end-cap region ($1.4 < |\eta| < 2.5$). The modules consist of pairs of sensor layers glued together in a back–to–back configuration, tilted by a small stereo angle (40 mrad) in order to measure three dimensional space points. There are four of these double layers in the barrel region, each with one strip oriented parallel to the beam axis. In each end-cap region nine disks, each with one strip oriented radially, are used. Typically eight layers, corresponding to four space points, are crossed by each track in the SCT. The strip pitch is 80 μm in the barrel region and approximately the same in the end-cap regions. In the barrel region the intrinsic precision per module are 17 μm (R–ϕ) and 580 μm (z), and 17 μm (R–ϕ) and 580 μm (R) in the end-cap region respectively. The total number of readout channels in the SCT is approximately 6.3 million.

Transition Radiation Tracker

In the barrel region of $|\eta| < 0.7$, the TRT consists of more than 50000 straw tubes with a diameter of 4 mm and a length of 144 cm. Their wires are divided into two halves (approximately at $\eta = 0$) that are oriented parallel to the beam axis and hence provide only R–ϕ information. In the end-cap region ($0.7 < |\eta| < 2.0$) more than 120000 straw tubes with a length of 37 cm are arranged radially in wheels. The intrinsic precision is 130 μm per straw tube (R–ϕ), about an order of magnitude worse compared to the PXD and SCT. However, the combination of the higher typical number of hits per track (about 36) and the longer lever arm make up for this shortcoming and let the TRT contribute to the overall momentum measurement resolution. In addition, photons created by transition radiation in the material by high momentum electrons and detected in the Xe-based gas mixture in the straw tubes yield much larger signal amplitudes than minimum-ionizing charged particles. To distinguish transition radiation from tracking signals separate low and high thresholds are used in the front-end electronic on a straw-by-straw basis. This effect is used in the electron identification as other charged particles do not emit transition radiation in the TRT. The total number of TRT readout channels is approximately 351000.

Material Distribution in the Inner Detector

As the material in the inner detector significantly affects the event reconstruction, e.g. the energy deposit of particles in the calorimeter, the material distribution has been accurately mapped and introduced into the ATLAS simulation. The material budget can be expressed in terms of radiation length X_0 or interaction length λ. The material distributions are shown in Figure 3.5 both in terms of X_0 and λ.

As a consequence of the material in the detector

- many electrons lose a large part of their energy through bremsstrahlung;
- approximately 40% of all photons convert in an electron–positron pair;
- a significant fraction of low-energy charged pions undergo inelastic hadronic interactions

inside the ID volume before reaching the calorimeters. Therefore understanding the material distribution is important for a reliable reconstruction of particle charge and electron identification.

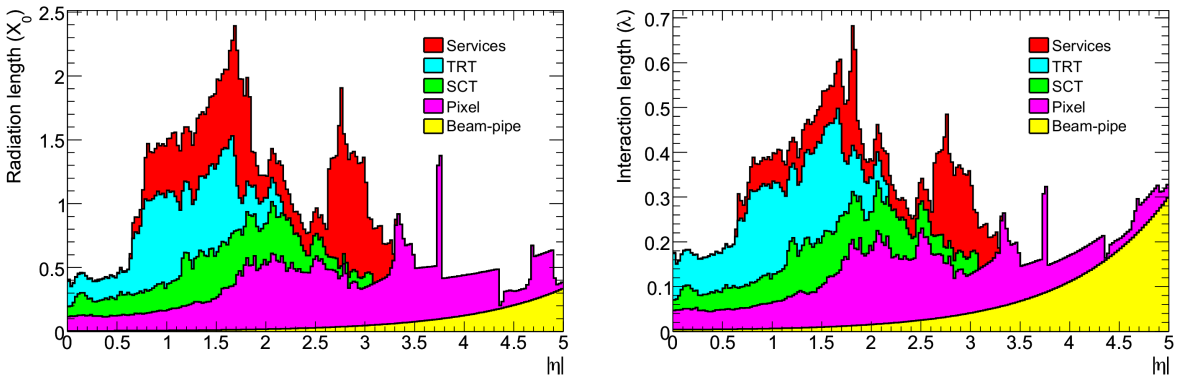

Figure 3.5: Material distribution in terms of radiation length X_0 (left) and interaction length λ (right) at the exit of the ID envelope, including services and thermal enclosures, shown as a function of $|\eta|$ and averaged over ϕ [46].

3.2.2 The Calorimeters

An overview of the calorimeters is shown in Figure 3.6. They are all sampling calorimeters, i.e. they consist of alternating layers of active and absorbing material that measure and absorb energy, respectively. The calorimeters cover a large pseudorapidity range of $|\eta| < 4.9$ using different technologies in order to suit the varying requirements imposed by the different physics processes and the radiation environment over this range. The fine granularity of the electromagnetic calorimeter in the pseudorapidity region matched to the ID is perfectly suited for precision measurements of electrons and photons. The coarser granularity of the rest of the calorimeters is sufficient to satisfy the physics requirements for jet reconstruction and $E_{\mathrm{T}}^{\mathrm{miss}}$ measurements.

As electromagnetic and hadronic showers must be contained in the calorimeters and punch-through to the muon system must be limited, a sufficient calorimeter depth is important. The electromagnetic calorimeter has a total depth of more than 22 radiation lengths in the barrel and more than 24 X_0 in the end-cap regions, respectively. The active material of the hadronic calorimeter is approximately equivalent to 9.7 (10) interaction lengths λ in the barrel (end-cap) region adequate to provide good energy resolution for high-energy jets. The total thickness, including outer support, is 11 λ at $\eta = 0$ and sufficiently reduces punch-through, as was shown with data measurements and detector simulations. The combination of the large pseudorapidity coverage and the sufficient depth allow for good $E_{\mathrm{T}}^{\mathrm{miss}}$ measurements.

LAr Electromagnetic Calorimeter

The EM calorimeter is divided into a barrel part ($|\eta| < 1.475$) and two end-cap components ($1.375 < |\eta| < 3.2$). The end-cap calorimeter is divided into two coaxial wheels, an outer and an inner one, covering the pseudorapidity regions of $1.375 < |\eta| < 2.5$ and $2.5 < |\eta| < 3.2$ respectively. The EM calorimeter is a lead-LAr detector with accordion-shaped kapton electrodes and lead absorber plates over its full coverage. This geometry provides full coverage in ϕ without azimuthal cracks. A sketch of a barrel module is shown in Figure 3.7. Over the central region that is important for many physics measurements ($|\eta| < 2.5$) the EM calorimeter is divided into three sections along its depth. The first layer (about $4X_0$ deep) has the highest granularity of up to $\Delta\eta = 0.0031$ for $|\eta| < 1.8$ and is coarser beyond that. It allows for measuring shower shapes to separate electrons and photons from hadronic objects in the calorimeter and is suited to resolve single photons from π^0 decays. The azimuthal granularity

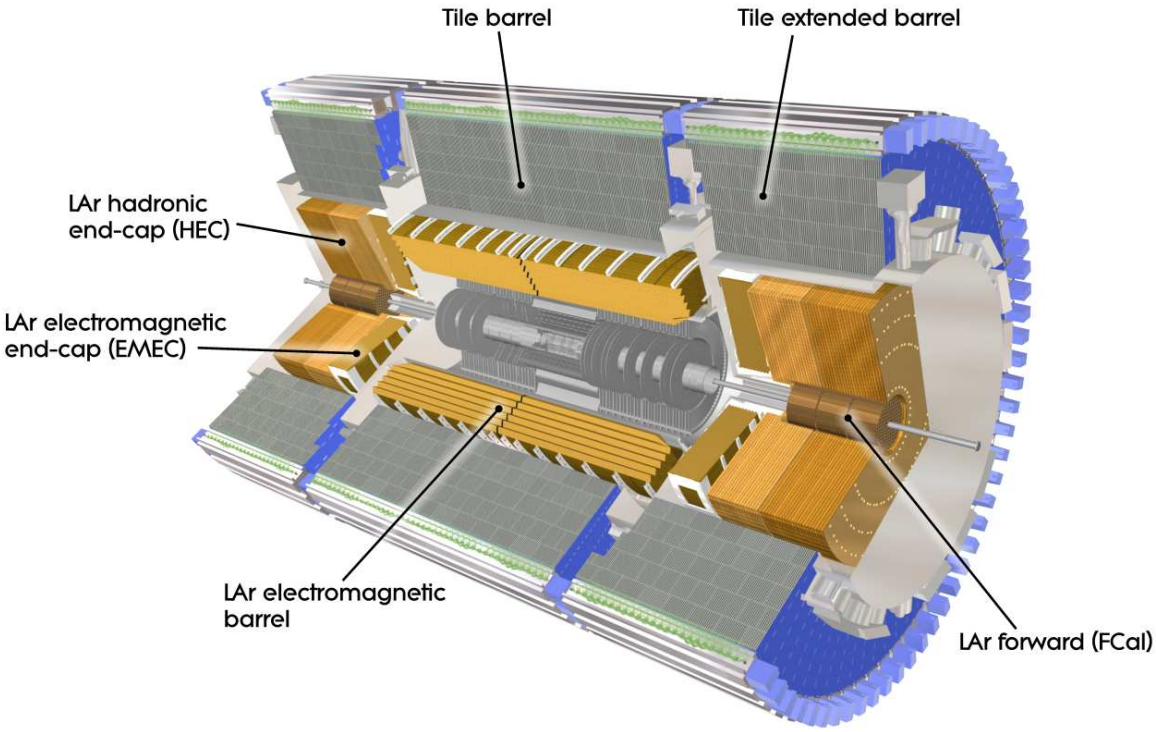

Figure 3.6: Cut-away view of the ATLAS calorimeter system [46].

in the first layer is coarser, with $\Delta\phi = 0.1$. The subsequent two layers have a coarser granularity of 0.025×0.025 in $\Delta\eta \times \Delta\phi$. Most of the energy of electrons and photons is contained within the second layer ($\approx 16X_0$) while the third layer ($\approx 2X_0$) is used to correct for electrons and photons with very high energies. A presampler located in front of the inner barrel region ($|\eta| < 1.8$) and consisting of a thin active LAr layer is used to recover the energy lost in the material of the ID (see Section 3.5). The inner wheel end-cap calorimeter is segmented in two sections in depth and has a coarser lateral granularity than the rest of the EM calorimeter.

The resolution of the EM calorimeter in the barrel according to test beam studies is $\sigma(E)/E = 10\%/\sqrt{E[\text{GeV}]} \oplus 0.17\%$.

Hadronic Calorimeters

The tile calorimeter covers the region $|\eta| < 1.7$ and surrounds the EM calorimeter. It is a sampling calorimeter using steel as the absorber and scintillating tiles as the active material. It is divided into three layers with a granularity of 0.1×0.1 (0.1×0.2) in $\Delta\eta \times \Delta\phi$ in the first two (the third) layers. Two sides of the scintillating tiles are read out by wavelength shifting fibers with two separate photomultiplier tubes. The hadronic end-cap calorimeter ("HEC") covers the pseudorapidity region of $1.5 < |\eta| < 3.2$. It is located in the same cryostat as the LAr EM calorimeter and uses LAr as its active medium as well. Copper plates are used as the passive medium.

The design resolution for jet energies in the hadronic barrel and end-cap calorimeters is $\sigma_E/E = 50\%/\sqrt{E[\text{ GeV}]} \oplus 10\%$.

LAr Forward Calorimeter

The Forward Calorimeter ("FCal") covers the range of $3.1 < |\eta| < 4.9$. It uses LAr as its active medium. The first out of its three layers uses copper as the passive medium and is dedicated for measuring electromagnetic energy deposits. The other two layers use tungsten as the passive medium and are dedicated to measure hadronic energy deposits. The design energy resolution for jets in the FCal is $\sigma_E/E = 100\%/\sqrt{E[\text{ GeV}]} \oplus 10\%$.

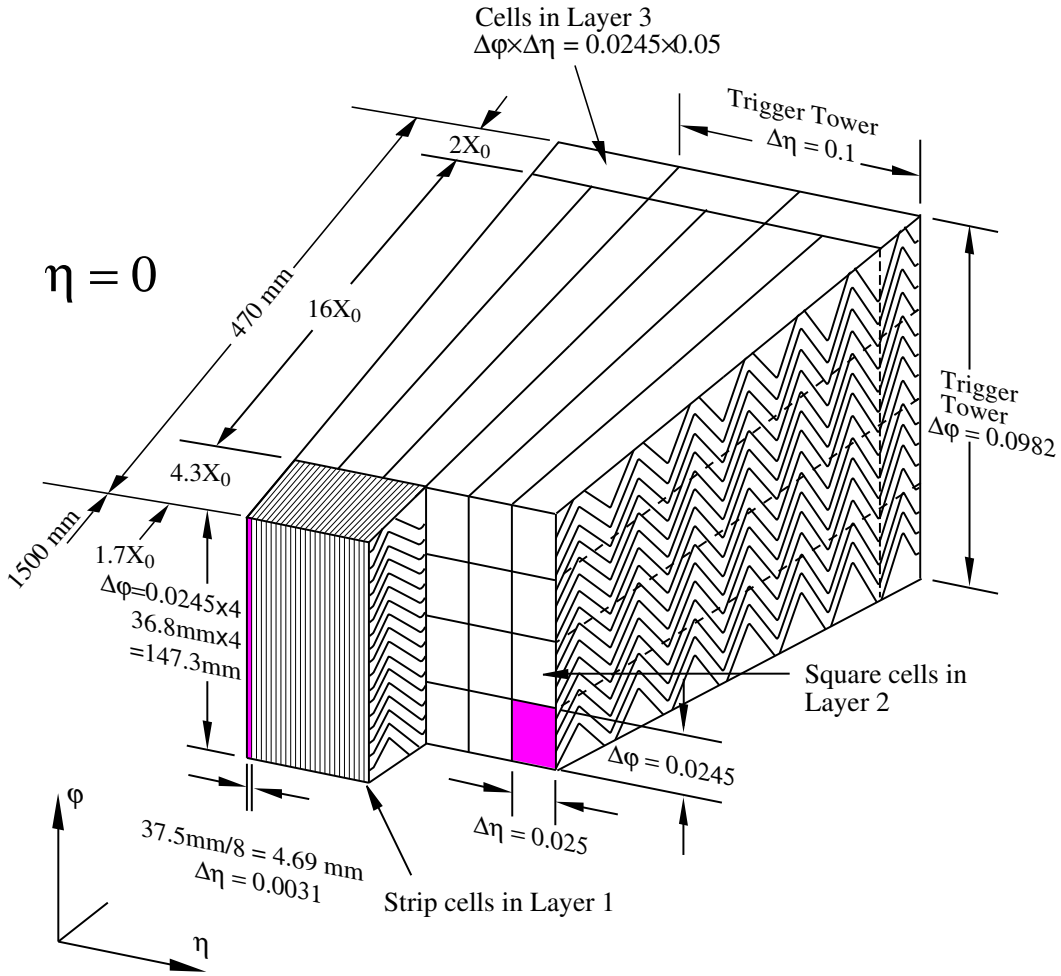

Figure 3.7: Sketch of a barrel module of the LAr electromagnetic calorimeter [46]. The granularity in η and ϕ of the cells of each of the three layers and of the trigger towers is also shown. In the trigger system not the full granularity of the calorimeter is used to improve the read-out speed and hence coarser projective towers are read out. They are referred to as "trigger towers".

3.2.3 The Muon System

The muon system encloses the rest of the detector and is the subdetector with the largest volume.

Its layout is shown in Figure 3.8. Charged particle trajectories are bent by large superconducting air-core toroid magnets, hence the bending is orthogonal to that in the solenoid field in the ID. The central region ($|\eta| < 1.4$) is covered by the large barrel toroid, while two smaller toroids cover the end-cap

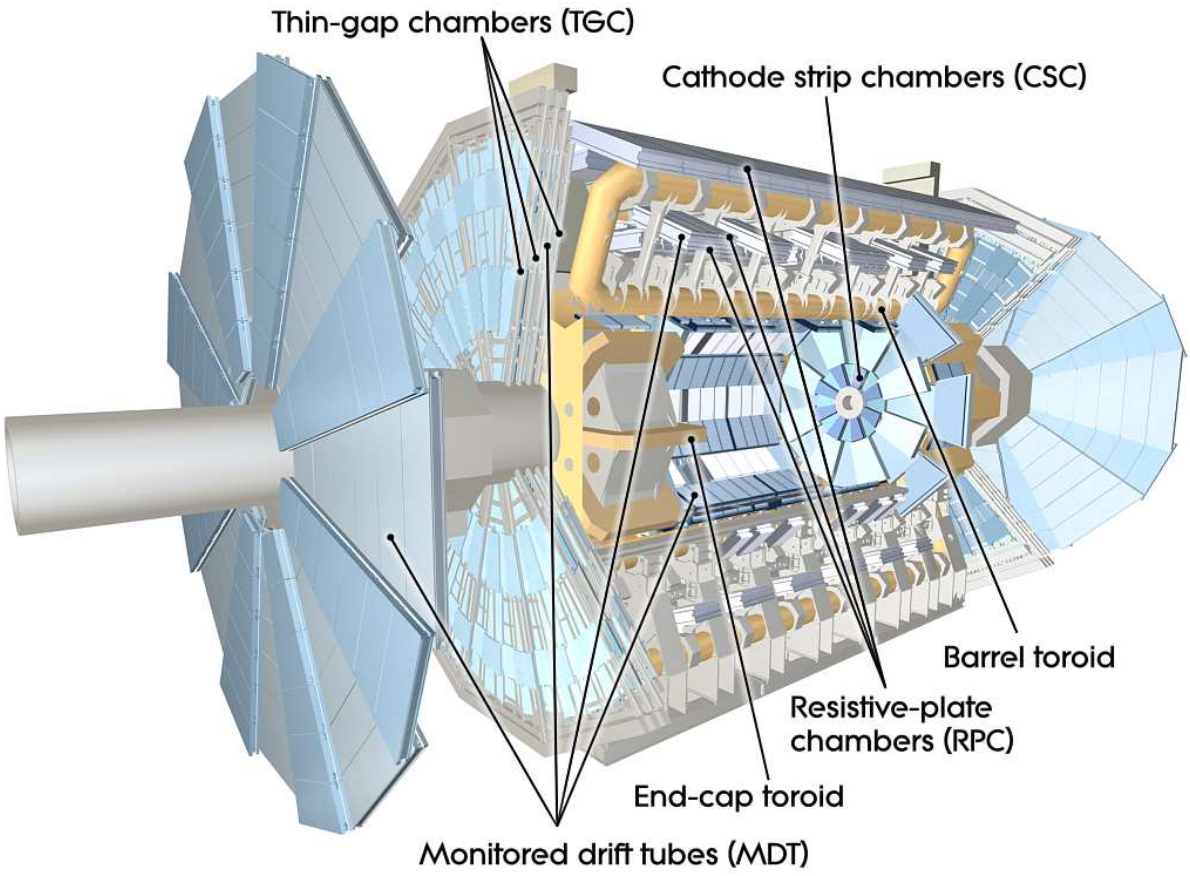

Figure 3.8: Cut-away view of the ATLAS muon system. [46].

region ($1.6 < |\eta| < 2.7$). In between ($1.4 < |\eta| < 1.6$) magnetic bending is provided by a combination of barrel and end-cap fields[1].

For most of the pseudorapidity range, precision measurements of the track coordinates are provided by Monitored Drift Tubes ("MDT"). Cathode Strip Chambers ("CSC"), which are multiwire proportional chambers with cathodes segmented into strips, provide higher granularity and are therefore used in the innermost plane in the pseudorapidity region $2 < |\eta| < 2.7$. For fast triggering within the pseudorapidity range $|\eta| < 2.4$ the barrel region is equipped with Resistive Plate Chambers ("RPC"), while in the end-cap regions Thin Gap Chambers ("TGC") are used.

3.2.4 Forward Detector Systems

The forward region is covered with three smaller detector systems. The first two systems measure the luminosity delivered to ATLAS. LUCID, the Luminosity measurement using Cerenkov Integrating Detector, is located at $z = \pm 17$m from the interaction point and detects inelastic p–p scattering in the forward region. It is the main online luminosity monitor for ATLAS. The second detector ALFA (Absolute Luminosity For ATLAS) located at $z = \pm 240$ m consists of scintillating fiber trackers located inside Roman pots designed to approach as close as 1 mm to the beam. The third system is the Zero-Degree Calorimeter ("ZDC"), located at $z = \pm 140$ m, which is mainly used for measuring the centrality of heavy-ion collisions[2].

3.2.5 Trigger System

The trigger system fore-mostly needs to reduce the high event rates that are due to background processes, while maintaining high efficiencies for interesting events. The hardware-based first trigger ("L1") uses information from the calorimeter and the muon systems. It searches for high-transverse-momentum muons, electrons, photons, jets, and τ leptons decaying into hadrons, as well as large missing and total transverse energy. This information is used to define one or more regions of interest ("RoI") in η and ϕ. Only a subset of the detectors is read out with coarser granularity. A trigger decision takes less than 2.5 µs and the rate is reduced from 40 MHz to $75 - 100$ kHz.

The RoIs are passed to the software-based second trigger level ("L2") and are then analyzed using all sub-detectors with their nominal granularity. L2 decisions are made within approximately 40 ms and the event rate is reduced to roughly 3.5 kHz.

The final trigger stage, the event filter ("EF") utilizes the full detector information and further reduces the event rate to about 300Hz. The processing time for each event is of the order of four seconds and the events passing the EF are permanently stored and have a typical size of about one to two MB. The stored events can then be further reprocessed and distributed for physics analyses.

[1] The "bending power" can be characterized as the field integral $\int Bdl$, where B is the magnetic field component perpendicular to the muon direction. The barrel (end-cap) toroid provides 1.5 to 5.5 Tm (approximately 1 to 7.5 Tm) of bending power.

[2] Centrality describes the "overlap" of the nuclei in a heavy-ion collision, where 100%, 50% and 0% centrality correspond to a central collision, half the nuclei overlapping and no overlapping, respectively.

Chapter 4

Datasets and Cross Sections

In the following the data collected with the ATLAS detector and the signal and background samples from Monte Carlo simulations used in this analysis are presented.

The typical event topology of a hard interaction and the underlying event (as discussed in Section 2.3) is reproduced in the Monte Carlo simulations. First the hard interaction of the colliding partons, taking into account the PDFs and also the decay of short lived heavy particles like the Z boson is calculated up to a certain precision in perturbation theory, usually next-to-leading order. Then higher order processes like initial and final state radiation (ISR/FSR) are added to the calculation. This is followed by a hadronization step where particles carrying color form color neutral hadrons, that then, if short lived, decay further to final state particles. In addition, the proton remnants from the underlying event are considered and additional pile-up events are overlayed.

The generated event, i.e. the four vectors of the final state particles, is then passed through a full simulation of the ATLAS detector based on GEANT4 [47, 48] and the standard ATLAS reconstruction algorithms are applied. The simulated events are reconstructed in exactly the same way as the data events. Reconstructed data and simulated events contain, e.g. information on charged particle tracks, calorimeter energy clusters and reconstructed particles. In addition, simulated events include information on what process is generated, what particles are produced, what their four momenta are, etc.

Some generators produce certain types of events more often than they would be produced in p–p collisions and must therefore correct this by reweighting these events to the correct probability, using so-called generator event weights.

4.1 ATLAS Data

The data used in the following were recorded with the ATLAS detector in proton-proton collisions at a center-of-mass energy of $\sqrt{s} = 7$ TeV during the 2011 LHC run. The integrated luminosity of the data sample, considering only data recorded when the detector was fully operational, is 2.08 fb^{-1}. Fully operational in this context means that almost all the detector systems were working properly to allow for a reliable reconstruction of all final state particles used in this analysis (see Chapter 5). The distribution of the average number of interactions per bunch crossings, μ, for this dataset is shown in Figure 4.1, the mean is $< \mu >= 6.1$.

4.2 Signal Samples and Cross Sections

Simulated samples of Higgs bosons that are produced in the gluon-fusion and the b-quark associated processes are used to estimate the expected yield of neutral MSSM Higgs boson decays in dependence of the parameters m_A and $\tan\beta$. The production in association with W/Z bosons and the vector boson

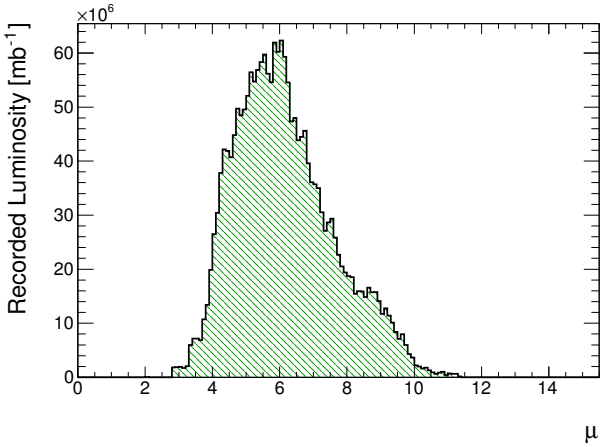

Figure 4.1: Average number of interactions per bunch crossing μ.

fusion production processes are negligible as the couplings are small or non existent in case of the CP-odd Higgs boson A.

The masses, couplings, and branching ratios of the Higgs bosons are computed with FeynHiggs [49]. Details of the calculations and the associated strong coupling constant α_S, PDFs and scale uncertainties can be found in [50].

The direct $gg \to A/H/h$ production is simulated with POWHEG [51], and the associated $b\bar{b}A/H/h$ production with SHERPA [52], where only the processes involving the Higgs boson A are simulated. Both $gg \to A$ and $b\bar{b}A$ samples are generated at values of m_A in the range from 90 to 600 GeV and for $\tan\beta = 20$. There is a small dependence of the Higgs bosons' natural widths on $\tan\beta$. The effect is illustrated in Table 4.1 for the Higgs boson A and a few values of its mass m_A and of $\tan\beta$. The widths of the h and H Higgs boson are of the same order or smaller. As this variation of the width in dependence of $\tan\beta$ is small compared to the experimental mass resolution, the samples can be used to estimated the signal yields for other values of $\tan\beta$ as well, by normalizing them using the appropriate cross sections (see Section 2.2.2 for details).

	125GeV	200GeV	300GeV
5	0.05%	0.1%	0.3%
20	0.7%	0.7%	0.8%
30	1.5%	1.4%	1.4%

Table 4.1: Total width of the Higgs boson A (in percent of its mass) for a few values of its mass m_A and of $\tan\beta$ [49].

The samples are also used for the decays of the H and h bosons, by using the generated sample with the mass m_A closest to the calculated mass M_H or m_h. For any given combination of m_A and $\tan\beta$, the masses M_H and m_h of the H and h bosons are calculated in the m_h^{max} scenario [29]. For $m_A = 120$ GeV and $\tan\beta = 20$ the masses are $m_h \approx 118$ GeV and $M_H \approx 130$ GeV, thus the $gg \to A$ and $b\bar{b}A$ samples simulated with $m_A = 120$ GeV are used to simulate the decays of the h and A Higgs bosons and the sample with $m_A = 130$ GeV is used for the H Higgs boson. A signal sample for $A/H/h$ production at each point is then obtained by combining the $gg \to A$ and $b\bar{b}A$ samples scaled according to the cross sections for h, H and A production.

The cross sections for Higgs boson production in the gluon fusion process have been calculated using HIGLU [53] and ggh@nnlo [54]. For the b-quark associated production, two approaches to calculate the cross section are commonly used, the four-flavor scheme [55, 56] that does not consider b-quarks as partons in the proton and the five-flavor scheme [57] that does. If all orders in perturbation theory could be taken into account the schemes would yield identical results. Currently, the cross sections are available at next-to-leading order and next-to-next-to leading order for the four-flavor and the five-flavor scheme, respectively. A matching scheme described in [58] is used to combine the two approaches. It interpolates between the asymptotic limits of very small ($M_H/M_b \to 1$) and very high ($M_H/M_b \to \infty$) Higgs boson masses where the four- and five-flavor scheme offer unique descriptions, respectively. In both cases, the MSTW2008 set of parton distribution functions (PDFs) [35] has been used.

The signal cross section times branching ratio are shown in Table 4.2 for $\tan\beta = 20$ at $m_A = 120$, 200 and 300 GeV.

Signal process	m_A	$\sigma \times \mathrm{BR}\ [pb]$
$b\bar{b}A/H/h(\to \tau\tau)$	120 GeV	7.62/0.69/7.3
$gg \to A/H/h(\to \tau\tau)$	120 GeV	4.93/2.21/4.1
$b\bar{b}A/H/h(\to \tau\tau)$	200 GeV	0.49/0.49/0.02
$gg \to A/H/h(\to \tau\tau)$	200 GeV	0.13/0.16/0.46
$b\bar{b}A/H/h(\to \tau\tau)$	300 GeV	0.02/0.03/0.002
$gg \to A/H/h(\to \tau\tau)$	300 GeV	0.003/0.005/0.11
Background process		$\sigma\ [pb]$
$W \to \ell\ (\ell = e, \mu, \tau)\ \nu_\ell$		10.5×10^3
$Z/\gamma^* \to \ell^+\ell^-\ (m_{\ell\ell} > 10\ \mathrm{GeV})$		4.96×10^3
Diboson (WW, WZ and ZZ)		46.2, 18.0, 5.6
$t\bar{t}$		165
Single-top (t-, s- and Wt-channels)		58.7, 3.9, 13.1

Table 4.2: Cross sections for signal and background processes. For $A/H/h$ production, the cross section is multiplied by the branching ratio for $A/H/h \to \tau^+\tau^-$. The signal cross sections are given for $\tan\beta = 20$ and the three values quoted correspond to $A/H/h$ production, respectively. For $m_A = 120/200/300$ GeV and $\tan\beta = 20$, the H and h boson masses in the m_h^{max} scenario are $M_H = 132/200/300$ GeV and $m_h = 118/130/130$ GeV.

4.3 Background Samples and Cross Sections

The cross sections of the considered Standard Model background processes are listed in Table 4.2, with the notable exception of the QCD multi-jet background, that will be estimated from data control regions.

The most important background processes in this MSSM Higgs boson search are those where real leptons are produced. In the following, the considered background processes are described.

- **W and Z boson production:** Production of W and Z[1] bosons that subsequently decay into leptons is the most important source of backgrounds. W and Z decays can involve light leptons or τ leptons and missing transverse energy $E_{\mathrm{T}}^{\mathrm{miss}}$ if neutrinos are produced. In Figure 4.2 the production of a Z boson in a proton–proton collision with a subsequent decay to electrons is illustrated.

[1] Instead of a Z boson, a virtual photon γ^* can mediate the decay and lead to the same final state.

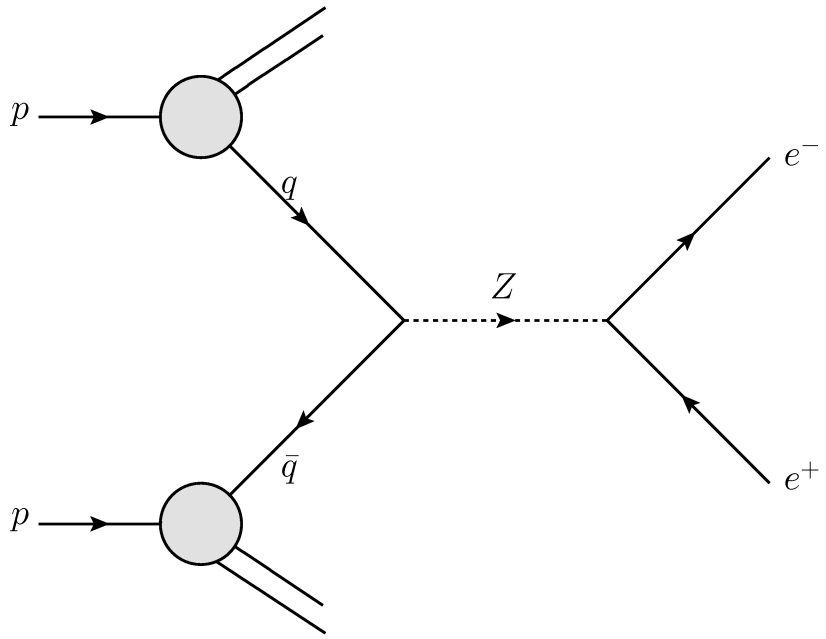

Figure 4.2: Feynman graph of the proton–proton to $Z/\gamma^* \to e^+e^-$ process.

  - $Z/\gamma^* \to \tau^+\tau^-$: This is the most important background process, especially at lower Higgs boson masses, as it has exactly the same signature as the signal process and hence is irreducible. Therefore reconstructing the di-τ mass with high resolution is very important in order to distinguish the signal from this background.
  - $Z/\gamma^* \to e^+e^-/\mu^+\mu^-$+ jets: Decays of the Z boson into electrons or muons in combination with a jet or with one of the light leptons accidentally reconstructed as a τ_{had} candidate also mimic the signal signature. As no neutrinos are involved, missing transverse energy $E_{\text{T}}^{\text{miss}}$ mostly originates from mis-measurement of the jets produced in association with the Z boson.
  - W + jets: A real τ_{had} candidate ($W \to \tau\nu_\tau$) or a real light lepton ($W \to \ell\nu_\ell$) are produced in combination with missing transverse energy $E_{\text{T}}^{\text{miss}}$ from the neutrinos. Hence either a light lepton or a τ_{had} candidate has to originate from mis-identification of a jet produced in association with the W boson.
  - Diboson: While the production of WW, WZ or ZZ can potentially mimic the signal signature if the bosons decay into τ_{had} candidates, light leptons and neutrinos it is a minor background process due to the small cross section (see Table 4.2).

- **$t\bar{t}$ and single top production:** As top quarks decay almost always into a W boson and a b quark that both can produce light leptons, τ_{had} candidates and neutrinos in their subsequent decays processes involving top quarks can mimic the signal signature. In Figure 4.3 $t\bar{t}$ production in proton–proton collisions, with the top quarks subsequently decaying into leptons and quarks is illustrated. Leptons originating from semi-leptonic decays of the b quarks are mostly not isolated as the b quarks will be boosted and therefore all its decay products, including the light leptons, will be close to each other and form a jet. Hence they can be distinguished from isolated leptons originating from W, Z or signal decays.

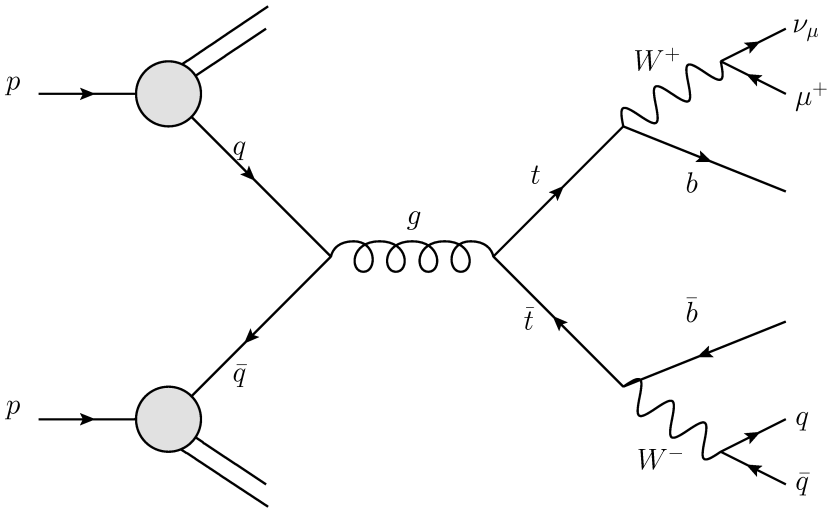

Figure 4.3: Feynman graph of the proton–proton to $t\bar{t}$ process, with the top quark decaying leptonically and its anti-particle decaying hadronically.

- **QCD multi-jet production:** In QCD multi-jet events no real leptons are produced in the initial hard scattering. However, due to the large QCD multi-jet production cross section, QCD processes where jets are accidentally reconstructed as lepton candidates or where real leptons are produced in secondary heavy quark decays cannot be neglected. Due to the rareness of these processes it is impossible to generate a sufficiently large dataset. Due to this and also due to the large uncertainties on the production cross section, the QCD multi-jet background component will be estimated from data control regions and no simulated event samples are used.

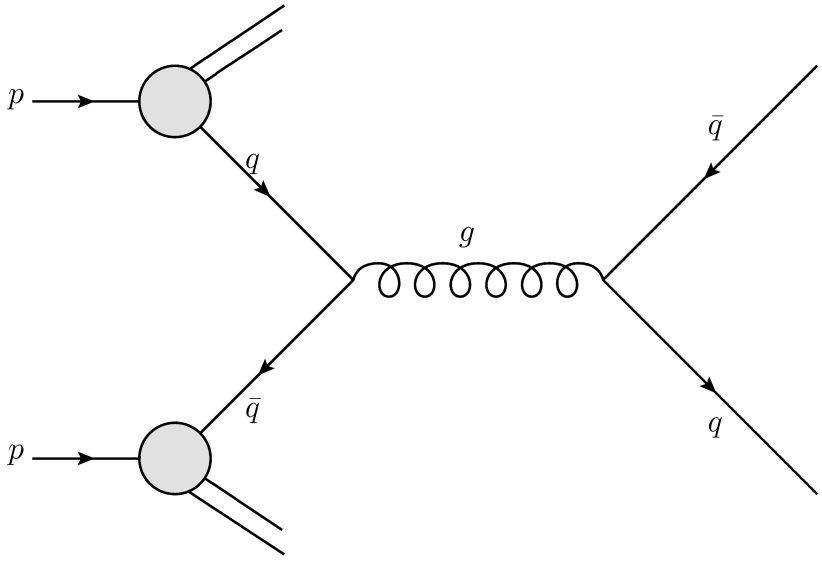

Figure 4.4: Feynman graph of the proton–proton to QCD di-jets process.

The production of W and Z bosons in association with jets is simulated with the ALPGEN [59] generator. The $t\bar{t}$ and single-top processes are generated with the MC@NLO [60] and ACER MC [61] generators, respectively. For diboson production, the HERWIG [62] and MC@NLO generators are used. The loop-induced process $gg \to WW$ is generated with gg2WW [63]. For events generated with the ALPGEN, HERWIG, MC@NLO, and gg2WW, parton shower and hadronization are simulated with HERWIG and the underlying event with JIMMY [64]. The program TAUOLA [65, 66] is used to model the decays of τ leptons in all samples except those generated with SHERPA which handles them internally. The QED radiation in decays, is simulated by PHOTOS [67], again with the exception of samples simulated with SHERPA.

In Table 4.3 an overview of the processes simulated, the generators used and the numbers of generated events is shown.

Process	Generator	Number of generated Events
$b\bar{b}A$	SHERPA	5×10^4 (for each m_A)
$gg \to A$	POWHEG	5×10^4 (for each m_A)
$W \to \ell$	ALPGEN	1.1×10^7 (for each e, μ, τ)
$Z/\gamma^* \to \ell^+\ell^-$	ALPGEN	1.0×10^7 (for each e, μ, τ)
Diboson (WW, WZ and ZZ)	HERWIG/MC@NLO	$(1.8/0.2/0.3) \times 10^6$
$t\bar{t}$	MC@NLO	1.6×10^7
Single-top (t-, s- and Wt-channels)	ACER MC	$(6/6/3) \times 10^5$

Table 4.3: Generator used and number of generated events for the simulated signal and background processes.

Chapter 5

Event Selection

In this chapter the signal selection is introduced. Starting with the trigger selection used, each part of the event selection is described. The reconstructed physics objects – with a focus on the hadronic τ decay candidates – are discussed and the more advanced selection criteria that help to distinguish signal from background events are motivated.

5.1 Trigger

The data was recorded using a single-electron trigger for the $e\tau_{\text{had}}$ and a single-muon trigger for the $\mu\tau_{\text{had}}$ final state. Only events from data-taking periods where the detector and all sub-systems were fully operational are considered.

The p_{T} threshold for the single-muon trigger is 18 GeV over the whole data-taking period. For the single-electron trigger the p_{T} thresholds are 20 GeV in earlier data-taking periods – while lower instantaneous luminosity was delivered by LHC – and 22 GeV in later periods (with an integrated luminosity of 1.4fb^{-1} at 20 GeV and of 0.7fb^{-1} at 22 GeV). To ensure that the triggers are in the plateau of their efficiency curves the event selection described below (Section 5.3) requires sufficiently higher thresholds.

The trigger efficiencies are 99% and 82% for electrons and muons [7], respectively.

5.2 Object Definition

5.2.1 Electrons

Electron candidates are reconstructed from energy clusters in the electromagnetic calorimeter that are matched to an inner detector track. Clusters are identified as an electron candidate if they have a profile consistent with an electromagnetic shower. In Figure 5.1 the electron identification efficiency versus the transverse energy E_{T} and versus the pseudorapidity $|\eta|$ of the electron candidate is shown. The efficiencies shown have been determined with $Z/\gamma^* \to e^+e^-$ simulated samples [68]. Results using the data recorded in 2011 are not publicly available yet. However, as presented in Figure 5.2 similar efficiency distributions were obtained from $W \to e\nu$ events selected in 2010 data and simulated samples [69].

The three standard ATLAS 2011 (i.e. as in Figure 5.1) electron identification working points, called "loose", "medium" and "tight" correspond to efficiencies for e.g. electrons with transverse momenta $p_{\text{T}} = 18$ GeV of roughly 90%, 82% and 60%, respectively. In the following electron candidates that satisfy the tight selection criteria are used, unless stated otherwise.

Electron candidates are required to have a transverse energy $E_{\text{T}}^e > 20$ GeV and to be in the fiducial volume of the barrel and endcaps ($|\eta| < 1.32$ or $1.52 < |\eta| < 2.47$). For the final event selection (see Section 5.3) electrons are required to have transverse momenta $E_{\text{T}}^e > 25$ GeV, in order to assure that the triggers are fully efficient.

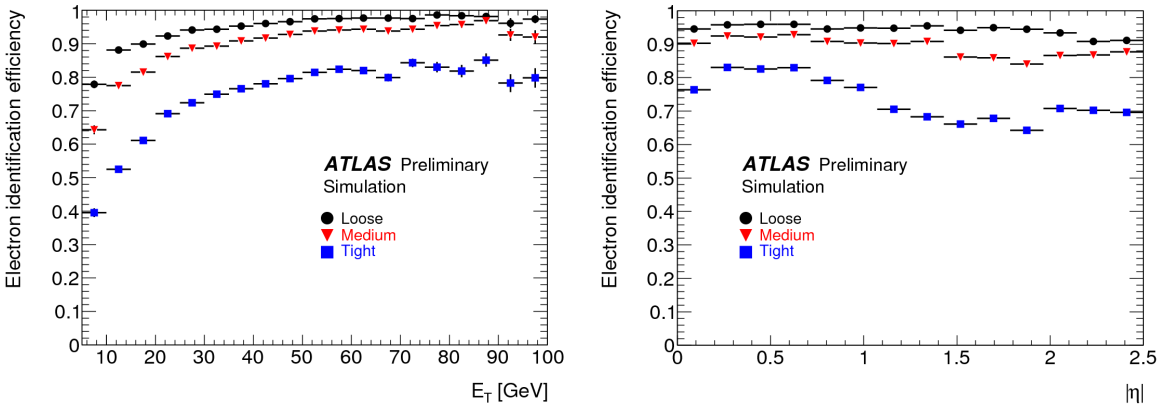

Figure 5.1: Distribution of the electron identification efficiency versus the transverse energy E_T and the pseudorapidity $|\eta|$ of the electron candidate for the loose, medium and tight working points for $Z/\gamma^* \rightarrow e^+e^-$simulated events [68].

Calorimeter isolation is imposed by requiring that the calorimeter energy in a cone of radius $\Delta R = 0.2$ around the electron direction is less then 8% of the electron's transverse energy[1]. In addition, the sum of the transverse momenta of all tracks with $p_T > 1$ GeV in a cone of radius $\Delta R = 0.4$ around the candidate's direction must be less then 6% of its track transverse momentum[2]. The combination of these track and calorimeter isolation requirements will be referred to as "isolation" in the following.

5.2.2 Muons

Muon candidates are reconstructed from tracks found in the muon spectrometer[3] that are matched to tracks found in the inner detector. The muon identification efficiency versus the pseudorapidity η of the muon candidate determined in data and simulation by reconstructing $Z/\gamma^* \rightarrow \mu^+\mu^-$ decays [70] is shown in Figure 5.3.

Muon candidates are required to have a transverse momentum $p_T^\mu > 10$ GeV and a pseudorapidity $|\eta| < 2.5$. For the final event selection (see Section 5.3) muons are required to have transverse momenta $p_T^\mu > 20$ GeV, in order to assure that the trigger is fully efficient. Calorimeter isolation is imposed by requiring that the energy deposited in a cone of radius $\Delta R = 0.2$ centered around the muon direction is less than 4% of its transverse momentum. In addition, the sum of the transverse momenta of all tracks with $p_T > 1$ GeV in a cone of radius $\Delta R < 0.4$ around the muon direction is required to be smaller than 6% of the muon track transverse momentum.

[1]The calorimeter isolation variable will be referred to as $E_T^{\Delta R<0.2}/p_T$ in the following.
[2]The track isolation variable will be referred to as $p_T^{\Delta R<0.4}/p_T$ in the following.
[3]The reconstruction is initiated locally in a muon chamber by searching for straight line track segment in the bending plane that point to the center of ATLAS. This is referred to as "Chain 1" muon reconstruction, while the alternative called "Chain 2" is based on global pattern recognition in the full muon spectrometer.

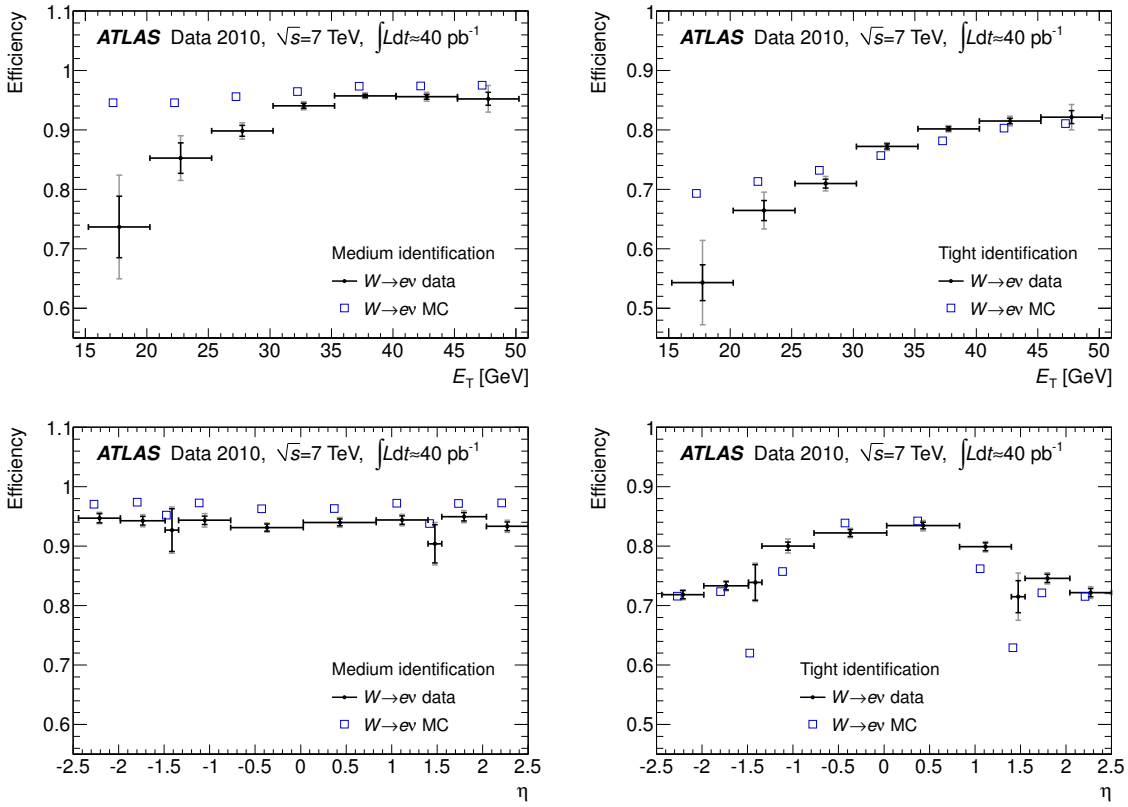

Figure 5.2: Distribution of the electron identification efficiency versus the transverse energy E_{T} (top, integrated over $|\eta| < 2.7$, ignoring the transition region $1.37 < |\eta| < 1.52$) and the pseudorapidity η (bottom, integrated over $20 < E_{\mathrm{T}} < 50$ GeV) of the electron candidate for the medium (left) and tight (right) working points for $W \to e\nu$ simulated and data events [69]. The results for the data are shown with their statistical (inner error bars) and total (outer error bars) uncertainties. The statistical error on the MC efficiencies plotted as open squares is negligible. For clarity, the data and MC points are slightly displaced horizontally in opposite directions.

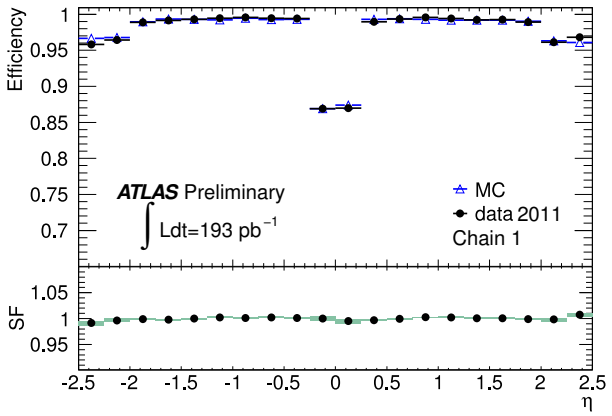

Figure 5.3: Distribution of the muon identification efficiency versus the pseudorapidity η of muon candidates with $p_{\mathrm{T}} > 20$ GeV, determined from reconstructed $Z/\gamma^* \to \mu^+\mu^-$decays in data and simulation [70]. "Chain 1" refers to the way the muon reconstruction is initiated[3]. The panel at the bottom shows the ratio of the efficiencies measured in data and simulation [70].

5.2.3 Jets

Jets are reconstructed using the anti-k_T algorithm [37, 38], an infrared and collinear safe jet reconstruction algorithm, with a radius parameter of $\Delta R = 0.4$, seeded by three-dimensional topological calorimeter energy clusters [71]. The clustering algorithm is seeded by calorimeter cells with measured energies $E_{\text{cell}} \geq 4 \cdot \sigma_{\text{noise}}$, where σ_{noise} is the width of the noise distribution of the cell. The noise measurement includes electronic noise and pile-up effects. After a seed cell has been found adjacent[4] cells with $E_{\text{cell}} \geq 2 \cdot \sigma_{\text{noise}}$ are added to the cluster until only cells with $E_{\text{cell}} = 0$ are found.

Jets are required to have a transverse momentum $p_T > 10$ GeV and a pseudorapidity $|\eta| < 4.5$.

5.2.4 Hadronically Decaying τ Leptons

Hadronic τ decays usually result in one or three charged pions ($\pi^{\pm}$) that can be accompanied by neutral pions. Therefore these decays produce one or three charged tracks and clusters of energy deposits in both the electromagnetic and the hadronic calorimeter. The main background for this signature are jets originating from QCD multi-jet events. The main differences between this background and hadronic τ decays are

- on average jets produced in multi-jet processes are much broader compared to the more narrow pencil shaped hadronic τ decay signature and
- higher track multiplicities in the jets from QCD multi-jet processes.

Technically the reconstruction of hadronic τ decays [72] is based on calorimeter jets reconstructed with the anti-k_T algorithm. All jets with a transverse momentum $p_T > 10$ GeV which are in the pseudorapidity range of the tracking system ($|\eta| < 2.5$) are considered τ_{had} candidates and τ identification (explained in the following) is performed on them to distinguish them from the background due to jets from QCD multi-jet events.

Track Association

Tracks are associated with a τ_{had} candidate if they are within a cone of radius $\Delta R = 0.2$ centered around the τ_{had} candidate's direction (i.e. the jet's direction) and if they fulfill the following quality criteria:

- Transverse momentum $p_T > 1$ GeV,
- Number of hits in the pixel detector ≥ 2,
- Total number of the hits in the pixel and the semiconductor detectors ≥ 7,
- $|d_0| < 1.0$ mm,
- $|z_0 \sin\theta| < 1.5$ mm,

where d_0 (z_0) is the distance of closest approach of the track to the reconstructed primary vertex in the transverse (longitudinal) plane. τ_{had} candidates are classified as single or multi-prong depending on the number of associated tracks. Within the context of this analysis only one- and three-prong τ_{had} candidates are considered.

[4] Adjacency in this case includes cells in the same and the neighboring calorimeter layers.

Identification Variables

As the reconstruction of τ_{had} candidates provides only limited rejection against jets from QCD multi-jet production, additional identification criteria are needed. Furthermore, one prong τ_{had} candidates can originate from true electrons.

Variables that offer additional rejection of jets from QCD multi-jet production and true electrons that are used in this analysis are discussed in the following [72]. Figure 5.4 shows a few selected distributions of those variables for simulated $Z/\gamma^* \to \tau^+\tau^-$ and $W \to \tau\nu$ samples and di-jet samples selected in data.

- Hadronic radius (R_{had}): the transverse energy weighted width of the shower in the hadronic calorimeter associated with the τ_{had} candidate:

$$R_{\text{had}} = \frac{\sum_{i\in\{\text{Had,EM3}\}}^{\Delta R_i<0.4} E_{\text{T},i}\,\Delta R_i}{\sum_{i\in\{\text{Had,EM3}\}}^{\Delta R_i<0.4} E_{\text{T},i}}, \tag{5.1}$$

  where i runs over cells associated with the τ_{had} candidate in the hadronic calorimeter and also the third layer of the EM calorimeter. Only cells in a cone of radius $\Delta R = 0.4$ around the τ_{had} direction are considered. The calorimeter cells are associated to a τ_{had} candidate if they are part of the topological clusters the original jet is made of. The distance ΔR_i is defined between a calorimeter cell i and the τ_{had} direction. $E_{\text{T},i}$ is the cell transverse energy, calibrated at the electromagnetic energy scale.

- Calorimetric radius (R_{Cal}): the transverse energy weighted shower width in the electromagnetic and hadronic calorimeters:

$$R_{\text{Cal}} = \frac{\sum_{i\in\{\text{all}\}}^{\Delta R_i<0.4} E_{\text{T},i}\,\Delta R_i}{\sum_{i\in\{\text{all}\}}^{\Delta R_i<0.4} E_{\text{T},i}}, \tag{5.2}$$

  where i runs over cells in all layers of the EM and hadronic calorimeters in a cone of radius $\Delta R = 0.4$ around the τ_{had} direction (see Figure 5.4a). Jets from the QCD di-jet sample tend to have larger calorimeter radii than signal events.

- Track radius (R_{track}): the p_{T} weighted track width:

$$R_{\text{track}} = \frac{\sum_{i}^{\Delta R_i<0.4} p_{\text{T},i}\,\Delta R_i}{\sum_{i}^{\Delta R_i<0.4} p_{\text{T},i}}, \tag{5.3}$$

  where i runs over all tracks fulfilling the above defined criteria in a cone of radius $\Delta R = 0.4$ around the τ_{had} direction and $p_{\text{T},i}$ is the transverse momentum of track i.

- Number of isolation tracks ($N^{\text{iso}}_{\text{track}}$): the number of tracks within an isolation annulus of inner and outer radii $R_i = 0.2$ and $R_o = 0.4$, respectively, around the τ_{had} direction (see Figure 5.4b). As expected, τ_{had} candidates on average have fewer tracks then jets from QCD di-jet events.

- Leading track momentum fraction (f_{track}):

$$f_{\text{track}} = \frac{p^{\text{track}}_{\text{T},1}}{p_{\text{T},\tau_{\text{had}}}}, \tag{5.4}$$

where $p_{\mathrm{T},1}^{\mathrm{track}}$ is the transverse momentum of the highest-p_{T} (leading) track associated with the τ_{had} candidate and $p_{\mathrm{T},\tau_{\mathrm{had}}}$ is the transverse momentum of the τ_{had} candidate, calibrated at the electromagnetic energy scale.

- Core energy fraction (f_{core}): the fraction of transverse energy within a cone of radius $\Delta R = 0.1$ around the direction of the τ_{had} candidate:

$$f_{\mathrm{core}} = \frac{\sum_{i\in\{\mathrm{all}\}}^{\Delta R_i<0.1} E_{\mathrm{T},i}}{\sum_{j\in\{\mathrm{all}\}}^{\Delta R_j<0.4} E_{\mathrm{T},j}}, \tag{5.5}$$

  where i runs over all cells associated with the τ_{had} candidate within a cone of radius $\Delta R = 0.1$ around the direction of the τ_{had} candidate and j runs over all cells in a cone of radius $\Delta R = 0.4$ around the direction of the τ_{had} candidate.

- Electromagnetic fraction (f_{EM}): the fraction of transverse energy of the τ_{had} candidate deposited in the electromagnetic calorimeter:

$$f_{\mathrm{EM}} = \frac{\sum_{i\in\{\mathrm{EM\ 0-2}\}}^{\Delta R_i<0.4} E_{\mathrm{T},i}}{\sum_{j\in\{\mathrm{all}\}}^{\Delta R_j<0.4} E_{\mathrm{T},j}}, \tag{5.6}$$

  where $E_{\mathrm{T},i}$ is the transverse energy deposited in cell i, and i runs over the cells in the first three layers of the EM calorimeter, while j runs over the cells in all layers of the calorimeter.

- Cluster mass ($m_{\mathrm{eff.\ clusters}}$): the invariant mass of the constituent clusters of the τ_{had} candidate:

$$m_{\mathrm{eff.\ clusters}} = \sqrt{\left(\sum_{\mathrm{clusters}} E\right)^2 - \left(\sum_{\mathrm{clusters}} \vec{p}\right)^2}. \tag{5.7}$$

  To minimize the effect of pileup, only the first N leading E_{T} clusters (effective clusters) are used in the calculation, where N is defined as

$$N = \frac{(\sum_i E_{\mathrm{T}i})^2}{\sum_i E_{\mathrm{T}i}^2}. \tag{5.8}$$

  Here i runs over all clusters associated with the τ_{had} candidate (see Figure 5.4c). On average background events tend to have larger $m_{\mathrm{eff.\ clusters}}$ then signal events.

- Track mass (m_{tracks}): the invariant mass of the tracks in a cone of radius $\Delta R = 0.4$ around the direction of the τ_{had} candidate:

$$m_{\mathrm{tracks}} = \sqrt{\left(\sum_{\mathrm{tracks}} E\right)^2 - \left(\sum_{\mathrm{tracks}} \mathbf{p}\right)^2}. \tag{5.9}$$

- Transverse flight path significance ($S_{\mathrm{T}}^{\mathrm{flight}}$): the decay length significance of the secondary vertex reconstructed for multi-prong τ_{had} candidates in the transverse plane:

$$S_{\mathrm{T}}^{\mathrm{flight}} = \frac{L_{\mathrm{T}}^{\mathrm{flight}}}{\delta L_{\mathrm{T}}^{\mathrm{flight}}}, \tag{5.10}$$

  where $L_{\mathrm{T}}^{\mathrm{flight}}$ is the reconstructed signed decay length[5], and $\delta L_{\mathrm{T}}^{\mathrm{flight}}$ is its estimated uncertainty. Only tracks associated with the τ_{had} are used to fit the vertex (see Figure 5.4d). As jets from QCD di-jet events originate from the primary vertex, their transverse flight path significance distribution is centered around zero. Due to the proper lifetime of τ leptons, signal τ_{had} candidates tend to have larger than zero values of the transverse flight path significance.

- TRT HT fraction (f_{HT}): the ratio of high-threshold to low-threshold hits, in the Transition Radiation Tracker (TRT), for the leading p_{T} track associated with the τ_{had} candidate.

$$f_{\mathrm{HT}} = \frac{\text{High-threshold TRT hits}}{\text{Low-threshold TRT hits}}. \tag{5.11}$$

  As mentioned in the description of the TRT (see chapter 3) electrons are more likely to produce transition radiation then pions from hadronic τ decays, as they are lighter and therefore have higher Lorentz γ factors at similar energies.

- Hadronic track fraction ($E_{\mathrm{T,had}}^{\mathrm{leak}}$): the ratio of the hadronic transverse energy over the transverse momentum of the leading track:

$$E_{\mathrm{T,had}}^{\mathrm{leak}} = \frac{\sum_{i\in\{\mathrm{Had}\}}^{\Delta R_i<0.4} E_{\mathrm{T},i}}{p_{\mathrm{T},1}^{\mathrm{track}}}, \tag{5.12}$$

  where i runs over all cells in the hadronic calorimeter within a cone of radius $\Delta R = 0.4$ around the direction of the τ_{had} candidate.

- Electromagnetic track fraction ($E_{\mathrm{T,EM}}^{\mathrm{leak}}$): the ratio of the transverse energy deposited in the electromagnetic calorimeter over the transverse momentum of the leading track:

$$E_{\mathrm{T,EM}}^{\mathrm{leak}} = \frac{\sum_{i\in\{\mathrm{EM}\}}^{\Delta R_i<0.4} E_{\mathrm{T},i}}{p_{\mathrm{T},1}^{\mathrm{track}}}, \tag{5.13}$$

  where i runs over all cells in the EM calorimeter within a cone of radius $\Delta R = 0.4$ around the direction of the τ_{had} candidate.

- Maximum strip transverse energy ($E_{\mathrm{T,max}}^{\mathrm{strip}}$): the maximum transverse energy deposited in a cell in the pre-sampler layer of the electromagnetic calorimeter, which is not associated with that of the leading track.

- Ring isolation (f_{iso}):

$$f_{\mathrm{iso}} = \frac{\sum_{i}^{0.1<\Delta R<0.2} E_{\mathrm{T},i}}{\sum_{j}^{\Delta R<0.4} E_{\mathrm{T},j}}, \tag{5.14}$$

[5]The decay length is considered positive if the secondary vertex is found on the same side of the primary vertex as the calorimeter energy deposits associated to the τ_{had} candidate and negative if it is found on the other side.

where i runs over cells in the first three layers of the EM calorimeter in an annulus of inner and outer radii $R_i = 0.1$ and $R_o = 0.2$, respectively, around the τ_{had} direction and j runs over electromagnetic cells in a cone of radius $\Delta R = 0.4$ around the direction of the τ_{had} candidate.

- Leading track IP significance ($S_{\text{lead track}}$): the impact parameter ("IP") significance of the leading track of the τ_{had} candidate:

$$S_{\text{lead track}} = \frac{d_0}{\delta d_0}, \tag{5.15}$$

where d_0 is the distance of closest approach of the track to the reconstructed primary vertex in the transverse plane, and δd_0 is its estimated uncertainty.

- Maximum ΔR (ΔR_{max}): the maximal ΔR between a track associated with a τ_{had} candidate and the τ_{had} direction (see Figure 5.4e). For τ_{had} decays the tracks are much closer to the τ_{had} candidate direction then in the broader jets in QCD di-jet background events.

- Ratio of first three leading clusters energies over total energy. ($f_{3\text{ lead clusters}}$): the ratio of the energy of the first three leading clusters (highest energy first) over the total energy of all clusters associated with the τ_{had} candidate (see Figure 5.4f). Larger ratios $f_{3\text{ lead clusters}}$ are observed in the QCD di-jet background.

Identification Methods

The identification variables are used as input for three standard ATLAS identification methods, one based on 1-dimensional selection criteria ("cuts"), the others based on multivariate analysis techniques, namely boosted decision trees ("BDT") and a projective likelihood ("Likelihood") [73].

Electron vetos based on one-dimensional and multivariate (BDT) selection criteria are available.

For this analysis, a BDT is used for the τ_{had} candidate identification and the electron veto. In Table 5.1 the variables that are used for the identification and the electron veto are presented.

Identification Performance

The performance of the τ_{had} identification can be judged in terms of the signal efficiency versus the inverse background efficiency, defined as follows:

- Signal efficiency:

$$\varepsilon_{\text{sig}}^{\text{n-prong}} = \frac{\left(\begin{array}{l}\text{\# of } \tau_{\text{had}} \text{ candidates with } n \text{ reconstructed tracks, passing} \\ \text{ID, and matched to a simulated n prong decay}\end{array}\right)}{(\text{\# of simulated visible hadronic } \tau_{\text{had}} \text{ with n prongs})} \tag{5.16}$$

- Background efficiency:

$$\varepsilon_{\text{bkg}}^{\text{n-prong}} = \frac{(\text{\# of } \tau_{\text{had}} \text{ candidates with } n \text{ reconstructed tracks, passing ID})}{(\text{\# of } \tau_{\text{had}} \text{ candidates with } n \text{ reconstructed tracks})} \tag{5.17}$$

- Inverse background efficiency:

$$\frac{1}{\varepsilon_{\text{bkg}}^{\text{n-prong}}} \tag{5.18}$$

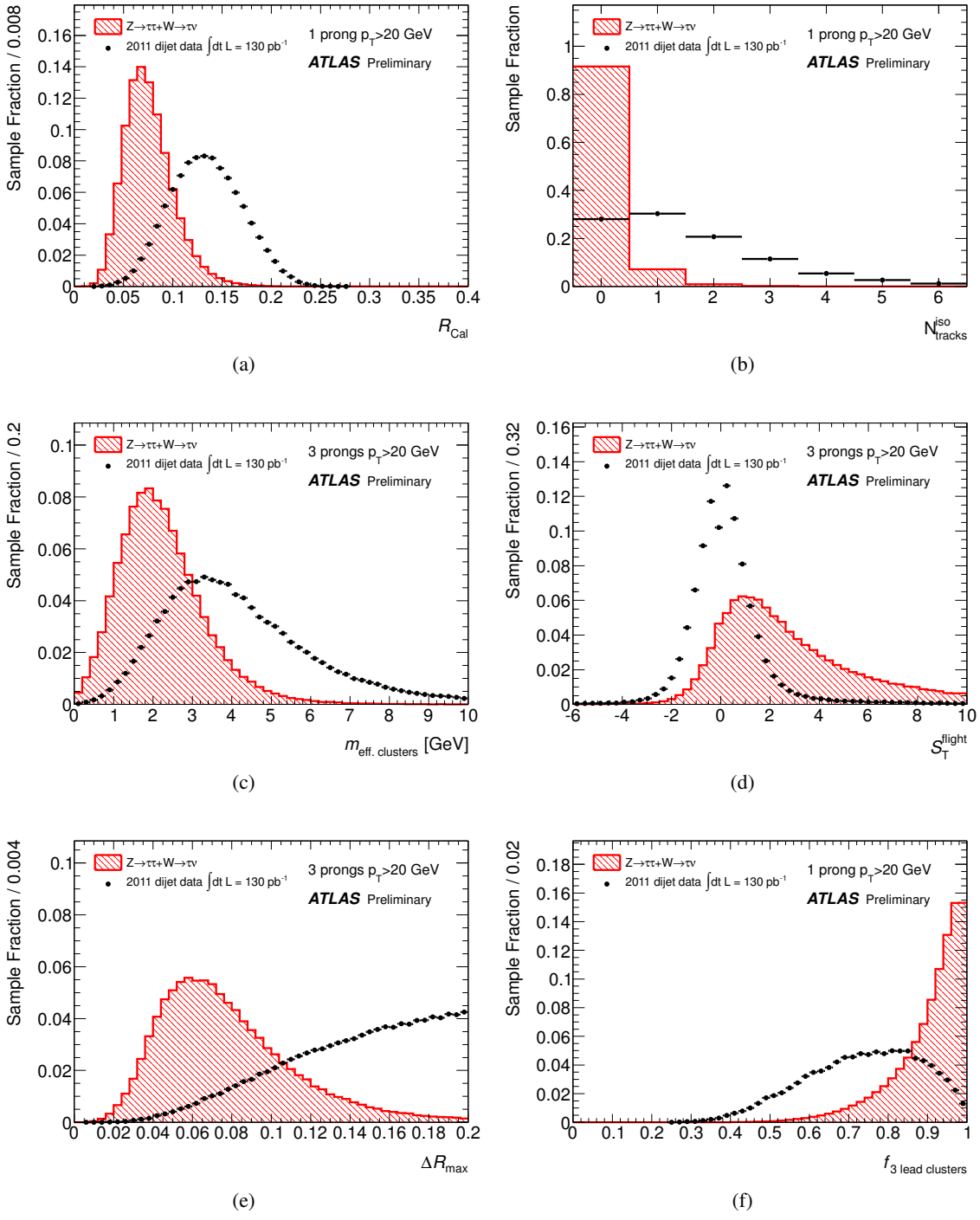

Figure 5.4: Distributions of a selection of τ_{had} identification variables for simulated $Z/\gamma^* \to \tau^+\tau^-$ and $W \to \tau\nu$ samples and a di-jet background sample selected from 2011 data. The distributions are normalized to unity [72].

	BDT τ_{had} ID		BDT e-Veto
	1-prong	multi-prong	1-prong
R_{had}			•
R_{Cal}	•	•	
R_{track}	•	•	•
$N^{\text{iso}}_{\text{track}}$	•	•	
f_{track}	•	•	•
f_{core}	•	•	•
f_{EM}			•
$m_{\text{eff. clusters}}$	•	•	
m_{tracks}		•	
$S^{\text{flight}}_{\text{T}}$		•	
f_{HT}			•
$E^{\text{leak}}_{\text{T,had}}$			•
$E^{\text{leak}}_{\text{T,EM}}$			
$E^{\text{strip}}_{\text{T,max}}$			•
f_{iso}			•
$S_{\text{lead track}}$	•	•	
ΔR_{max}		•	
$f_{\text{3 lead clusters}}$	•	•	

Table 5.1: Complete list of variables used by the boosted decision tree (BDT) for τ_{had} identification, and the BDT discriminant for electron rejection (BDT *e*-Veto). The used variables are listed separately for 1-prong and multi-prong candidates.

Where visible refers to the τ_{had} decay products that can be detected in ATLAS, i.e. everything but the neutrinos. Here, simulated visible τ_{had} candidates are taken directly from Monte Carlo generator information. Their visible four-momentum is defined as the sum of the transverse momenta of all the τ_{had} decay products, excluding neutrinos. They are required to have a transverse momentum $E_{\text{T}}^{\text{vis}} > 10$ GeV and a pseudorapidity $|\eta| < 2.5$. A τ_{had} candidate is matched to a simulated visible τ_{had} if their direction lies in a cone of radius $\Delta R = 0.2$ around the direction of the simulated visible τ_{had} candidate. Figure 5.5 shows the distribution of the inverse background efficiency as a function of the signal efficiency for the three τ_{had} identification methods in different kinematic regions and for one and three prong candidates. The BDT performance is best overall and therefore used in the following to select τ_{had} candidates. The τ_{had} identification efficiency hence results to about 45%, while the background is rejected by a factor of 70 – 130.

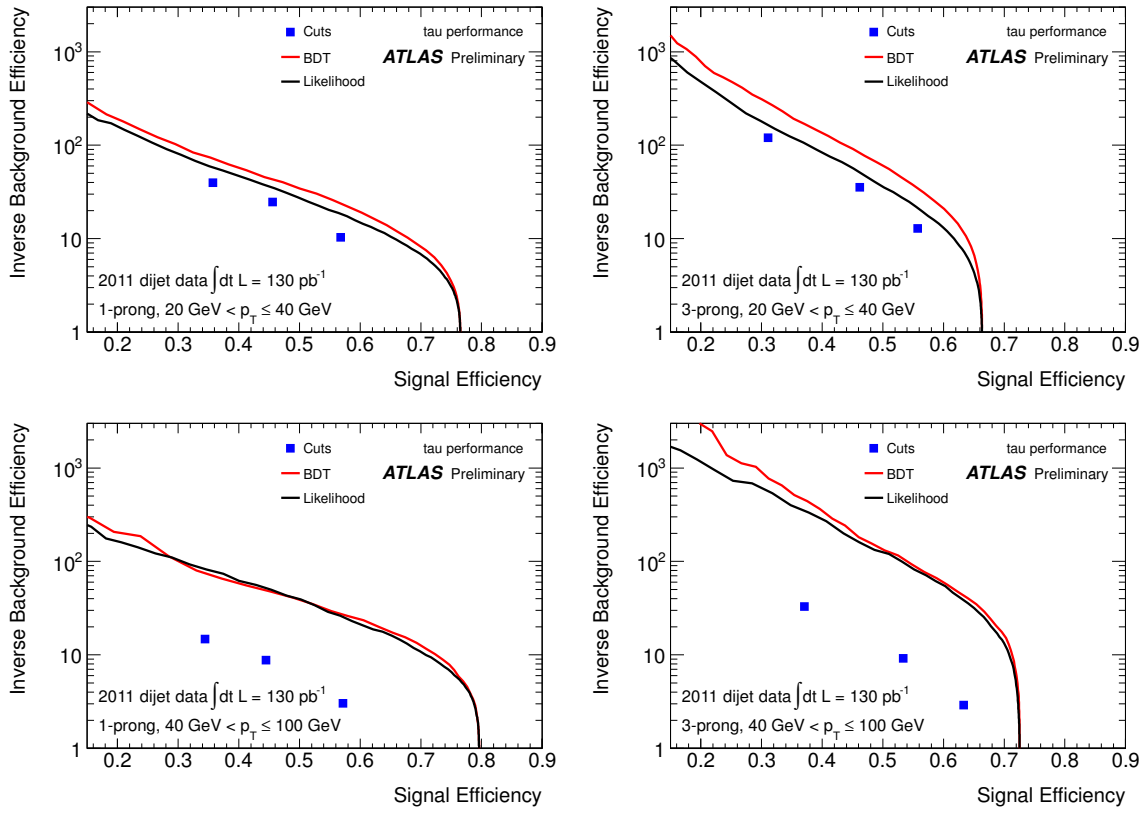

Figure 5.5: Distribution of inverse background efficiency as a function of signal efficiency for 1-prong (left) and 3-prong (right) τ_{had} candidates, in the p_{T} ranges of $20 < p_{\text{T}} \leq 40$ GeV (top) and $40 < p_{\text{T}} \leq 100$ GeV (bottom), for all τ_{had} identification discriminants [72].

The discriminant output of the BDT electron veto is shown in Figure 5.6 for simulated $Z/\gamma^* \to \tau^+\tau^-$ decays and $Z/\gamma^* \to e^+e^-$ decays selected in data. τ_{had} candidates with a discriminant value bigger than 0.51 are accepted in the following, resulting in a background rejection factor of 100 – 1000.

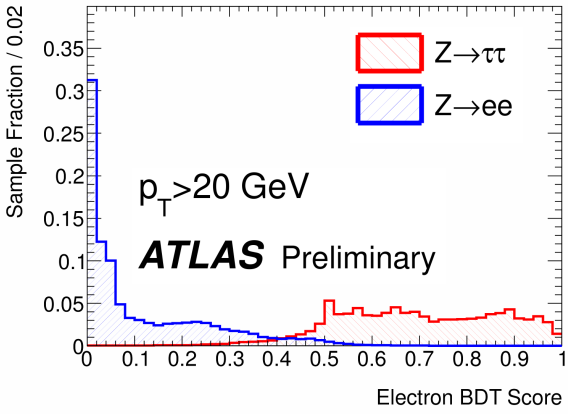

Figure 5.6: Discriminant output ("Score") of the BDT-based electron veto for simulated τ_{had} decays and electron candidates selected from data. τ_{had} candidates with a score > 0.51 are accepted [72].

5.2.5 Overlap Removal

When electron, muon, jet and τ_{had} candidates fulfilling the above selection criteria overlap geometrically (i.e. one candidate's direction is found to lie inside of a cone with radius $\Delta R = 0.2$ of another's direction) only one of them is selected. The overlap is resolved by selecting muons, electrons, τ_{had} candidates and jets in this order of priority.

5.2.6 Missing Transverse Energy $E_{\text{T}}^{\text{miss}}$

The missing transverse energy vector $\vec{E}_{\text{T}}^{\text{miss}} = (E_{\text{x}}^{\text{miss}}, E_{\text{y}}^{\text{miss}})$ is defined as the negative vectorial sum of the transverse energies deposited in calorimeter cells with pseudorapidities $|\eta| < 4.5$, using the topological clusters that are also used for jet reconstruction. It is corrected for the contribution of identified muons [74].

Assuming a perfect detector and perfect reconstruction $\vec{E}_{\text{T}}^{\text{miss}}$ is equal to the vector sum of the transverse momenta of all undetectable particles, e.g. the neutrinos from the τ decays in the signal topology.

In the following the magnitude of the vector $\vec{E}_{\text{T}}^{\text{miss}}$ will be called missing transverse energy $E_{\text{T}}^{\text{miss}}$.

5.3 Event Selection

Events passing the trigger are selected as collision events if they have a reconstructed vertex formed by at least four tracks that lies within 15 cm of the nominal interaction point along the beam axis. Standard quality criteria on jets are applied in order to suppress beam and non-collision backgrounds that are sources for badly measured missing transverse energy. Events with particles measured close to inefficient LAr-calorimeter regions are rejected.

While those selection criteria are purely driven by detector and performance issues, the following criteria are imposed to select events with signal-like topologies, e.g. featuring a τ_{had} candidate, an isolated light lepton from a leptonic decay of the second τ lepton and missing transverse energy due to the undetected neutrinos, using the object definitions described above.

- 1 lepton[6]: One electron or muon with transverse momentum $p_{\text{T}}^{e} > 25$ GeV or $p_{\text{T}}^{\mu} > 20$ GeV. In

[6]Lepton or ℓ refers to electrons and muons in the following.

Figure 5.7 the transverse momentum distribution of the selected leading electron (p_{T}^{e}) and muon (p_{T}^{μ}) before the 1 lepton selection is shown for the simulated background and a signal sample. As no simulated QCD multi-jet event samples with sufficiently high amounts of events generated exist, this background is not included. The histograms representing the backgrounds are stacked on top of each other, the shape of the signal sample distribution is indicated by the red dashed line.

- Di-lepton veto: Events with more than one light lepton are rejected to suppress events from $Z/\gamma^{*} \rightarrow e^{+}e^{-}/\mu^{+}\mu^{-}$, $t\bar{t}$ and single top processes. To provide a harsher suppression of these backgrounds the isolation requirements are dropped from the muon selection and a looser identification for electrons is applied for the veto.

- 1 τ_{had} candidate: Exactly one identified τ_{had} candidate with a transverse momentum of $p_{\mathrm{T},\tau_{\mathrm{had}}} > 20$ GeV is required. To illustrate the performance of the τ identification in this analysis the distribution of $p_{\mathrm{T},\tau_{\mathrm{had}}}$ and the discriminator output of the BDT τ_{had} identification method for data, a signal sample ($m_A = 120$ GeV, $\tan\beta = 20$) and two background samples are presented in Figure 5.8. For the simulated samples the reconstructed τ_{had} candidates are matched to hadronically decaying, generator level τ leptons that lie in a cone of radius $\Delta R = 0.2$ around the reconstructed candidate's direction. If a match is found the τ_{had} candidate is categorized as "true", otherwise as "fake". As expected, the signal and the $Z/\gamma^{*} \rightarrow \tau^{+}\tau^{-}$ samples have a large number of true τ_{had} candidates that also have high BDT scores and are therefore selected in the analysis.

- Charge correlation: The charges of the lepton q_{ℓ} and the τ_{had} candidate $q_{\tau_{\mathrm{had}}}$ are required to have opposite signs: $q_{\ell} \times q_{\tau_{\mathrm{had}}} = -1$ as they are supposed to be the decay products of a neutral Higgs boson. In Figure 5.9 the distribution of the product of the charges of the e/μ and the τ_{had} candidates after the 1 τ_{had} selection step are shown for the simulated background samples and a signal sample.

  In the following, events passing this criterion are referred to as opposite-sign ("OS") events, while events not passing are called same-sign ("SS") events.

- $E_{\mathrm{T}}^{\mathrm{miss}}$: The missing transverse energy $E_{\mathrm{T}}^{\mathrm{miss}}$ is required to be bigger than 20 GeV to reject events from QCD multi-jet and $Z/\gamma^{*} \rightarrow e^{+}e^{-}/\mu^{+}\mu^{-}$ processes. The $E_{\mathrm{T}}^{\mathrm{miss}}$ distribution after the charge correlation selection is applied is shown in Figure 5.10.

- Transverse mass: The transverse mass of the lepton-$E_{\mathrm{T}}^{\mathrm{miss}}$system is defined as:

$$m_{\mathrm{T}} = \sqrt{2 p_{\mathrm{T}}^{\ell} E_{\mathrm{T}}^{\mathrm{miss}} (1 - \cos\Delta\phi)}, \tag{5.19}$$

  where p_{T}^{ℓ} denotes the transverse momentum of the lepton and $\Delta\phi$ is the angle between the lepton and $\vec{E}_{\mathrm{T}}^{\mathrm{miss}}$ in the plane perpendicular to the beam direction. The distribution of m_{T} for background samples from simulation and a signal sample are shown in Figure 5.11. To reduce contributions from backgrounds with real W bosons such as W + jets, $t\bar{t}$ and single-top processes, events are required to have $m_{\mathrm{T}} \leq 30$ GeV. In addition, the high-m_{T} region is dominated by the W + jets background and can be used to study this background.

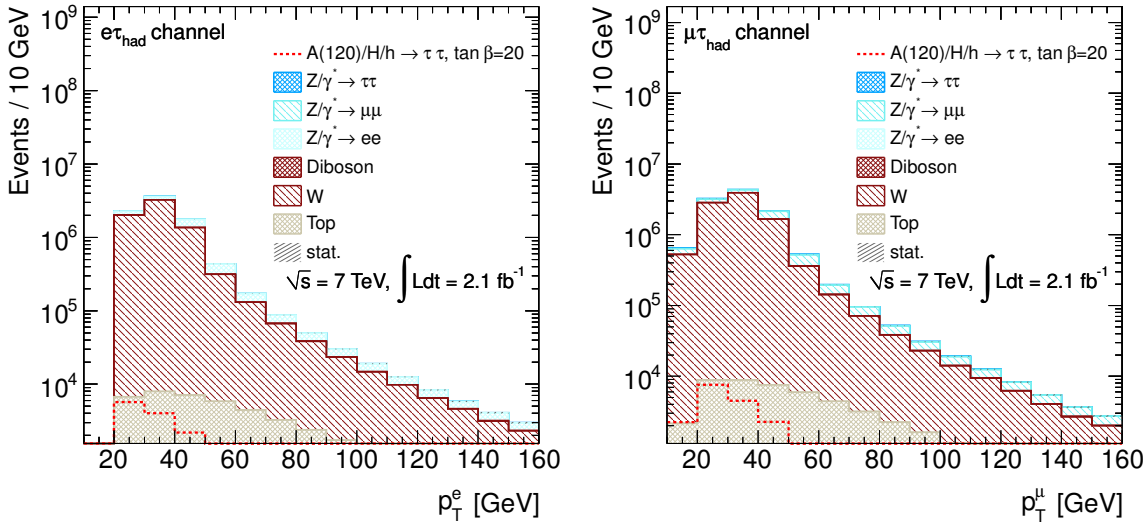

Figure 5.7: Simulated distribution of the transverse momentum of the selected leading electron, p_{T}^{e}, (left) and muon, p_{T}^{μ}, (right) before the 1 lepton selection. Shown are a signal sample (m_A = 120 GeV, $\tan\beta$ = 20, with the yield increased by a factor of 5 for better visibility) indicated by the dashed red line and background samples from simulation (with the samples stacked on top of each other) and their statistical uncertainty shown as a hatched error band. No simulated QCD multi-jet sample events are included.

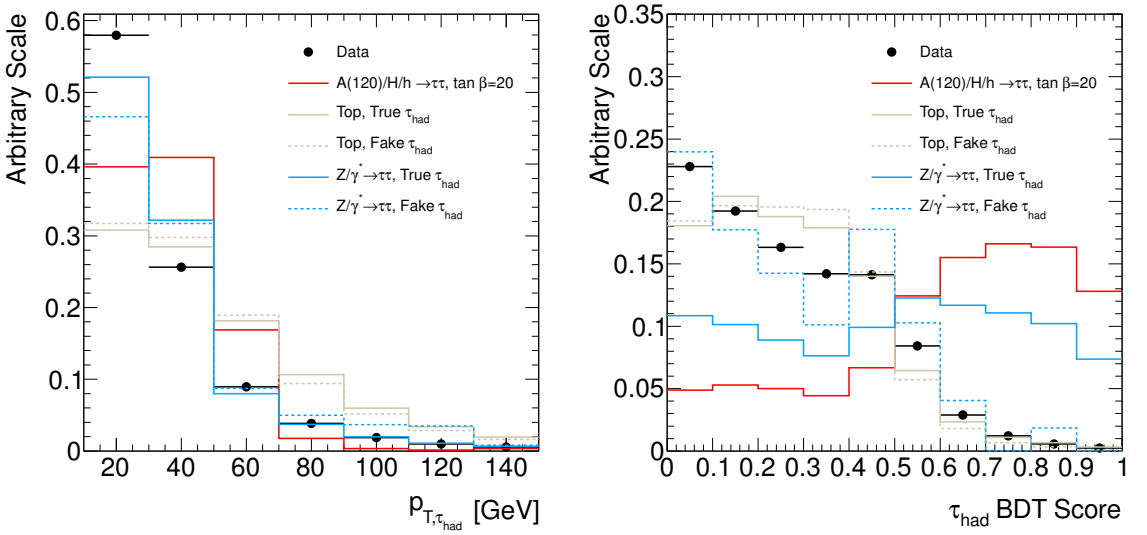

Figure 5.8: Distribution of the τ_{had} transverse momentum and the score of the BDT identification of τ_{had} candidates before the 1 τ_{had} selection for the data, a hypothetical signal (m_A = 120 GeV, $\tan\beta$ = 20) and background samples from simulation. The distributions are given for true and fake τ_{had} candidates. High/low BDT score indicates signal/background like τ_{had} candidates. All distributions are normalized to unity to compare the shapes of the distributions.

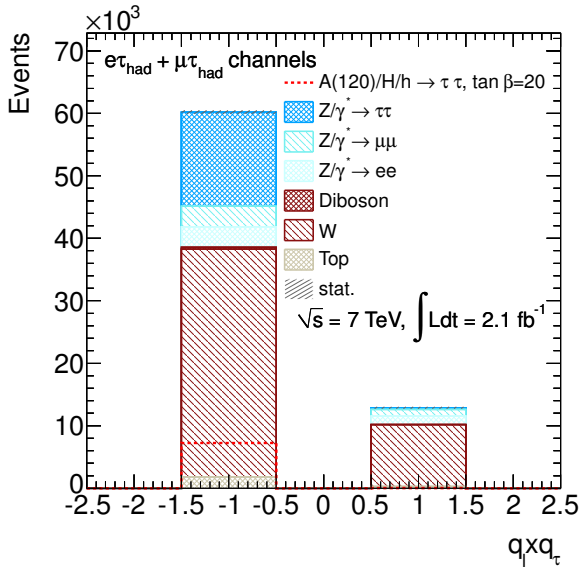

Figure 5.9: Simulated distribution of the product of the charges of the e/μ and the τ_{had} candidates after the 1 τ_{had} selection step. Shown are a signal sample ($m_A = 120$ GeV, $\tan\beta = 20$, with the yield increased by a factor of 5 for better visibility) indicated by the dashed red line and background samples from simulation (with the samples stacked on top of each other) and their statistical uncertainty. No simulated QCD multi-jet sample events are included.

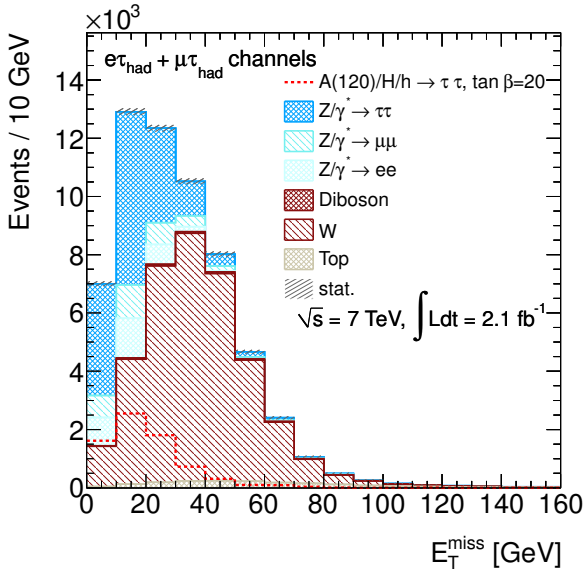

Figure 5.10: Simulated distribution of the missing transverse energy $E_{\text{T}}^{\text{miss}}$ after the charge correlation selection. Shown are a signal sample ($m_A = 120$ GeV, $\tan\beta = 20$, with the yield increased by a factor of 5 for better visibility) indicated by the dashed red line and background samples from simulation (with the samples stacked on top of each other) and their statistical uncertainty. No simulated QCD multi-jet sample events are included.

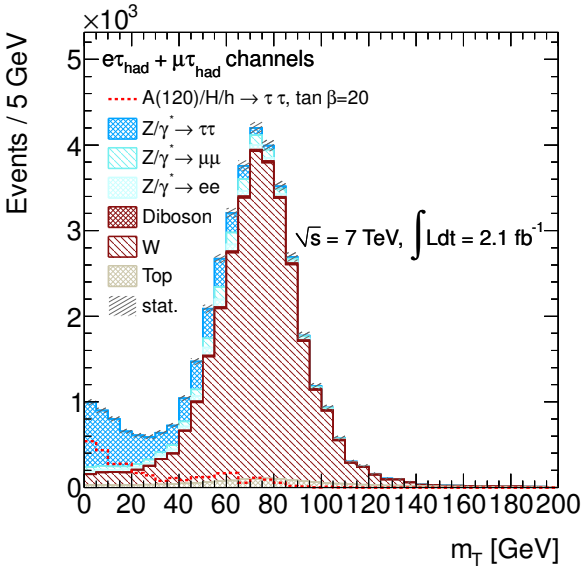

Figure 5.11: Simulated distribution of the transverse mass of the lepton-$E_{\mathrm{T}}^{\mathrm{miss}}$ system, m_{T}, after the $E_{\mathrm{T}}^{\mathrm{miss}}$ selection criterion. Shown are a signal sample ($m_A = 120\,\mathrm{GeV}$, $\tan\beta = 20$, with the yield increased by a factor of 5 for better visibility) indicated by the dashed red line and background samples from simulation (with the samples stacked on top of each other) and their statistical uncertainty. No simulated QCD multi-jet sample events are included.

5.4 Results of the Selection

In Tables 5.2 and 5.3 the effect of the selection on the data, a hypothetical signal ($m_A = 120\,\mathrm{GeV}$, $\tan\beta = 20$) and background samples from simulation is shown for the $e\tau_{\mathrm{had}}$ and the $\mu\tau_{\mathrm{had}}$ channels. In addition, the efficiency of each criterion is given. In data 4239 events ($e\tau_{\mathrm{had}}$: 1456, $\mu\tau_{\mathrm{had}}$: 2783) are selected. The signal efficiency is $\approx 0.7\%$ for $m_A = 120\,\mathrm{GeV}$, $\tan\beta = 20$.

The data are compared with the simulated background samples at different steps of the selection. In Figure 5.12 the distribution of the transverse mass m_{T} is shown for the data, an example signal sample ($m_A = 120\,\mathrm{GeV}$, $\tan\beta = 20$) and the simulated background samples before the m_{T} selection criterion is applied. The histograms for the simulated samples are stacked on top of each other. The simulation does not agree with the data and the distribution suggests that the normalization of the W + jets sample needs to be corrected. Furthermore no estimate for the background from QCD multi-jet processes is included.

Additional examples with the full selection applied are shown in Figure 5.13, namely the distribution of transverse momentum $p_{\mathrm{T},\tau_{\mathrm{had}}}$ of the τ_{had} candidate and the missing transverse energy $E_{\mathrm{T}}^{\mathrm{miss}}$. The simulation results do not agree with the data at this selection step either. In Chapter 6 methods to improve the agreement by estimating the $Z/\gamma^* \to \tau^+\tau^-$, W + jets and QCD multi-jet background with the help of data control regions will be introduced. These two distributions are going to be shown repeatedly to illustrate the effect of the data based background estimation methods presented in the following Chapter 6.

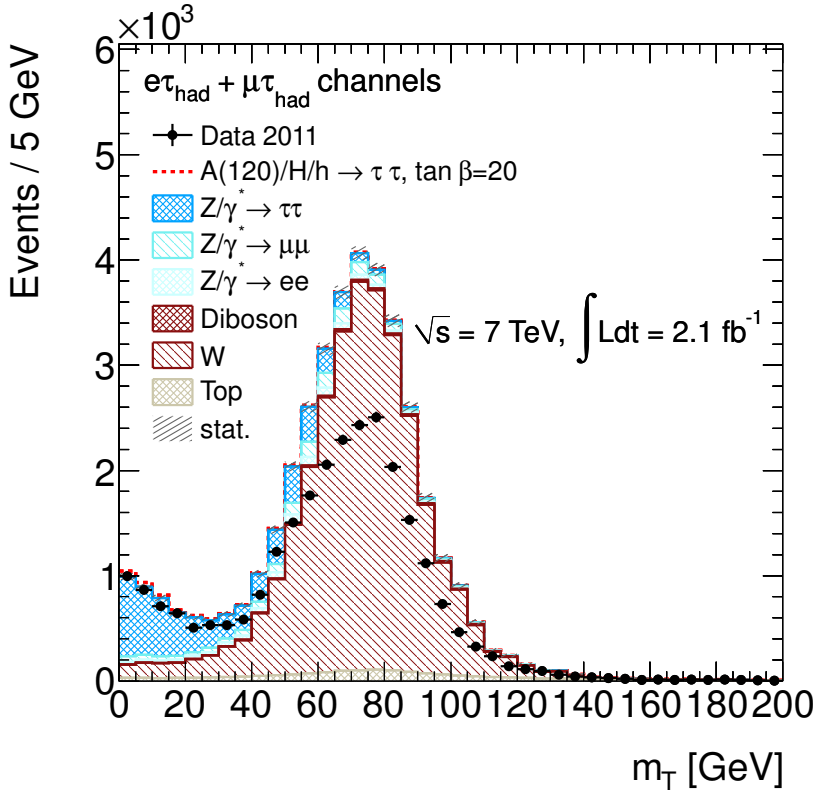

Figure 5.12: Distribution of the transverse mass m_{T} before the m_{T} selection criterion is applied. Shown are the data, a signal sample ($m_A = 120\,\mathrm{GeV}$, $\tan\beta = 20$) on top of background samples from simulation (with the background samples stacked on top of each other) and their statistical uncertainty shown as a hatched error band. No simulated QCD multi-jet events are included.

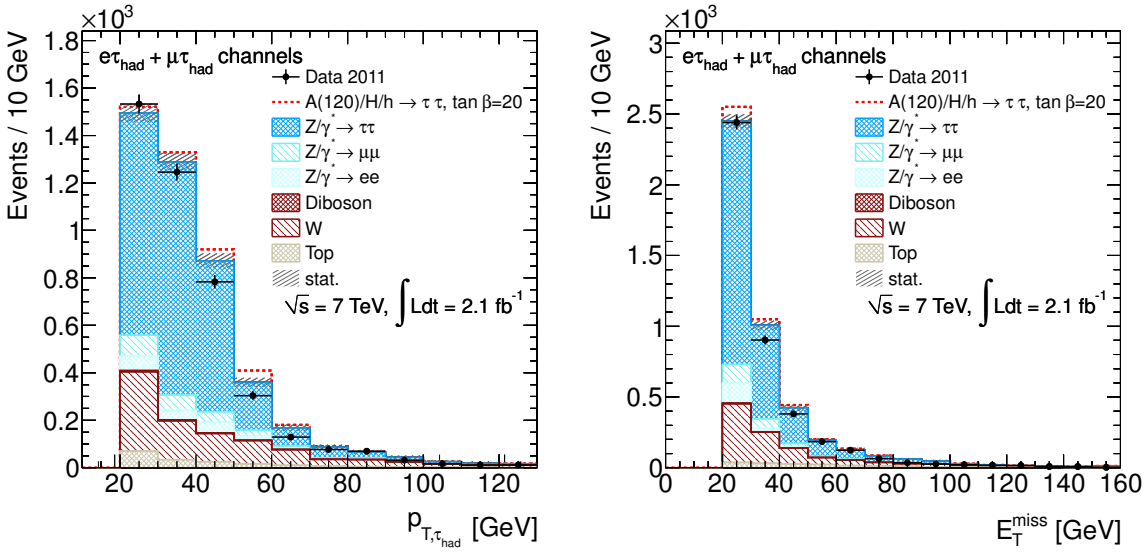

Figure 5.13: Distribution of the transverse momentum of the τ_{had} candidate $p_{\mathrm{T},\tau_{\mathrm{had}}}$ (left) and the missing transverse energy $E_{\mathrm{T}}^{\mathrm{miss}}$ (right) with the full selection applied. Shown are the data, a signal sample ($m_A = 120\,\mathrm{GeV}$, $\tan\beta = 20$) on top of background samples from simulation (with the background samples stacked on top of each other) and their statistical uncertainty. No simulated QCD multi-jet events are included.

5.5 Mass Reconstruction

After selecting signal candidate events the di-τ mass is the most promising distribution to find a Higgs boson signal in. Different mass reconstruction methods are studied. The simplest one is the so-called visible di-τ mass, $m_{\tau\tau}^{\text{visible}}$, defined as the invariant mass of the τ_{had} and lepton system. It can be expanded to the effective mass, $m_{\tau\tau}^{\text{effective}}$, by calculating the invariant mass of the τ_{had}, lepton and $E_{\text{T}}^{\text{miss}}$ according to

$$m_{\tau\tau}^{\text{effective}} = \sqrt{(p_{\tau_{\text{had}}} + p_\ell + p_{\text{T}}^{\text{miss}})^2}, \tag{5.20}$$

where $p_{\tau_{\text{had}}}$ and p_ℓ denote the four-vectors of the τ_{had} and the lepton candidates, respectively, and the missing momentum four-vector is defined as $p_{\text{T}}^{\text{miss}} = (E_{\text{T}}^{\text{miss}}, E_{\text{x}}^{\text{miss}}, E_{\text{y}}^{\text{miss}}, 0)$.

A clear disadvantage of these methods is that they cannot reproduce the mass of the di-τ resonance, as they do not properly account for the neutrinos in the τ decays. Hence the masses estimated with them will be lower than the true mass of the resonance.

An accurate mass reconstruction is challenging, as it needs to estimate the contribution of the neutrinos. Furthermore, more advanced mass reconstruction techniques do not necessarily find a solution for all events and hence have a lower efficiency, defined as the ratio of the number of events where a solution is found divided by the number of all events passed as input to the algorithm.

The collinear approximation [75] assumes strict collinearity of the visible and invisible τ decay products and therefore suffers from not being able to describe back-to-back configurations and hence reduced mass reconstruction efficiency.

The so-called "Missing Mass Calculator (MMC)" a novel technique, introduced in [76], does not assume a strict collinearity and therefore has a higher efficiency.

For each event the MMC solves a system of four equations:

$$\begin{aligned}
E_{\text{x}}^{\text{miss}} &= p_{(\nu_\ell\bar{\nu}_\tau)} \sin\theta_{(\nu_\ell\bar{\nu}_\tau)} \cos\phi_{(\nu_\ell\bar{\nu}_\tau)} + p_{\nu_\tau} \sin\theta_{\nu_\tau} \cos\phi_{\nu_\tau}, && (5.21)\\
E_{\text{y}}^{\text{miss}} &= p_{(\nu_\ell\bar{\nu}_\tau)} \sin\theta_{(\nu_\ell\bar{\nu}_\tau)} \sin\phi_{(\nu_\ell\bar{\nu}_\tau)} + p_{\nu_\tau} \sin\theta_{\nu_\tau} \sin\phi_{\nu_\tau}, && (5.22)\\
m_\tau^2 &= m_{(\nu_\ell\bar{\nu}_\tau)}^2 + m_\ell^2 + 2\sqrt{p_\ell^2 + m_\ell^2}\sqrt{p_{(\nu_\ell\bar{\nu}_\tau)}^2 + m_{(\nu_\ell\bar{\nu}_\tau)}^2},\\
&\quad -2p_\ell p_{(\nu_\ell\bar{\nu}_\tau)} \cos\theta_{\ell,(\nu_\ell\bar{\nu}_\tau)}, && (5.23)\\
m_\tau^2 &= m_{\tau_{\text{had}}}^2 + 2\sqrt{p_{\tau_{\text{had}}}^2 + m_{\tau_{\text{had}}}^2}\cdot p_{\nu_\tau},\\
&\quad -2p_{\tau_{\text{had}}} p_{\nu_\tau} \cos\theta_{\tau_{\text{had}},\nu_\tau} && (5.24)
\end{aligned}$$

where the known quantities are

- the x- and y- components of the $p_{\text{T}}^{\text{miss}}$ vector, $E_{\text{x}}^{\text{miss}}$ and $E_{\text{y}}^{\text{miss}}$,
- the invariant mass of the τ lepton, $m_\tau = 1.777$ GeV,
- the "visible" components of the two τ decays:
  - the momentum, the invariant mass, the azimuthal and the polar angle of the lepton from one τ decay, p_ℓ, m_ℓ, θ_ℓ and ϕ_ℓ,
  - the momentum, the invariant mass, the azimuthal and the polar angle of the τ_{had} decay products from the other τ decay, $p_{\tau_{\text{had}}}$, $m_{\tau_{\text{had}}}$, $\theta_{\tau_{\text{had}}}$ and $\phi_{\tau_{\text{had}}}$.

The unknown quantities are

- the "invisible" products of the two τ decays:
  - the momentum, the invariant mass, the polar and the azimuthal angle of the combined two neutrino system from the leptonic τ decay, $p_{(\nu_\ell\bar{\nu}_\tau)}$, $m_{(\nu_\ell\bar{\nu}_\tau)}$, $\theta_{(\nu_\ell\bar{\nu}_\tau)}$, $\phi_{(\nu_\ell\bar{\nu}_\tau)}$,
  - the momentum, the polar and the azimuthal angle of the neutrino from the τ_{had} decay, p_{ν_τ}, θ_{ν_τ}, ϕ_{ν_τ}, and
- the difference between the polar angles of the visible and the invisible parts of the two τ decays, $\theta_{\ell,(\nu_\ell\bar{\nu}_\tau)}$, $\theta_{\tau_{\text{had}},\nu_\tau}$.

The number of unknowns exceeds the number of constraints and thus the system can only be solved numerically. A grid of points in the $(\Delta\phi_1, \Delta\phi_2)$ parameter space, with $\Delta\phi_1 = \phi_\ell - \phi_{(\nu_\ell\bar{\nu}_\tau)}$ and $\Delta\phi_2 = \phi_{\tau_{\text{had}}} - \phi_{\nu_\tau}$ is scanned. The system is solved for each point and the di-τ mass $m_{\tau\tau}$ and the 3-dimensional angle between the directions of the visible and the invisible products of the τ decays, $\Delta\theta_{3\text{D}}$ are calculated. A probability density function for $\Delta\theta_{3\text{D}}$ is used to weight each grid point. The position of the maximum of the resulting $m_{\tau\tau}$ distribution is used as the mass estimate for a given event and called MMC $m_{\tau\tau}$ in the following. The probability density function is estimated with simulated $Z/\gamma^* \to \tau^+\tau^-$ events for leptonic, 1- and 3-prong τ decays separately and a comparison of the function to the distribution of $\Delta\theta_{3\text{D}}$ in simulated $Z/\gamma^* \to \tau^+\tau^-$events is shown in Figure 5.14. As a cross-check, similar probability density functions are obtained from a simulated sample of $H(120\text{ GeV}) \to \tau\tau$ events and the $\Delta\theta_{3\text{D}}$ distributions are found to be compatible [7]. To account for effects of finite $E_{\text{T}}^{\text{miss}}$ resolution, two additional scans over $E_{\text{x}}^{\text{miss}}$ and $E_{\text{y}}^{\text{miss}}$ are performed according to the measured $E_{\text{T}}^{\text{miss}}$ resolution of $\sigma(E_{\text{T}}^{\text{miss}}) = A_0\sqrt{\sum p_{\text{T}}}$, with $A_0 = 0.50 \pm 0.05$ [77].

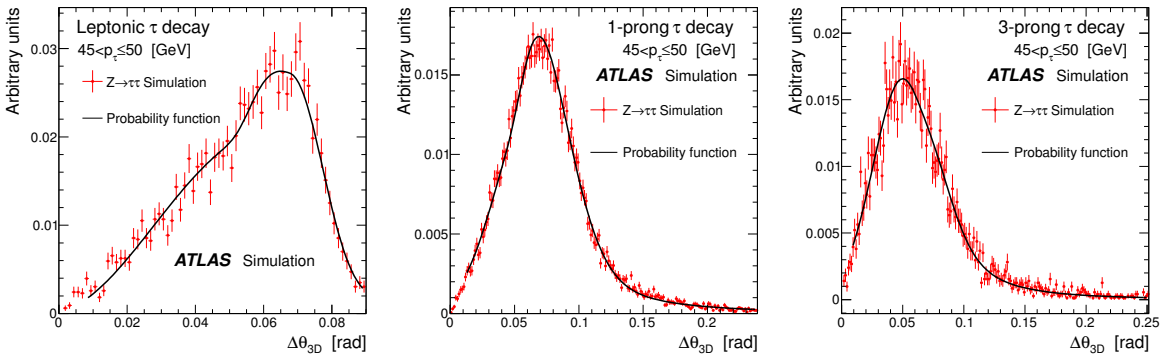

Figure 5.14: Angular distance distributions between neutrinos and visible decay products for τ leptons with generated momentum $45 < p \leq 50$ GeV obtained from simulated $Z \to \tau\tau$ events. The three distributions correspond to the three dominant types of τ decays [7].

In Table 5.4 the MMC efficiency is shown. It is defined as the number of events the MMC finds a solution for divided by the number of selected events that served as input to the algorithm, for simulated $Z/\gamma^* \to \tau^+\tau^-$ and signal samples. The efficiency for non-Z-boson backgrounds is smaller (see Tables 5.2 and 5.3 for efficiencies on all samples). For the Z-boson backgrounds and signal samples with masses up to $M_H = 150$ GeV, the MMC mass resolution is about 17% and below 23% for the higher masses considered.

The MMC mass for several signal samples is shown in Figure 5.15 after the full selection.

After reconstructing the $m_{\tau\tau}$ mass with the MMC, 4065 data events ($e\tau_{\text{had}}$: 1410, $\mu\tau_{\text{had}}$: 2655) are retained. The distribution of the transverse momentum of the τ_{had} candidate $p_{\text{T},\tau_{\text{had}}}$ and the missing

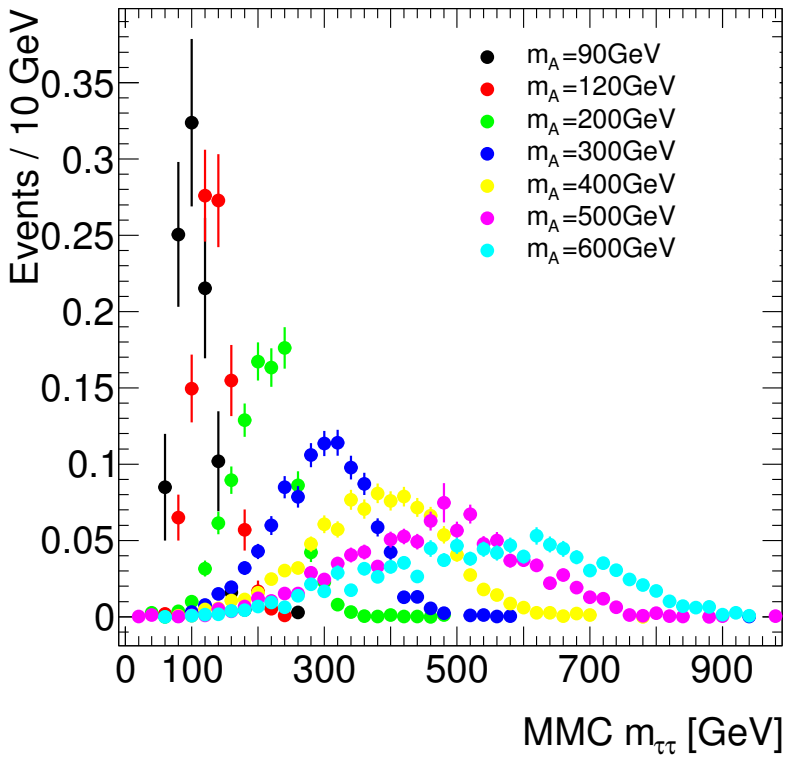

Figure 5.15: MMC mass distribution for several signal samples (Sherpa $b\bar{b}A$) with masses m_A from 90 – 600 GeV. The distributions are normalized to unity.

transverse energy $E_{\mathrm{T}}^{\mathrm{miss}}$ are shown in Figure 5.16 for the data, an example signal sample and the simulated background samples with the full selection and the MMC mass reconstruction applied. The agreement of the simulation with the data is similar to the one found before the MMC $m_{\tau\tau}$ reconstruction (see Figure 5.12).

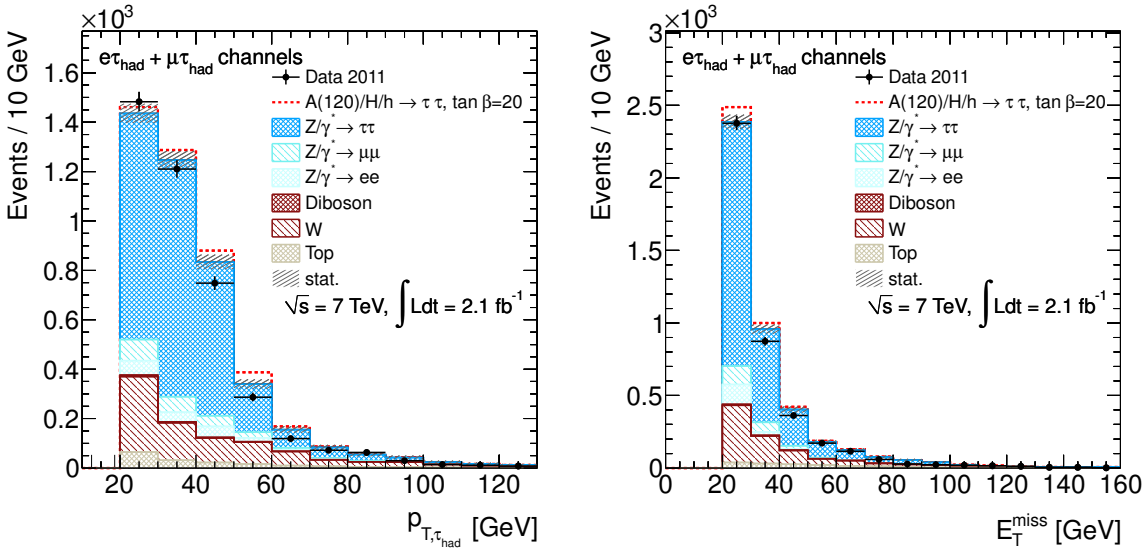

Figure 5.16: Distribution of the transverse momentum of the τ_{had} candidate $p_{\mathrm{T},\tau_{\mathrm{had}}}$ (left) and the missing transverse energy $E_{\mathrm{T}}^{\mathrm{miss}}$ (right) after the full selection and the MMC $m_{\tau\tau}$ mass reconstruction. Shown are the data, a signal sample ($m_A = 120$ GeV, $\tan\beta = 20$) on top of background samples from simulation (with the background samples stacked on top of each other) and their statistical uncertainty. No simulated QCD multi-jet events are included.

	Data		Signal		Diboson		W + jets		$Z/\gamma^* \to e^+e^-$		$Z/\gamma^* \to \tau^+\tau^-$		Top	
	Yield	Eff.	Yield	Eff.	Yield	Eff.	Yield	Eff.	Yield	Eff.	Yield	Eff.	Yield	Eff.
Processed	2.7×10^8	-	2.6×10^4	-	2.9×10^4	-	7.0×10^7	-	1.0×10^7	-	1.0×10^7	-	5.3×10^5	-
Generator Weight	-	-	2.6×10^4	100%	2.1×10^4	72%	7.0×10^7	100%	1.0×10^7	100%	1.0×10^7	100%	4.2×10^5	80%
Trigger	1.1×10^8	43%	3.6×10^3	14%	7.7×10^3	36%	1.2×10^7	17%	1.6×10^6	16%	1.0×10^5	1%	7.3×10^4	17%
Cleaning	1.1×10^8	95%	3.4×10^3	95%	7.3×10^3	95%	1.1×10^7	95%	1.6×10^6	95%	9.7×10^4	95%	6.6×10^4	91%
1 Electron	9.5×10^6	9%	1.8×10^3	52%	5.1×10^3	70%	6.9×10^6	61%	1.1×10^6	72%	3.9×10^4	40%	4.2×10^4	63%
Di-lepton Veto	8.9×10^6	94%	1.7×10^3	99%	3.1×10^3	60%	6.9×10^6	100%	5.9×10^5	53%	3.4×10^4	87%	3.2×10^4	77%
1 τ_{had}	2.8×10^4	0%	509	29%	178	6%	2.1×10^4	0.3%	4582	1%	5221	15%	984	3%
$q_\ell \times q_{\tau_{\text{had}}} = -1$	2.1×10^4	73%	496	99%	150	85%	1.7×10^4	78%	3018	71%	5115	98%	851	86%
$E_{\text{T}}^{\text{miss}} > 20$ GeV	1.2×10^4	55%	211	43%	122	82%	1.4×10^4	84%	838	28%	1850	36%	766	90%
$m_{\text{T}} < 30$ GeV	1456	13%	125	59%	8	7%	440	3%	170	20%	939	51%	84	11%
Mass reco. (MMC)	1410	97%	123	98%	8	93%	406	92%	167	98%	918	98%	78	93%

Table 5.2: Overview of the event yields for the $e\tau_{\text{had}}$ **channel** after the application of each selection criterion and of the efficiency (Eff.) of each criterion for the data, a hypothetical signal of $m_A = 120$ GeV and $\tan\beta = 20$ and for all background samples from simulation. For data the item "Trigger" also includes the requirement that the detector was fully operational and data taking was successful for all sub-systems, which was the case in $\approx 86\%$ of the events.

	Data		Signal		Diboson		W + jets		$Z/\gamma^* \to \mu^+\mu^-$		$Z/\gamma^* \to \tau^+\tau^-$		Top	
	Yield	Eff.	Yield	Eff.	Yield	Eff.	Yield	Eff.	Yield	Eff.	Yield	Eff.	Yield	Eff.
Processed	2.6×10^8	-	2.6×10^4	-	2.9×10^4	-	5.4×10^7	-	1.0×10^7	-	8.3×10^6	-	5.3×10^5	-
Generator Weight	-	-	2.6×10^4	100%	2.1×10^4	72%	5.4×10^7	100%	1.0×10^7	100%	8.3×10^6	100%	4.2×10^5	80%
Trigger	8.8×10^7	34%	3.7×10^3	14%	7.0×10^3	33%	9.2×10^6	17%	1.7×10^6	17%	9.9×10^4	1%	7.6×10^4	18%
Cleaning	8.3×10^7	95%	3.6×10^3	97%	6.7×10^3	96%	8.9×10^6	96%	1.7×10^6	97%	9.6×10^4	96%	7.0×10^4	92%
1 Muon	1.2×10^7	15%	2.7×10^3	76%	6.1×10^3	91%	7.6×10^6	86%	1.5×10^6	90%	6.7×10^4	70%	4.8×10^4	69%
Di-lepton Veto	1.1×10^7	92%	2.7×10^3	98%	3.3×10^3	55%	7.6×10^6	100%	5.4×10^5	37%	6.0×10^4	89%	3.7×10^4	76%
1 τ_{had}	3.4×10^4	0%	753	28%	197	6%	2.3×10^4	0.3%	4352	1%	8418	14%	1136	3%
$q_\ell \times q_{\tau_{\text{had}}} = -1$	2.7×10^4	80%	750	100%	180	88%	1.8×10^4	79%	3299	76%	8284	98%	970	86%
$E_{\text{T}}^{\text{miss}} > 20$ GeV	1.6×10^4	57%	362	48%	150	83%	1.5×10^4	85%	1405	43%	2858	35%	880	91%
$m_{\text{T}} < 30$ GeV	2783	18%	223	62%	13	9%	474	3%	242	17%	1683	59%	99	11%
Mass reco. (MMC.)	2655	95%	219	98%	12	90%	404	85%	233	96%	1636	97%	89	90%

Table 5.3: Overview of the event yields for the $\mu\tau_{\text{had}}$ **channel** after the application of each selection criterion and of the efficiency (Eff.) of each criterion for the data, a hypothetical signal of $m_A = 120$ GeV and $\tan\beta = 20$ and for all background samples from simulation. For data the item "Trigger" also includes the requirement that the detector was fully operational and data taking was successful for all sub-systems, which was the case in $\approx 83\%$ of the events.

Mass[GeV]	92	120	150	200	250	300	400	600
MMC Eff.	98%	98%	98%	97%	96%	92%	87%	81%

Table 5.4: MMC efficiency for the $Z/\gamma^* \rightarrow \tau^+\tau^-$background and for signal samples with mass $M_H = 120$ GeV, 150 GeV, 200 GeV, 250 GeV, 300 GeV, 400 GeV and with 600 GeV.

Chapter 6

Background Estimation

As understanding the normalization and the shape of the MMC $m_{\tau\tau}$ distribution for the main background components is crucial for discovering or excluding a potential Higgs boson signal, data control samples are used as much as possible. In the following, methods to estimate the $Z/\gamma^* \to \tau^+\tau^-$, the W + jets and the QCD multi-jet backgrounds from data are presented.

6.1 $Z \to \tau^+\tau^-$ Embedding

The shape of the MMC $m_{\tau\tau}$ distribution from the irreducible $Z/\gamma^* \to \tau^+\tau^-$ background is estimated with a data-driven method based on a so-called embedding technique [7]. This method uses a $Z/\gamma^* \to \mu^+\mu^-$ sample selected from data by requiring two muons with transverse momenta $p_{\mathrm{T}}^{\mu} > 20$ GeV, no isolation criteria applied, and a di-muon mass $m_{\mu\mu} > 40$ GeV. The muons in these events are replaced by simulated τ leptons according to the following procedure:

- The kinematics of the di-μ system are used as an estimate for the Z boson kinematics.
- The muon tracks and associated calorimeter cells (within a cone of radius $\Delta R = 0.1$ around the muon direction) are removed from the event.
- An event fragment is generated that contains only a $Z/\gamma^* \to \tau^+\tau^-$ decay with the same kinematics as the $Z/\gamma^* \to \mu^+\mu^-$ decay. The τ lepton decays are generated with TAUOLA [65].
- The original data event after the removal of the muons and the simulated event fragment are combined and the full reconstruction is performed on the combined event.

Thus only the τ decays and the corresponding detector response are taken from simulation, while the Z decay kinematics and all other properties of the event, including underlying event, pile-up, etc., are taken directly from data. Figure 6.1 shows a shape comparison for $Z/\gamma^* \to \tau^+\tau^-$ from simulation, generated with ALPGEN, and $Z/\gamma^* \to \tau^+\tau^-$ from embedding samples for the MMC $m_{\tau\tau}$ distribution. The comparison is shown for two steps of the selection: Without the $E_{\mathrm{T}}^{\mathrm{miss}}$ and m_{T} selection criteria applied and after the full event selection. The distributions agree within the statistical uncertainties.

As no trigger response has been implemented in the embedding samples the normalization is taken from simulation, by normalizing the yield of the embedding samples to the prediction after the charge correlation criterion is applied. In the following, embedding samples are used instead of simulated $Z/\gamma^* \to \tau^+\tau^-$ samples unless stated otherwise. For comparison with the overall background prediction using only simulated background samples shown in Figure 5.16, in Figure 6.2 the distribution of the transverse momentum of the τ_{had} candidate $p_{\mathrm{T},\tau_{\mathrm{had}}}$ and the missing transverse energy $E_{\mathrm{T}}^{\mathrm{miss}}$ are presented for the data, the simulated background sample and the $Z/\gamma^* \to \tau^+\tau^-$ embedding sample. As expected the differences are small, as the simulated and the embedded $Z/\gamma^* \to \tau^+\tau^-$ samples agree well.

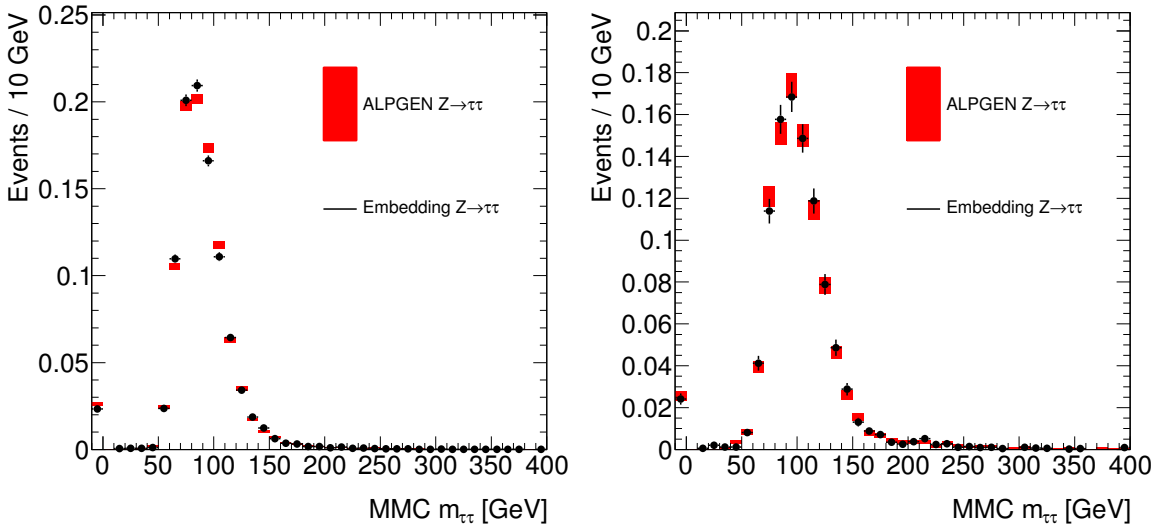

Figure 6.1: Distribution of the MMC $m_{\tau\tau}$ shape for events generated with ALPGEN and embedding events after the charge correlation criterion (left) and after the full event selection (right). The distributions are normalized to unity. The bin below zero contains events where the MMC $m_{\tau\tau}$ calculation did not converge. The shown uncertainties are only statistical.

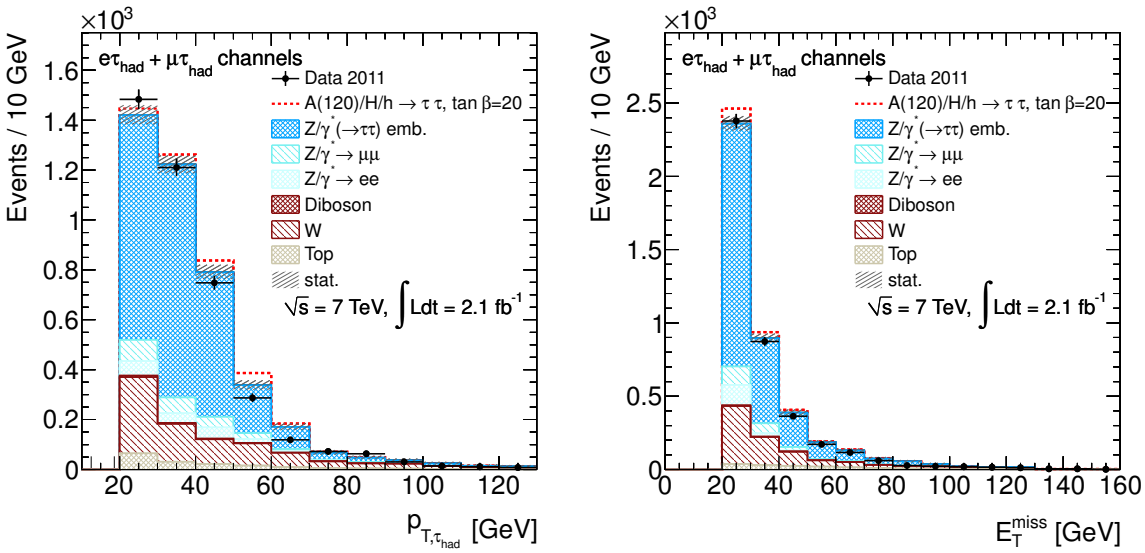

Figure 6.2: Distribution of the transverse momentum of the τ_{had} candidate $p_{\text{T},\tau_{\text{had}}}$ (left) and the missing transverse energy $E_{\text{T}}^{\text{miss}}$ (right) after the full selection and the MMC $m_{\tau\tau}$ mass reconstruction. Shown are the data, a signal sample ($m_A = 120\,\text{GeV}$, $\tan\beta = 20$) on top of background samples from simulation and the $Z/\gamma^* \to \tau^+\tau^-$ embedding sample and the statistical uncertainty of the combined background samples. No simulated QCD multi-jet events are included.

6.2 W + Jets Normalization

Backgrounds from W + jets processes are estimated using events from simulation, however the normalization is checked in a data control region, namely the high transverse mass region, where the simulated W + jets sample has been shown not to agree well with the data in Chapter 5.4. For events with a real W boson decaying into a lepton and a neutrino the transverse mass distribution m_{T} has a peak around the mass of the W boson. For background events that do not contain real W bosons and for signal events the m_{T} distribution is peaking at zero. In particular events from QCD multi-jet production are not expected to result in high values of m_{T}.

In Figure 6.3 the distribution of the transverse mass m_{T} after the charge correlation criterion (a) and after the $E_{\mathrm{T}}^{\mathrm{miss}}$ criterion (b) is shown in data and simulation. As expected almost all events at high values of the m_{T} distribution are due to W + jets background events, as this process is the most abundant one containing real W bosons. Hence the high transverse mass region can be used to check and correct the normalization of the W + jets background with data. The comparison is made after the charge correlation criterion (Figure 6.3 (a)) as the correction can be different for OS and SS events. The m_{T} distribution after the $E_{\mathrm{T}}^{\mathrm{miss}}$ selection criterion, the latest possible selection step before the m_{T} distribution itself is used in the selection, is shown in Figure 6.3 (b). The distribution at this selection step can later be used to judge the effect of the correction applied to the W + jets backgrounds.

A correction is needed as the yield of W + jets events is clearly overestimated in the simulation, which is due to fake tau candidates not being correctly modeled.To correct the normalization, correction factors f_W are obtained by comparing the transverse mass distribution of data and simulation in the region dominated by W decays (70 GeV to 110 GeV), this is done for both the OS and the SS region. The factors are obtained after the charge correlation selection step (i.e. for opposite-sign events) by subtracting the small non-W contribution (estimated from simulation) from the data and then dividing by the number of events found in the W + jets simulated sample:

$$f_W^{\ell} = \frac{n_{\mathrm{data}}\,(70\ \mathrm{GeV}, 110\ \mathrm{GeV}) - n_{\mathrm{non-}W,\ \mathrm{MC}}\,(70\ \mathrm{GeV}, 110\ \mathrm{GeV})}{n_{W,\ \mathrm{MC}}\,(70\ \mathrm{GeV}, 110\ \mathrm{GeV})}. \tag{6.1}$$

Events from QCD multi-jet production, where no simulation samples are used, are neglected as they are not expected to contribute in the control region. In addition, correction factors are estimated for same-sign events as the QCD multi-jet background estimate described in the next section needs a prediction for the W + jets background in the low m_{T} same-sign region.

For opposite-sign events the factor is found to be $f_W^e = (60.4 \pm 2.6)\%$ for the electron channel and $f_W^{\mu} = (55.0 \pm 2.2)\%$ for the muon channel and for same-sign events it is $f_W^{e\mathrm{SS}} = (80.0 \pm 5.0)\%$ and $f_W^{\mu\mathrm{SS}} = (75.8 \pm 4.0)\%$.

The transverse mass distributions with the correction factors applied are shown in Figure 6.3, both after requiring charge correlation (c) and after the $E_{\mathrm{T}}^{\mathrm{miss}}$ selection criterion (d). The agreement of the simulation with the data is much improved in the W boson mass peak region. After the charge correlation criterion a lack of events in the simulation at lower values of m_{T} is visible, that is due to the QCD multi-jet background not being considered here. As this background is strongly suppressed by the $E_{\mathrm{T}}^{\mathrm{miss}}$ selection criterion the agreement is also much better overall after it has been applied.

The estimated W + jets background after the full selection, including the application of the MMC, amounts to 467 ± 20 events.

In Figure 6.4 the distribution of the transverse momentum of the τ_{had} candidate $p_{\mathrm{T},\tau_{\mathrm{had}}}$ and the missing transverse energy $E_{\mathrm{T}}^{\mathrm{miss}}$ are presented for comparison again, now with the W + jets correction factors applied.

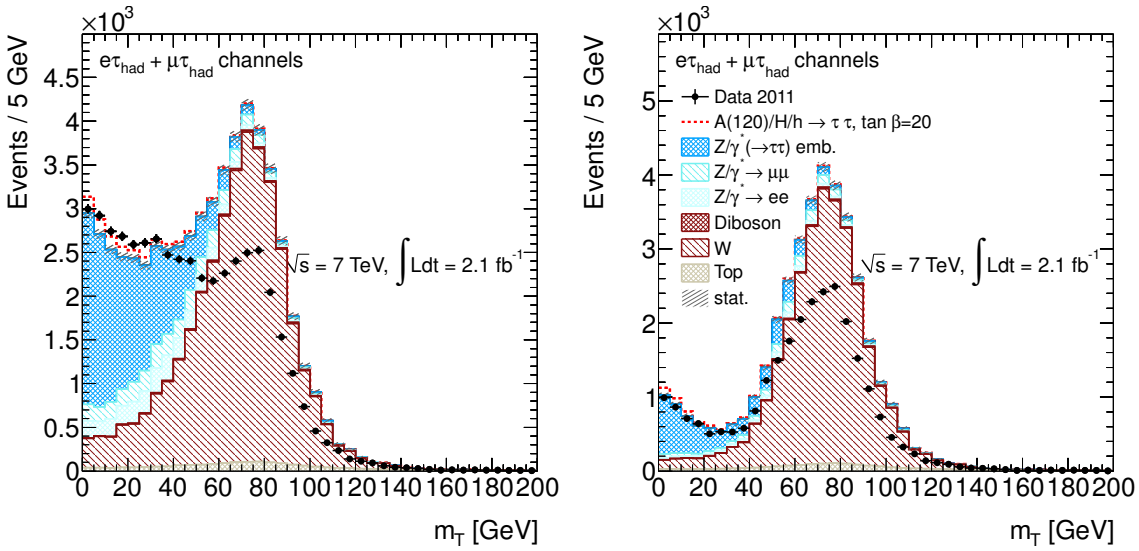

(a) W + jets unscaled

(b) W + jets unscaled

(c) W + jets scaled

(d) W + jets scaled

Figure 6.3: Distribution of the transverse mass m_{T} without (top) and with (bottom) W + jets correction factors applied after the charge correlation (left) and the $E_{\mathrm{T}}^{\mathrm{miss}}$(right) selection are applied. Shown are the data, a hypothetical signal ($m_A = 120$, $\tan\beta = 20$) sample, background samples from simulation and the $Z/\gamma^* \rightarrow \tau^+\tau^-$ embedding sample. No QCD multi-jet estimation is included.

Except for small values of p_T and E_T^{miss}in the first bin of the distribution the estimated background samples agree well with the data. The only relevant background events that have not been included yet are those from QCD multi-jet processes. As events from QCD multi-jet processes can only pass the event selection if objects, most probably jets, have been misidentified as τ_{had} candidates and as isolated light leptons, which is more likely to happen at low transverse momenta, and as they tend not to have any significant amount of E_T^{miss}, the missing events in Figure 6.4 are very likely due to QCD multi-jet processes. In the following Section 6.3 a method to estimated this last missing background sample will be introduced.

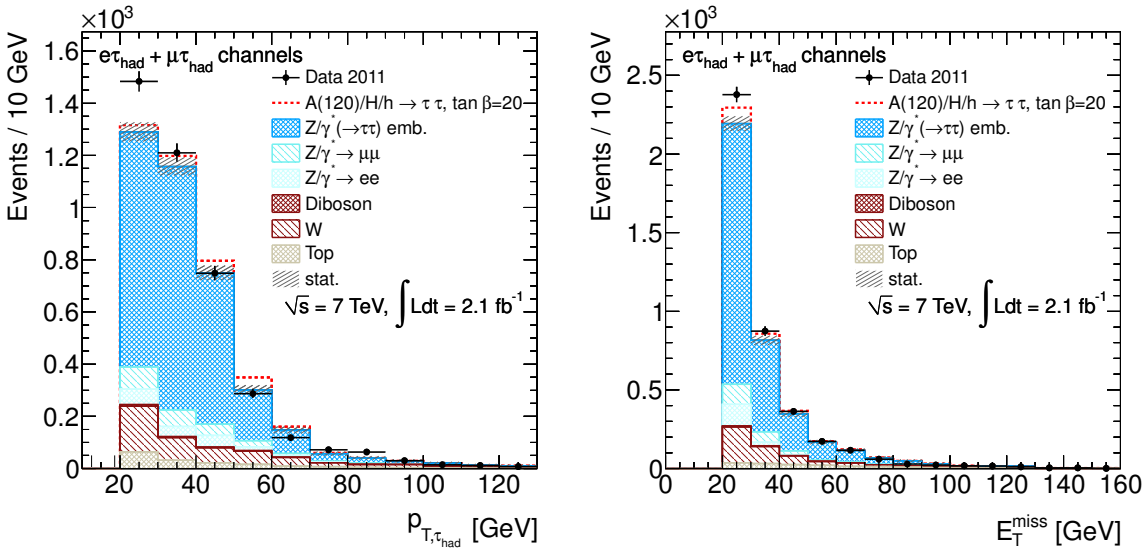

Figure 6.4: Distribution of the transverse momentum of the τ_{had} candidate $p_{T,\tau_{had}}$ (left) and the missing transverse energy E_T^{miss} (right) with the W + jets correction factor applied after the full selection including the application of the MMC. Shown are the data, a signal sample (m_A = 120 GeV, $\tan\beta$ = 20) on top of background samples from simulation and the $Z/\gamma^* \to \tau^+\tau^-$ embedding sample and the statistical uncertainty of the combined background samples. No simulated QCD multi-jet events are included.

6.3 QCD Multi-Jet Estimate

As has been visible in the distributions in Figure 6.4 events from QCD multi-jet processes seem to pass the selection and need to be estimated. Even though the contribution of this background is expected to be small compared to the $Z/\gamma^* \to \tau^+\tau^-$ and W + jets backgrounds it is important to estimate it from data as both the simulation and the prediction of the production cross section for QCD multi-jet processes are difficult and therefore simulation normalized to theory prediction cannot be relied on.

A method to estimate both the shape of the MMC $m_{\tau\tau}$ distribution and the normalization of the QCD multi-jet background is described in the following. It uses two variables to split the data sample into four sub-regions, one of those being the signal region, while the other three are data control regions and should be free from signal contributions. The regions are labeled A,B,C and D. The two variables used are the charge correlation between the light lepton and the τ lepton ("opposite-sign" versus "same-sign") and the isolation of the lepton[1] ("isolation" versus "inverted isolation").

[1] For electrons (muons) the isolation criteria are $E_T^{\Delta R<0.2}/p_T < 0.08$ and $p_T^{\Delta R<0.4}/p_T < 0.06$ ($E_T^{\Delta R<0.2}/p_T < 0.04$ and $p_T^{\Delta R<0.4}/p_T < 0.06$), also see Section 5.2.

In Table 6.1 it is illustrated which selection corresponds to which region.

	Isolation	Inverted Isolation
Opposite-Sign	A (Signal)	B
Same-Sign	C	D

Table 6.1: Definition of signal and control regions for the QCD multi-jet estimate in dependence of the charge correlation between the light lepton and the τ lepton (opposite-sign vs. same-sign) and the isolation of the light lepton (isolation vs. inverted isolation).

To estimate the QCD multi-jet background in the signal region the data in control Region C is used to estimate the MMC $m_{\tau\tau}$ shape and it is normalized by comparing Region B to D.

The two variables used for this method should not be correlated and the control regions should ideally be dominated by events originating from QCD multi-jet processes. However, small residual contamination from electroweak processes are subtracted using the Monte Carlo simulation prediction and the $Z/\gamma^* \rightarrow \tau^+\tau^-$ embedding samples.

Control Regions

The distributions of the isolation variables defining the control regions are shown in Figures 6.5 and 6.6 for selected electrons and muons, respectively. The regions with the inverted isolation (B and D) are dominated by QCD multi-jet events and hardly any non-QCD multi-jet backgrounds are left. The same-sign region with isolated leptons (C) has a significant non-QCD multi-jet background contribution that needs to be subtracted. The corresponding numbers of data, simulation and embedding events are shown in Table 6.2. The ratio of events from the two regions used for the normalization, $r_{\mathrm{B/D}}$, after subtraction of non-QCD multi-jet components is

$$r_{\mathrm{B/D}} = 1.16 \pm 0.02, \tag{6.2}$$

were only the statistical uncertainty is given.

Using the ratio $r_{\mathrm{B/D}}$ and the number of non-QCD multi-jet subtracted data events from region C, $n_{\mathrm{C}}^{\mathrm{subtracted}}$, the number of estimated QCD multi-jet events in Region A is given by

$$n_{\mathrm{A}}^{\mathrm{estimate}} = r_{\mathrm{B/D}} \times n_{\mathrm{C}}^{\mathrm{subtracted}} = 308 \pm 37, \tag{6.3}$$

were only the statistical uncertainty is given.

Method Validation

To check if the variables are correlated, the combined regions $A + B$ and $C + D$ ($A + C$ and $B + D$), i.e. opposite-sign versus same-sign (isolation versus inverted isolation), are compared.

If the variables are uncorrelated for QCD multi-jet processes all distributions should have the same shapes in the half-planes, i.e. $A + B$ ($A + C$) should be similar to $C + D$ ($B + D$). As no simulated QCD multi-jet samples of sufficient statistics are available the data has to be used for this check. After subtracting the non-QCD multi-jet background contributions from the data in control regions B, C and D the remaining events are from QCD multi-jet processes. However, in the signal region a potential signal contribution cannot be subtracted. Therefore to avoid a potentially large signal contribution in region A the comparison of the half-planes is shown at an earlier selection step, namely before the $E_{\mathrm{T}}^{\mathrm{miss}}$ selection criterion is applied, where the backgrounds are dominant.

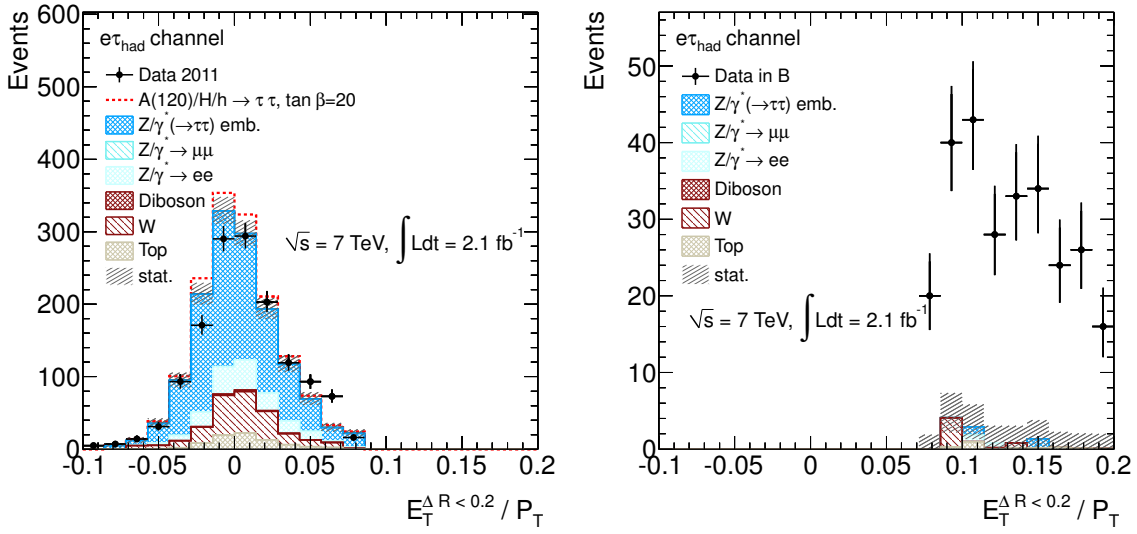

(a) Region A – Signal Region

(b) Region B – Inverted Isolation

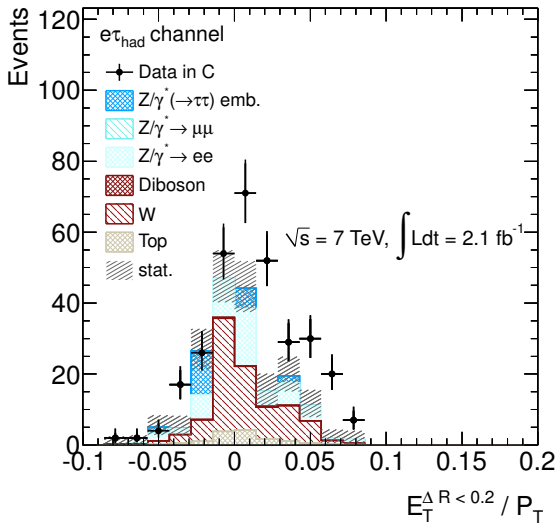

(c) Region C – Same-Sign

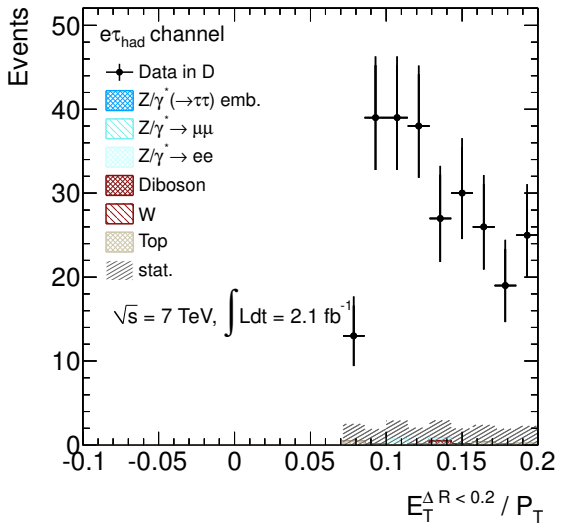

(d) Region D – Same-Sign & Inverted Isolation

Figure 6.5: Distribution of the isolation variable (ratio of the calorimeter energy in a cone of radius $\Delta R = 0.2$ around the electron direction and p_T^e) for selected electrons in the four control regions. The data are compared to the backgrounds estimated from simulation and embedding at the end of the selection. As expected, the data is not described by the simulation in the control regions as no contribution for the QCD multi-jet background is included.

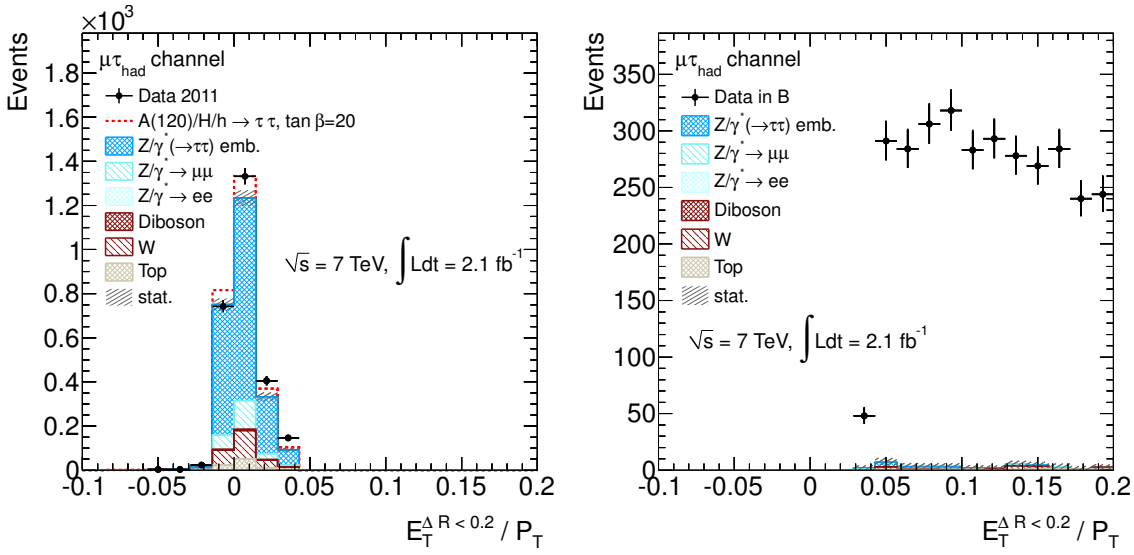

(a) Region A – Signal Region

(b) Region B – Inverted Isolation

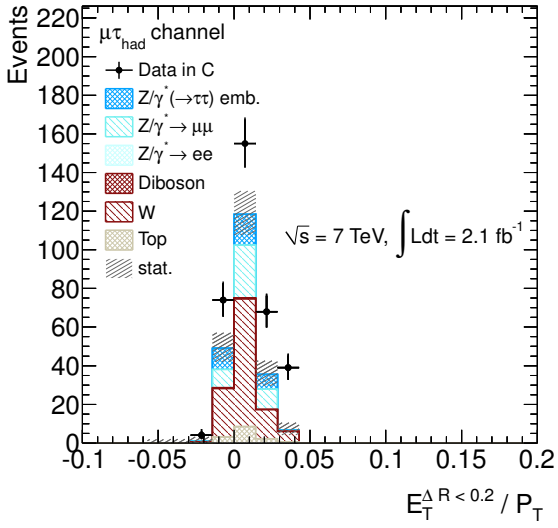

(c) Region C – Same-Sign

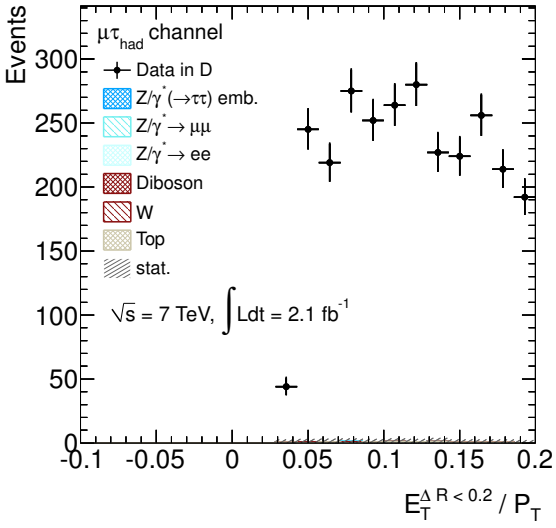

(d) Region D – Same-Sign & Inverted Isolation

Figure 6.6: Distribution of the isolation variable (ratio of the calorimeter energy in a cone of radius $\Delta R = 0.2$ around the muon direction and p_{T}^{μ}) for selected muons in the four control regions. The data are compared to the backgrounds estimated from simulation and embedding at the end of the selection. As expected, the data is not described by the simulation in the control regions as no contribution for the QCD multi-jet background is included.

	A	B	C	D
Data	4065	9674	654	8306
Signal (m_A = 120 GeV,tanβ = 20)	342 ± 11	2.4 ± 0.6	2.3 ± 0.8	-
Di-Boson	19.3 ± 1.2	0.4 ± 0.1	2.0 ± 0.4	0.03 ± 0.01
W + jets	467 ± 20	26.8 ± 6.1	198 ± 15	2.5 ± 0.8
$Z/\gamma^* \rightarrow e^+e^-$	167 ± 9	2.4 ± 1.3	54 ± 5	1.0 ± 0.7
$Z/\gamma^* \rightarrow \mu^+\mu^-$	233 ± 12	4.1 ± 1.5	48 ± 6	1.1 ± 0.5
$Z/\gamma^* \rightarrow \tau^+\tau^-$	2790 ± 49	18.7 ± 3.0	57 ± 8	1.4 ± 1.2
Top	167 ± 3	51 ± 3	28 ± 1	40 ± 3
Sum	3844 ± 56	103 ± 8	388 ± 19	46 ± 4

Table 6.2: Observed data events and expected numbers of events from simulation and embedding in the four regions used in the QCD multi-jet background estimation. For the W + jets samples the correction factors (see Section 6.1) are applied. The full event selection is applied and the MMC $m_{\tau\tau}$ has been reconstruction. The quoted errors are statistical.

It is worth noting, that the potential signal is not a problem for the actual estimate, only for the correlation check, as the estimate only uses regions B, C and D.

In Figure 6.7 this comparison of QCD multi-jet (data with non-QCD multi-jet backgrounds subtracted) is shown in the combined regions $A + B$ and $C + D$ ($A + C$ and $B + D$) for the $E_{\mathrm{T}}^{\mathrm{miss}}$ and the MMC $m_{\tau\tau}$ distributions before the $E_{\mathrm{T}}^{\mathrm{miss}}$ selection criterion is applied. For the comparison of $A + B$ and $C + D$ the distributions agree within their statistical uncertainties. Due to the small number of events in $A + C$ a comparison with $B + D$ is more difficult. The observed differences while statistically significant can be considered small enough, especially as there are additional systematic uncertainties not being considered at this point (see Chapter 7). Hence the two variables are assumed to be uncorrelated.

As an additional check, the isolation requirement is varied and the background estimate is then repeated with stricter and less strict isolation for electrons and muons separately. While the amount of estimated QCD multi-jet events is expected to change with different isolation criteria applied, the ratio $r_{\mathrm{B/D}}$, i.e. the ratio of opposite-sign and same-sign events in the inverted isolation control region is expected to be independent of the isolation criterion chosen. The results presented in Table 6.3 and Figure 6.8 show no significant deviation in the ratio.

In conclusion, the QCD multi-jet estimation method is reliable and stable under various checks performed, and is hence used in the following.

$r_{\mathrm{B/D}}$	Less Strict Isolation	Normal Isolation	Stricter Isolation
Electron Channel	1.04 ± 0.08	1.04 ± 0.07	1.00 ± 0.06
Muon Channel	1.16 ± 0.02	1.17 ± 0.02	1.16 ± 0.02
Combined	1.16 ± 0.02	1.16 ± 0.02	1.15 ± 0.02

Table 6.3: Ratio $r_{\mathrm{B/D}}$, i.e. the ratio of opposite-sign and same-sign events in the inverted isolation control region, for less strict isolation ($E_{\mathrm{T}}^{\Delta R<0.2}/p_{\mathrm{T}} < 0.10$ (0.06) for electrons (muons)), normal isolation ($E_{\mathrm{T}}^{\Delta R<0.2}/p_{\mathrm{T}} < 0.08$ (0.04) for electrons (muons)) and stricter Isolation ($E_{\mathrm{T}}^{\Delta R<0.2}/p_{\mathrm{T}} < 0.06$ (0.02) for electrons (muons)).

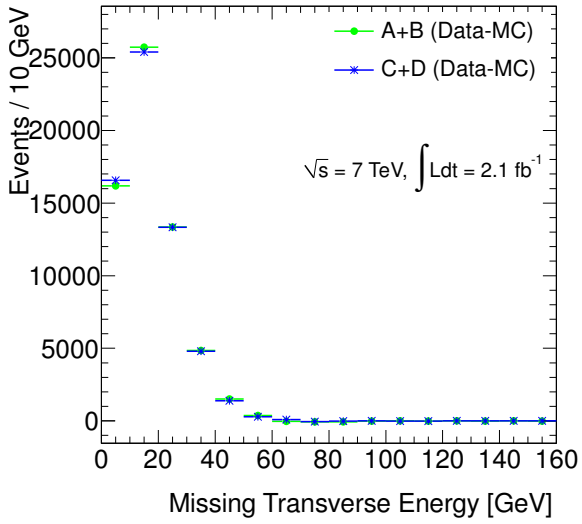

(a) AB vs. CD

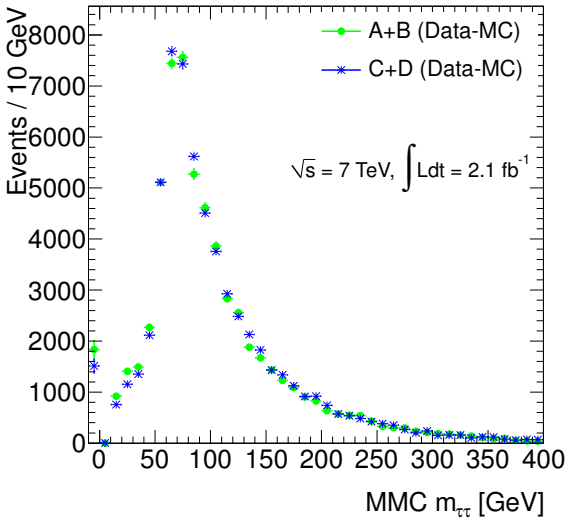

(b) AB vs. CD

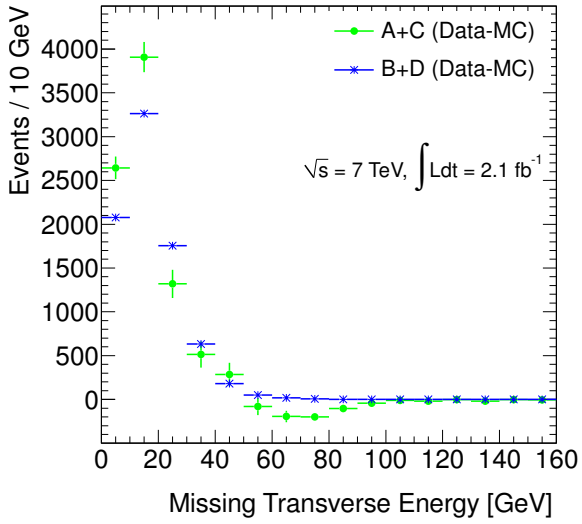

(c) AC vs. BD

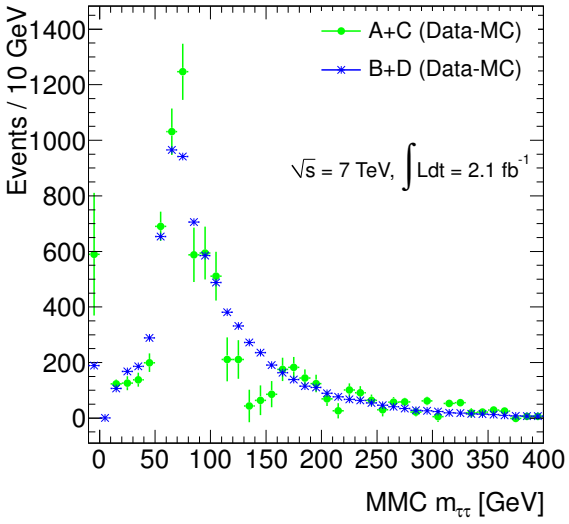

(d) AC vs. BD

Figure 6.7: Top: Comparison of the combined regions $A + B$ (green) and $C + D$ (blue) (i.e. opposite-sign versus same-sign). Bottom: Comparison of combined regions $A + C$ (green) and $B + D$ (blue) (i.e. isolation versus inverted isolation). Shown are the non-QCD multi-jet subtracted data distributions of $E_{\mathrm{T}}^{\mathrm{miss}}$ (left) and MMC $m_{\tau\tau}$ (right) before the $E_{\mathrm{T}}^{\mathrm{miss}}$ selection criterion is applied. In the top (bottom) two figures the distribution in the combined region $C + D$ ($B + D$) is normalized to the yield in the combined region $A + B$ ($A + C$).

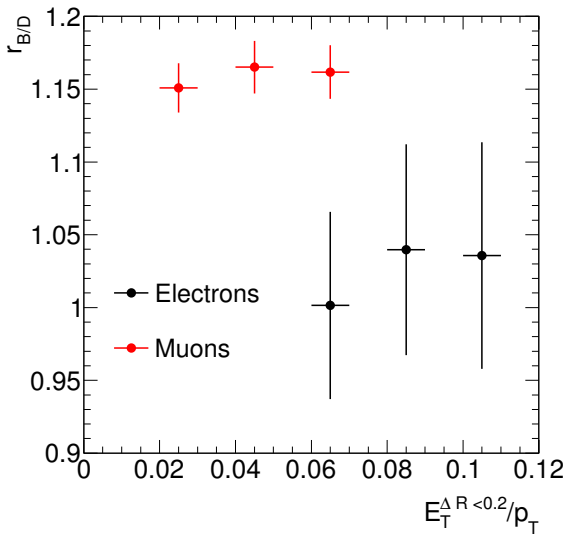

Figure 6.8: Ratio $r_{\mathrm{B/D}}$, i.e. the ratio of opposite-sign versus same-sign events in the inverted isolation control region in dependence of $E_{\mathrm{T}}^{\Delta R<0.2}/p_{\mathrm{T}}$.

6.4 Results with Background Estimates from Data

The final comparisons of the distributions of the transverse momentum of the τ_{had} candidate $p_{\mathrm{T},\tau_{\mathrm{had}}}$ and the missing transverse energy $E_{\mathrm{T}}^{\mathrm{miss}}$ in the data and the estimated background samples is presented in Figure 6.9. With the addition of the QCD multi-jet background estimate the overall agreement is good. However, the presence of a resonant signal can be observed best in the di-τ mass distribution. Different methods to estimated it are available (as described earlier, see Section 5.5). The final MMC $m_{\tau\tau}$ distribution is shown in Figure 6.10. For comparison the visible mass distribution is shown in the same figure. The main difference between the two mass distributions is that the $Z/\gamma^* \rightarrow \tau^+\tau^-$ peak region is correctly located close to the mass of the Z boson in the MMC $m_{\tau\tau}$ distribution and located at much lower values for the visible mass distribution.

The estimated background distributions agree with the data within the shown statistical and the systematic uncertainties discussed in Chapter 7.

In Figure 6.11 and 6.12 distributions ($p_{\mathrm{T},\tau_{\mathrm{had}}}$, lepton p_{T}, $E_{\mathrm{T}}^{\mathrm{miss}}$ and MMC $m_{\tau\tau}$) after the final selection and with the full background estimation are shown for the $e\tau_{\mathrm{had}}$ and the $\mu\tau_{\mathrm{had}}$ channels separately. The disagreement of the simulation with the data around the Z boson mass peak, i.e. for $Z/\gamma^* \rightarrow \tau^+\tau^-$ events is observed in the statistically less precise $e\tau_{\mathrm{had}}$ channel, while the $\mu\tau_{\mathrm{had}}$ channel shows better, but also not perfect agreement.

For both channels, as well as for the combination of the two, the difference between simulation and data, e.g. in the MMC mass distribution between roughly 50 GeV and 150 GeV, is covered by the large uncertainty on the $Z/\gamma^* \rightarrow \tau^+\tau^-$ background due to the τ_{had} and jet energy scale uncertainty that will be discussed, together with all other systematic uncertainties, in the next chapter (see Section 7.1.1).

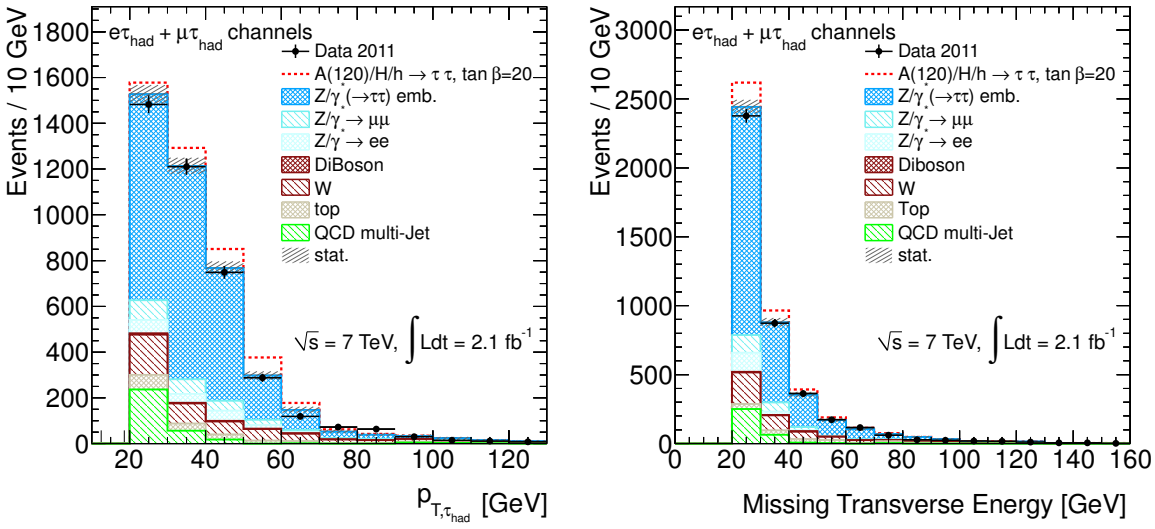

Figure 6.9: Distribution of the transverse momentum of the τ_{had} candidate $p_{\text{T},\tau_{\text{had}}}$ (left) and the missing transverse energy $E_{\text{T}}^{\text{miss}}$ (right) after the full selection and the MMC $m_{\tau\tau}$ mass reconstruction. Shown are the data, a hypothetical signal sample with $m_A = 120$ and $\tan\beta = 20$, the QCD multi-jet sample estimated from data control region C, the $Z/\gamma^* \to \tau^+\tau^-$ embedding sample, the W + jets sample normalized in the high-m_{T} data control region and the other backgrounds from simulated samples.

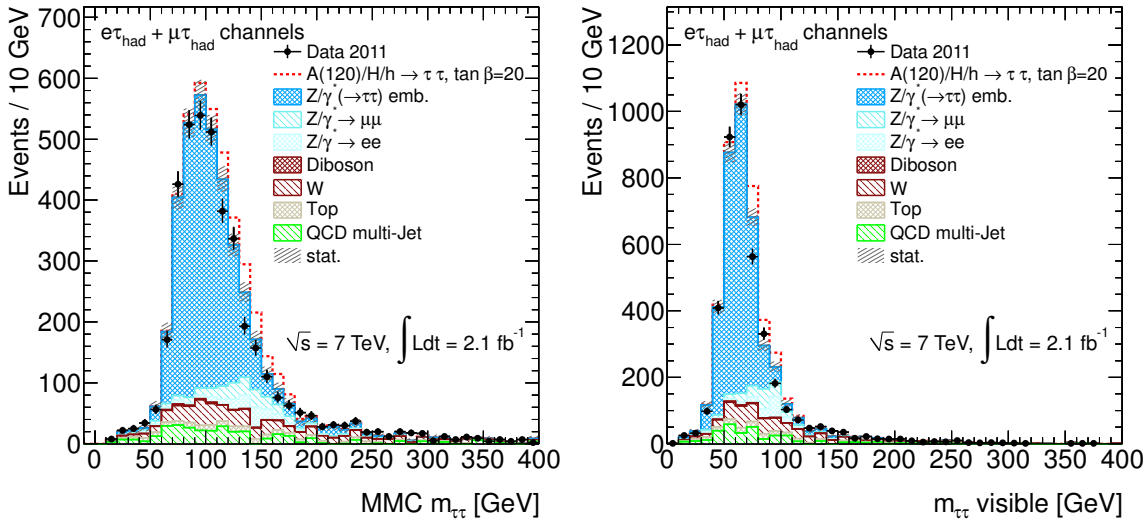

Figure 6.10: Distribution of the MMC $m_{\tau\tau}$ and the visible di-τ mass after the full selection. Shown are the data, a hypothetical signal with $m_A = 120$ and $\tan\beta = 20$, QCD multi-jet estimated from data control region C, $Z/\gamma^* \to \tau^+\tau^-$ embedding, W + jets normalized in the high-m_{T} data control region and the other backgrounds from simulation samples.

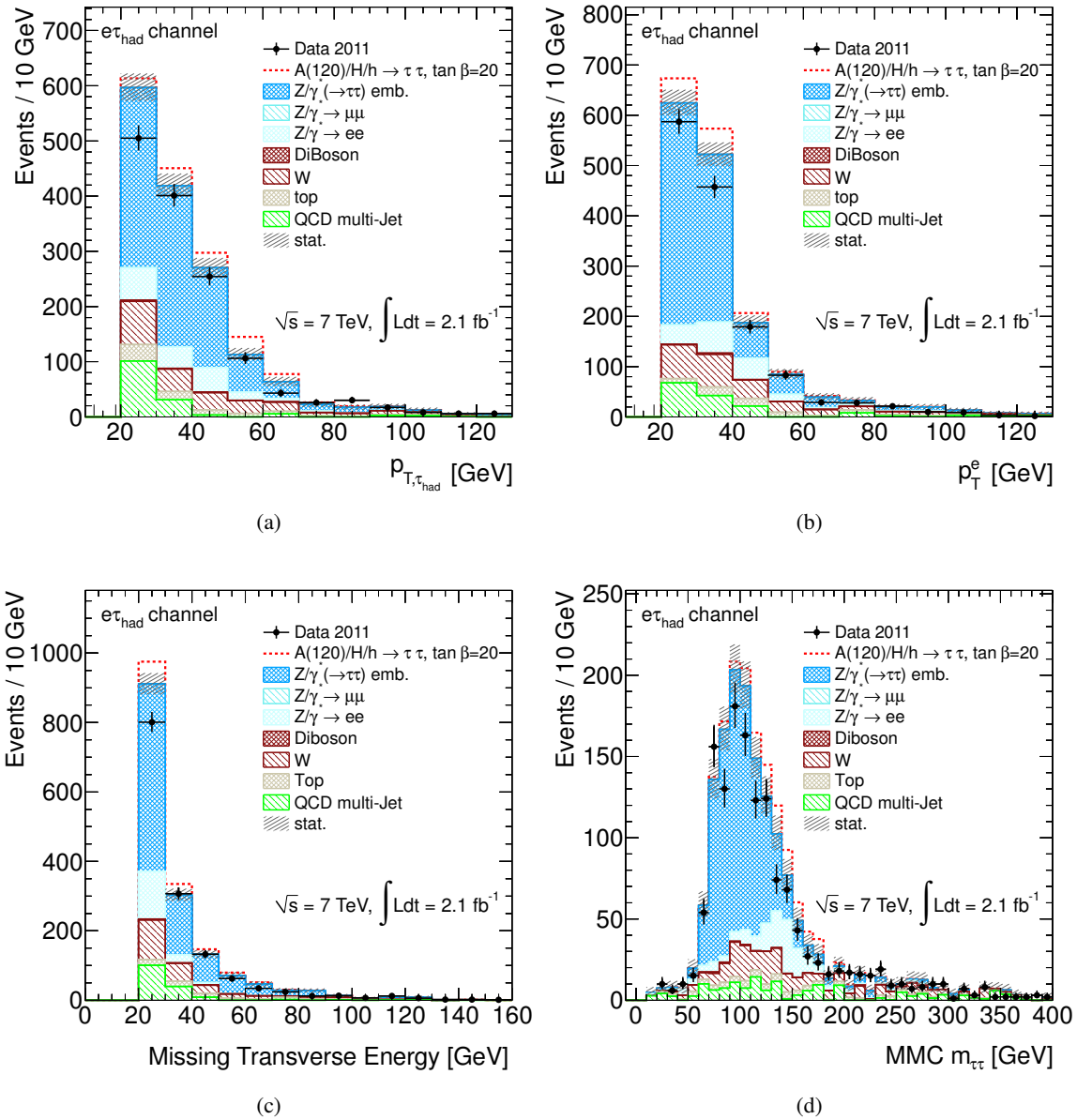

Figure 6.11: ***eτ*had channel:** Distribution of the τ_{had} candidate $p_{\text{T},\tau_{\text{had}}}$ (a), the electron p_{T}^{e} (b), the missing transverse energy $E_{\text{T}}^{\text{miss}}$ (c) and the MMC $m_{\tau\tau}$ (d) mass after the full selection after the full selection and the MMC $m_{\tau\tau}$ mass reconstruction. Shown are the data, a hypothetical signal sample with $m_A = 120$ and $\tan\beta = 20$, the QCD multi-jet sample estimated from data control region C, the $Z/\gamma^* \to \tau^+\tau^-$ embedding sample, the W + jets sample normalized in the high-m_{T} data control region and the other backgrounds from simulated samples.

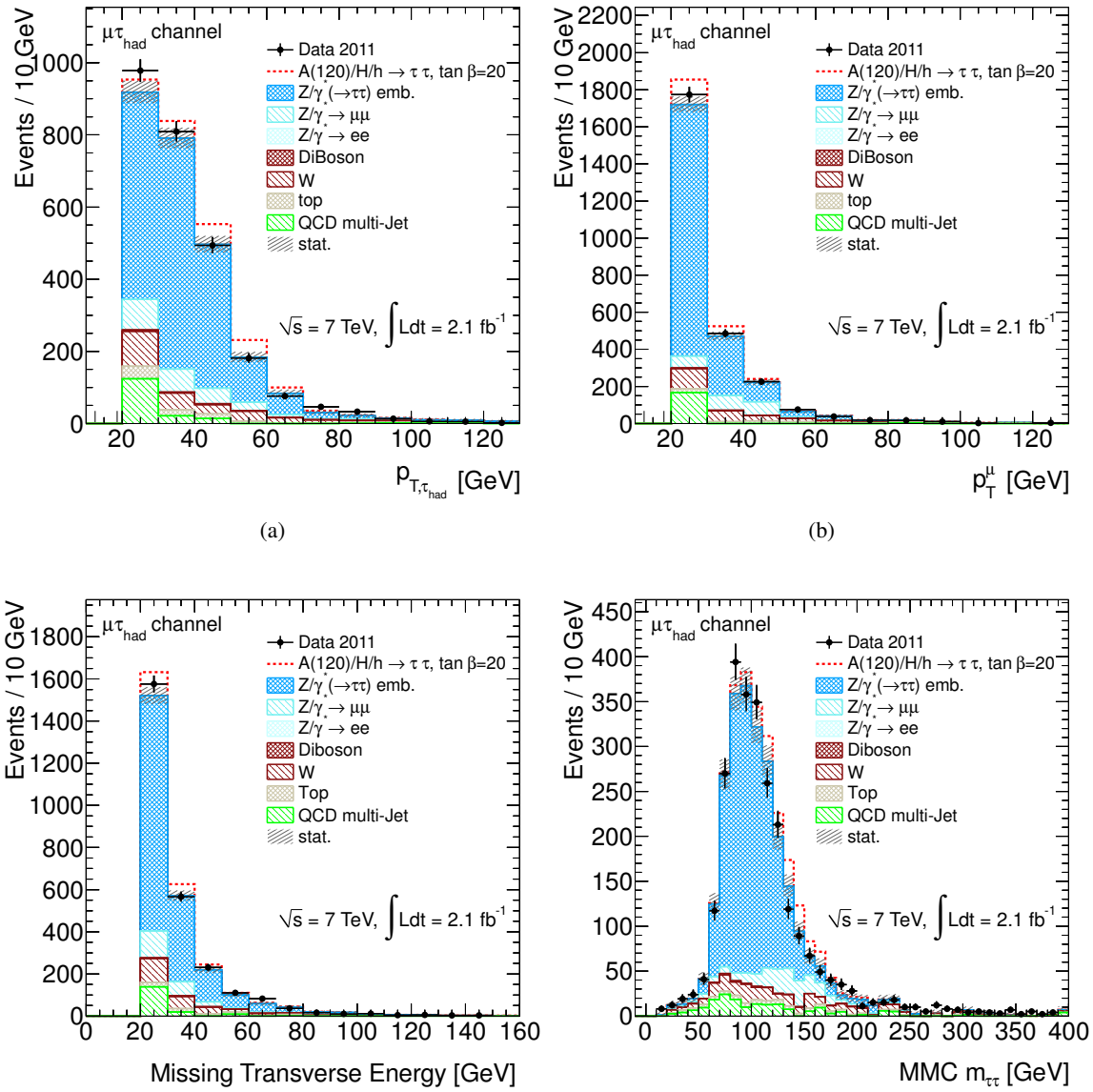

Figure 6.12: $\boldsymbol{\mu\tau_{\text{had}}}$ **channel:** Distribution of the τ_{had} candidate $p_{\text{T},\tau_{\text{had}}}$ (a), the electron p_{T}^{μ} (b), the missing transverse energy $E_{\text{T}}^{\text{miss}}$ (c) and the MMC $m_{\tau\tau}$ (d) mass after the full selection and the MMC $m_{\tau\tau}$ mass reconstruction. Shown are the data, a hypothetical signal sample with $m_A = 120$ and $\tan\beta = 20$, the QCD multi-jet sample estimated from data control region C, the $Z/\gamma^* \to \tau^+\tau^-$ embedding sample, the W + jets sample normalized in the high-m_{T} data control region and the other backgrounds from simulated samples.

Chapter 7

Systematic Uncertainties

The modeling of both the detector response and the physics processes in the simulation as well as the needed theoretical predictions used in the analysis are not perfect. Therefore they lead to systematic uncertainties on the yield and the shape of the MMC $m_{\tau\tau}$ distribution that need to be taken into account.

In addition, uncertainties due to the background estimation methods used and the uncertainty on the luminosity measurement are considered.

7.1 Reconstruction Uncertainties

7.1.1 Energy Scales and Resolutions

Due to disagreement between the energy measurement in data and in simulation both the overall energy scale and the resolution need to be corrected in the simulation and have a systematic uncertainty assigned to them. The uncertainties on the energy of the object in question, e.g. electrons, jets, etc., are propagated to the missing transverse energy vector[1] $\vec{E}_{\mathrm{T}}^{\mathrm{miss}}$.

Typical electron energy scale uncertainties are in the 1% region [69]. To correct the electron energy resolution in the simulation, the measured energy is folded with a Gaussian resolution function with an average width of $1-4\%$. This correction itself has an uncertainty of $0.2\%-2\%$. The effect of the electron energy uncertainties on the event yield is given in Table 7.1. No significant deviation in the MMC mass shapes are observed.

For muon candidates the transverse momentum in both the inner detector and the muon system are smeared within their resolution to estimate the uncertainty on the transverse momentum. The resolution in the inner detector (muon system) is given by $\sigma(p_{\mathrm{T}})/p_{\mathrm{T}} = \sqrt{(0.00624)^2 + (0.000299 \cdot (p_{\mathrm{T}}/\ \mathrm{GeV}))^2}$ ($\sigma(p_{\mathrm{T}})/p_{\mathrm{T}} = \sqrt{(0.02035)^2 + (0.000129 \cdot (p_{\mathrm{T}}/\ \mathrm{GeV}))^2}$) for muons in the central detector region ($|\eta| < 1.05$ [78]. The effect of this uncertainty on the event yield is small ($< 0.5\%$) for most samples (see Table 7.1). The effect is only of notable size for $Z/\gamma^* \rightarrow \mu^+\mu^-$ (0.6%) and the statistical less precise background samples $Z/\gamma^* \rightarrow e^+e^-$ (2.11%) and QCD multi-jet estimated from data (0.6%). Here only a very small sample containing reconstructed muons is selected and hence the resulting uncertainies are negligible.

The typical energy scale uncertainty for jets and τ_{had} candidates is of the order of 5% [72, 79]. As τ_{had} candidates are seeded from jets the uncertainty is treated as being fully correlated for jets and τ_{had} candidates. Jets in the $Z/\gamma^* \rightarrow \tau^+\tau^-$ embedding samples are assumed to have no uncertainty as they are taken directly from data. In Table 7.1 the effect of the jet/τ_{had} energy uncertainties on the event yield is shown. The jet/τ_{had} energy uncertainty has the biggest influence on the overall result and its effect on the shape of the MMC mass distributions is taken into account.

[1] As the analysis selection is not directly using jets this is the only way the jet energy scale uncertainty has an effect on the final results.

In Figure 7.1 comparisons of the MMC mass distributions for the nominal jet/τ_{had} energy scale and its up- and down variations are shown. A clear difference in the shapes of the distributions is visible. Therefore this uncertainty on the MMC mass shapes due to the jet/τ_{had} energy scale uncertainty is propagated into the final limit estimation (see Chapter 8).

The typical energy resolution for jets in the central detector region and with transverse momenta of $p_{\text{T}} = 250$ GeV (10 GeV) is 4% (20%) [80].

The resolution of the missing transverse energy $E_{\text{T}}^{\text{miss}}$ is $\approx$ 3 (7) GeV for a sum of all transverse energies $E_{\text{T}} = \sum E_{\text{T}} = 50$ (7) GeV [81]. In order to estimate the uncertainty due to the limited $E_{\text{T}}^{\text{miss}}$ resolution, $E_{\text{T}}^{\text{miss}}$ is varied within the resolution. The results are shown in Table 7.1.

	Electron Energy Scale	Electron Energy Resolution	Jet/Tau Energy Scale Up/Down	Jet Energy Resolution	$E_{\text{T}}^{\text{miss}}$ Resolution
Signal ($m_A = 120$ GeV)	0.1	0.01	$^{+17}_{-13}$	0.3	0.1
Diboson	0.4	0.4	$^{+13}_{-13}$	0.5	0.3
W + jets	0.9	0.2	$^{+11}_{14}$	1.1	0.4
$Z/\gamma^* \rightarrow e^+e^-$	2.3	1.7	$^{+37}_{-25}$	3.1	2.4
$Z/\gamma^* \rightarrow \mu^+\mu^-$	0.4	0.4	$^{+24}_{-16}$	0.4	0.4
$Z/\gamma^* \rightarrow \tau^+\tau^-$	0.3	0.3	$^{+25}_{-16}$	0.4	0.4
Top	0.2	0.2	$^{+7}_{-15}$	0.1	0.1
QCD multi-jet	1.2	1.8	$^{-34}_{+24}$	1.3	0.3

Table 7.1: Effect on the event yield in % of the energy scale and resolution uncertainties on an example signal sample, simulated background samples, the $Z/\gamma^* \rightarrow \tau^+\tau^-$ embedding sample and the QCD multi-jet sample estimated from data.

7.1.2 Particle Identification, Reconstruction and Trigger Efficiency

The efficiency of the identification of electrons [69], muons [78] and τ_{had} candidates [72] is different in data and simulation and correction factors are applied.

In case of the electrons the η dependent scale factors are within $\approx$ 10% of unity and have relative

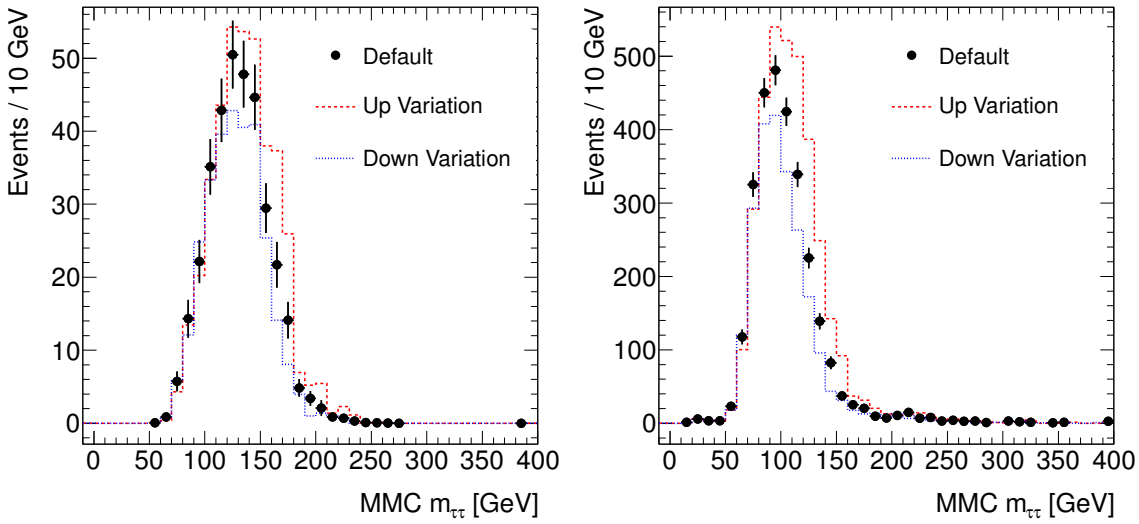

(a) Signal $m_A = 120$ GeV, $\tan\beta = 20$

(b) $Z/\gamma^* \to \tau^+\tau^-$

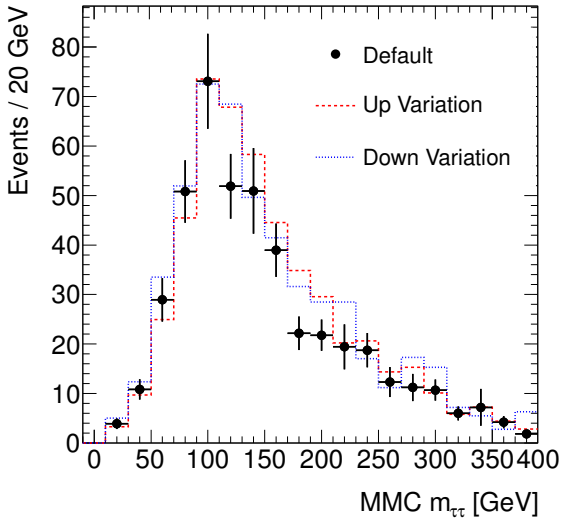

(c) W + jets

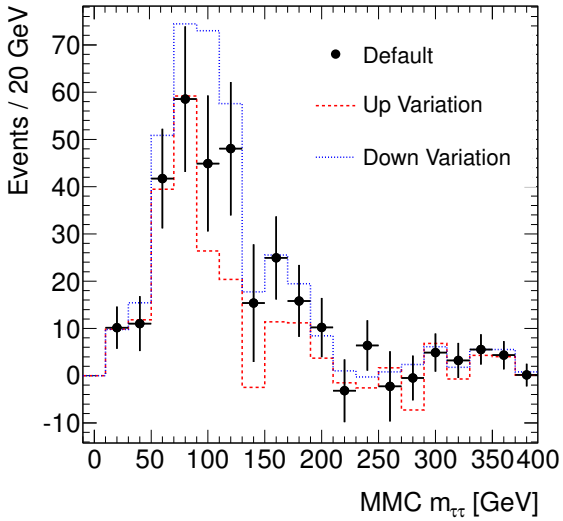

(d) QCD multi-jet

Figure 7.1: Comparison of the MMC mass distribution with the nominal jet/τ_{had} energy scale and the up- and downward variations applied. The distributions are shown for a potential signal ($m_A = 120$ GeV, $\tan\beta = 20$ GeV), the $Z/\gamma^* \to \tau^+\tau^-$ embedding sample, the W + jets sample from simulation and the QCD multi-jet sample obtained from data.

uncertainties of $\approx 1-2\%$ for the identification, and within $\approx 1-3\%$ of unity with relative uncertainties of $\approx 1\%$ for both the track reconstruction and the trigger modeling. The effect on the event yield of this electron identification and reconstruction uncertainties is shown in Table 7.2. The biggest effect is observed for the $Z/\gamma^* \to e^+e^-$ sample, where two electrons are present. As events with more than one identified electron are vetoed, the yield for this sample depends highly on the electron identification and reconstruction efficiencies.

For muons the scale factors used to correct the simulation are consistent with unity and have a relative uncertainty of 1.8%. In Table 7.2 the event yield uncertainties due to the muon identification uncertanties are shown. Again the $Z/\gamma^* \to e^+e^-$ sample is affected, mostly due to changing numbers of electons being removed by muons in the overlap removal step and by the di-lepton veto. The muon trigger efficiency has a relative uncertainty of 1%.

For τ_{had} candidates a relative identification efficiency uncertainty of 9.1% is obtained for all regions of phase space. In addition, the efficiency of true electrons to be mis-identified as τ_{had} candidates needs to be corrected in the simulation in dependence of the electron veto used. For the W + jets and QCD multi-jet backgrounds the uncertainties due to the τ_{had} identification are estimated by varying the other backgrounds accordingly and propagating the changes to the background estimates. The correction factors used for the BDT electron veto used in this analysis (see Section 5.2.4) are shown in Table 7.3. The effect of these τ_{had} identification uncertainties on the event yield can be found in Table 7.2 as well.

	Electron ID	Muon ID	τ_{had} ID	Electron as τ_{had} Mis-ID
Signal (m_A = 120 GeV)	0.8	0.2	9.1	0.4
Diboson	1.0	0.2	9.1	0.5
W + jets	0.8	0.4	1.4	0.6
$Z/\gamma^* \to e^+e^-$	3.8	2.1	9.1	4.8
$Z/\gamma^* \to \mu^+\mu^-$	0.8	0.3	9.1	0.4
$Z/\gamma^* \to \tau^+\tau^-$	0.8	0.2	9.1	0.4
Top	0.8	0.2	9.1	0.3
QCD multi-jet	0.8	0.6	5.7	1.3

Table 7.2: Effect on the event yield in % of the electron, muon, τ_{had} identification ("ID") uncertainties and the uncertainty of the mis-identification of electrons as τ_{had} candidates for an example signal sample, simulated background samples, the $Z/\gamma^* \to \tau^+\tau^-$ embedding sample and the QCD multi-jet sample estimated from data.

	$\lvert\eta\rvert < 1.37$	$1.37 \geq \lvert\eta\rvert < 1.52$	$\lvert\eta\rvert > 1.52$
Correction Factor	0.98 ± 0.30	1.0 ± 1.0	1.59 ± 0.66

Table 7.3: Correction factors for the electron as τ_{had} mis-identification efficiency, when using the BDT electron veto.

7.2 Background Estimation Uncertainties

7.2.1 Embedding Uncertainties

The systematic uncertainties of the embedding method are estimated by using alternative event samples with varied settings (see Section 6.1).

The variations are:

- **Isolation:** The muons that are replaced by τ_{had} candidates are not required to be isolated in the standard embedding procedure. For this variation the sum of all tracks with $p_{\text{T}} > 1$ GeV in a cone of radius $\Delta R = 0.2$ around the muon's direction is required to be less then 20% of its track transverse momentum.
- **Muon energy:** For this variation, instead of removing all calorimeter energy within a cone of radius $\Delta R = 0.1$ around the (to be replaced) muon's direction, no energy is removed.

Requiring isolation leads to a 3.4% decrease in the yield of the $Z/\gamma^* \rightarrow \tau^+\tau^-$ embedding sample, while not removing the muon energy decreases the yield by 3.3%. In addition, changes in the embedding procedure indirectly influence the QCD multi-jet estimate as $Z/\gamma^* \rightarrow \tau^+\tau^-$ embedding events are subtracted in the control regions, used for the multi-jet estimate. The yield increases by 3.7% and 4.4% for the isolation and the muon energy variations, respectively. The W + jets estimate is not influenced, as it is performed at an earlier selection step where $Z/\gamma^* \rightarrow \tau^+\tau^-$ from simulation is used. In Figure 7.2 comparisons of the MMC mass distributions for the nominal embedding settings, the isolation change and the muon energy change are shown. While the effect on shape of the MMC mass distribution is negligible for the QCD multi-jet estimate, it will be propagated to the final limit for the $Z/\gamma^* \rightarrow \tau^+\tau^-$ embedding sample.

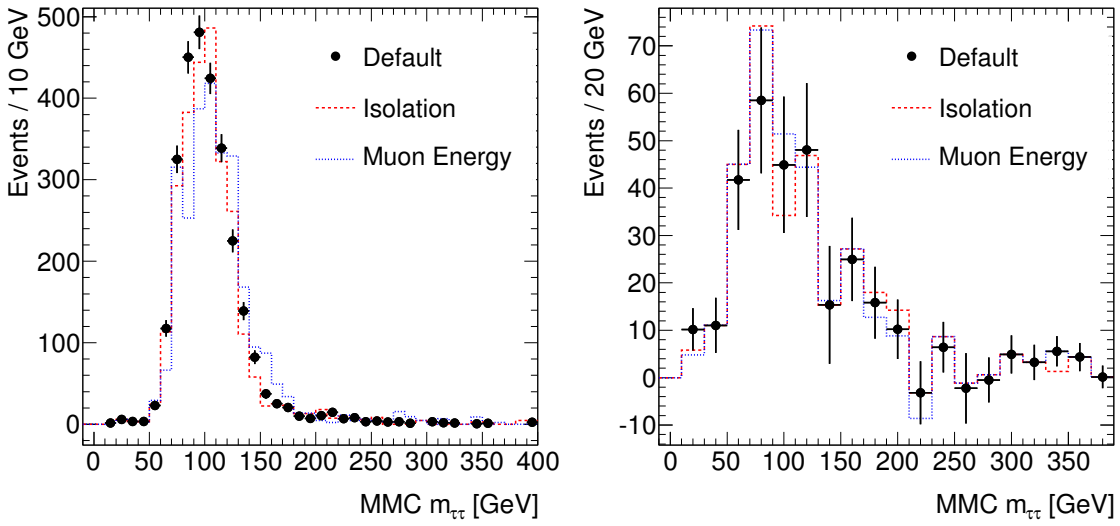

(a) $Z/\gamma^* \rightarrow \tau^+\tau^-$ (b) QCD multi-jet

Figure 7.2: Comparison of the MMC mass distribution with the nominal embedding settings, the isolation change and the muon energy change. The distributions are shown for the $Z/\gamma^* \rightarrow \tau^+\tau^-$ embedding sample (left) and the QCD multi-jet samples obtained from data (right).

7.2.2 W + Jets Normalization Uncertainty

The uncertainties of the normalization correction factors estimated for the W + jets background (see Equation 6.1) are considered by varying the factors within their uncertainties. This leads to a 4.1% uncertainty on the W + jets event yield. As the QCD multi-jet estimation depends on the W + jets event yield in the control regions the normalization variation results in a 4.2% uncertainty on the QCD multi-jet event yield.

7.3 Theory and Monte Carlo Modeling Uncertainties

Both the theoretical cross section calculations and the simulation of the signal and background processes carry uncertainties. The uncertainties of the individual theoretical inclusive cross sections are obtained by varying the renormalization and factorization scales (μ_R, μ_F) by factors of $\frac{1}{2}$ and 2, the strong coupling constant α_S and the PDF sets within their uncertainties. The QCD multi-jet estimate from data and the W + jets normalization depend on the normalization of the other backgrounds and therefore they are affected by this theory uncertainty as well.

The acceptance uncertainty is estimated by a variation of μ_R and μ_F, the ALPGEN matching parameters and by changing the default PDF(MSTW2008) to MRST2001J [82]. This is performed using simulated[2] samples [6] and therefore the effect on the QCD multi-jet background estimated from data and the W + jets normalization that depends on the full simulation of the other background samples cannot be assessed. However, the effect of the acceptance uncertainties is assumed to be of smaller or similar size as the uncertainty due to the cross sections and therefore to be negligible when compared to the much larger jet energy scale uncertainty. In Table 7.4 the effect of these variations on the yields of an example signal sample, the simulated backgrounds and the background samples estimated from data is presented.

7.4 Luminosity Uncertainty

The integrated luminosity uncertainty is 3.7% [84] and it is taken into account for all background samples taken from simulation. The QCD multi-jet and the W + jets backgrounds are only affected indirectly, as the contents of the control regions change. This results in a 2.3% (0.6%) uncertainty for the QCD multi-jet (W + jets) background.

7.5 Summary of Systematic Uncertainties

An overview of all systematic uncertainties considered and their effect on the event yield for all samples is given in Table 7.4.

The large uncertainties on the $Z/\gamma^* \to e^+e^-$ sample is unproblematic as the event yield of this sample is very small. The uncertainty on the QCD multi-jet estimate are large, as the uncertainties on all other samples are propagated to it, and as it is estimated from data with a limited statistical precision. The estimated number of QCD multi-jet events, including systematic uncertainties, is

$$n_{\mathrm{A}}^{\text{QCD multi-jet}} = 308 \pm 37^{\text{stat.}} \pm 95^{\text{syst.}} = 308 \pm 102. \tag{7.1}$$

[2]These samples are produced using the fast ATLAS simulation ATLFAST II [83].

where the total systematic $\sigma^{\text{total}}_{\text{syst.}}$ is given by the single systematic uncertainties added in quadrature, with the energy scale and resolution uncertainties symmetrized and the total uncertainty is given as $\sqrt{(\sigma^{\text{total}}_{\text{syst.}})^2 + (\sigma_{\text{stat.}})^2}$.

The effect of the jet/τ_{had} energy scale uncertainty dominates the overall uncertainties especially for the signal sample and the $Z/\gamma^* \rightarrow \tau^+\tau^-$ embedding sample[3] which constitutes a large background contribution. In addition, it leads to significant differences of the shape of the MMC mass distribution that need to be considered for the final limit estimation (see Chapter 8). The final estimate for the $Z/\gamma^* \rightarrow \tau^+\tau^-$ background yield is:

$$n^{Z/\gamma^* \rightarrow \tau^+\tau^-} = 2790 \pm 49^{\text{stat.}} \pm 781^{\text{syst.}} = 2790 \pm 783, \tag{7.2}$$

while the result for the estimated W + jets background yield is

$$n^{W+\text{jets}} = 467 \pm 20^{\text{stat.}} \pm 65^{\text{syst.}} = 467 \pm 68. \tag{7.3}$$

Assuming the uncertainties to be uncorrelated the total expected background event yield is $4151 \pm 66^{\text{stat.}} \pm 792^{\text{syst.}} = 4151 \pm 795$. In the statistical methods presented in the next Chapter 8 the correlations between the uncertainties for all samples will be taken into account properly, i.e. the jet energy scale uncertainty is treated as being correlated for all samples.

	Signal	Diboson	W + jets	$Z \rightarrow ee$	$Z \rightarrow \mu\mu$	$Z \rightarrow \tau\tau$	Top	QCD
$\sigma_{\text{inclusive}}$	12.4	7	0.5	5	5	5	10	2.7
Acceptance	7	2	-	14	14	14	2	-
e Efficiency	0.8	1.0	0.8	3.8	0.8	0.8	0.8	0.8
μ Efficiency	0.2	0.2	0.4	2.1	0.3	0.2	0.2	0.6
τ_{had} Eff./Mis-ID	9.1	9.1	1.5	10.3	9.1	9.1	9.1	5.8
Energy Scale/Reso.	$^{+17}_{-13}$	13	$^{+11}_{-14}$	$^{+37}_{-26}$	$^{+24}_{-16}$	$^{+25}_{-16}$	$^{+7}_{-15}$	$^{-34}_{+25}$
W+jets Normalization	-	-	4.1	-	-	-	-	4.2
Embedding	-	-	-	-	-	4.7	-	5.7
Luminosity	3.7	3.7	0.6	3.7	3.7	3.7	3.7	2.3
$\sigma^{\text{total}}_{\text{syst.}}$	23	18	14	37	27	28	18	31
$\sigma_{\text{stat.}}$	4	6	4	6	5	2	2	12
Total Uncertainty	23	19	14	37	27	28	18	33

Table 7.4: Overview of the effect of the systematic uncertainties on the event yield in % for all samples. The signal sample is shown for $m_A = 120$ GeV and $\tan\beta = 20$. The table is divided into a theory, a detector, a background estimation and a luminosity part. The three bottom lines give the total systematic $\sigma^{\text{total}}_{\text{syst.}}$, the statistic $\sigma_{\text{stat.}}$ and the total uncertainties.

[3]Note: Without the embedding method, relying on simulation only, the effect of the jet energy scale uncertainty would have to be considered as well and the uncertainty on the $Z/\gamma^* \rightarrow \tau^+\tau^-$ sample would be even bigger.

Chapter 8

Statistical Interpretation and Exclusion Limits

No significant excess of data events compared with the Standard Model prediction is observed in the MMC $m_{\tau\tau}$ distribution (see Figures 6.10 and 7.1). Therefore, exclusion limits on the Higgs boson production are set at the 95% confidence level. The statistical method applied in the following is the profile likelihood method [85] based on the CL_s parameter [86, 87] from an analysis of the MMC $m_{\tau\tau}$ distribution. In the following the methods are briefly introduced and the resulting exclusion limits are presented.

8.1 The Profile Likelihood Method

8.1.1 Test Statistic and Likelihood Function

In order to apply the CL_s method a test statistic, q, used to distinguish between the hypothesis that the data contain signal and background ($s + b$) and the background-only hypothesis (b) is defined in terms of a likelihood function L. It takes the systematic uncertainties of the measurement into account. The Likelihood is given by:

$$L\left(\mathbf{n}|\mu, \mathbf{s}, \mathbf{b}, \boldsymbol{\theta}\right) = \prod_i P\left(n_i|\lambda_i\left(\mu \cdot s_i, b_i, \boldsymbol{\theta}\right)\right) \times \prod_j P_{\text{Syst}}\left(\theta_j, \theta_j^0\right) \tag{8.1}$$

where $\mathbf{n}$ is the measured distribution in the signal region, i.e. a vector with each of its elements representing one of the bins i of the MMC $m_{\tau\tau}$ distribution in the signal region, $\mathbf{s}$ and $\mathbf{b}$ are for the expected signal and background distribution in the signal region, accordingly. The parameter μ is the signal strength[1] and $\boldsymbol{\theta}$ represents the nuisance parameters[2] that parametrize the systematic uncertainties. The first term $P\left(n_i|\lambda_i\right)$ is the Poisson probability of observing n_i events given an expectation of $\lambda_i\left(\mu \cdot s_i, b_i, \boldsymbol{\theta}\right)$ events. The expected λ_i depends on the number of the expected signal events, $\mu \cdot s_i$, for a given signal strength μ, the expected background b_i and the nuisance parameters $\boldsymbol{\theta}$. The second term P_{Syst} takes the systematic uncertainties, in the form of the nuisance parameters θ_j, into account. The nuisance parameters are allowed to vary around their nominal value θ_i^0 according to a Gaussian distribution with a width corresponding to their uncertainty.

Suppressing all parameters but μ and $\boldsymbol{\theta}$ for simplicity, one specific test statistic $\tilde{q}_\mu$ is defined as

$$\tilde{q}_\mu = -2 \ln \frac{L(\mu, \hat{\hat{\boldsymbol{\theta}}}(\mu))}{L(\hat{\mu}, \hat{\boldsymbol{\theta}})}, \tag{8.2}$$

[1] $\mu = 1$ corresponds to the $s + b$ hypothesis with nominal signal strength and $\mu = 0$ corresponds to the background-only hypothesis.

[2] There are j nuisance parameters.

where $\hat{\mu}$ and $\hat{\boldsymbol{\theta}}$ maximize L unconditionally and $\hat{\hat{\boldsymbol{\theta}}}(\mu)$ maximizes L for any given μ. The expression is only valid for $0 \leq \hat{\mu} \leq \mu$. It is called profile log likelihood ratio, hence the name profile likelihood method. In the following the test statistic $\tilde{q}_\mu$ is used. To simplify the notation and as the next subsection is also true for other test statistic definitions, the notation q is used in the following.

8.1.2 The CL$_s$ Technique

With a test statistic q given, a so-called p-value can be constructed. It is defined as the probability, assuming a hypothesis H is correct, to observe data with equal or lesser compatibility to H than the measured data. The tested hypotheses are the null or background-only hypothesis b and the signal plus background hypothesis $s + b$. An example of the distribution of q under the two hypotheses $f(q|b)$ and $f(q|s + b)$ is given in Figure 8.1.

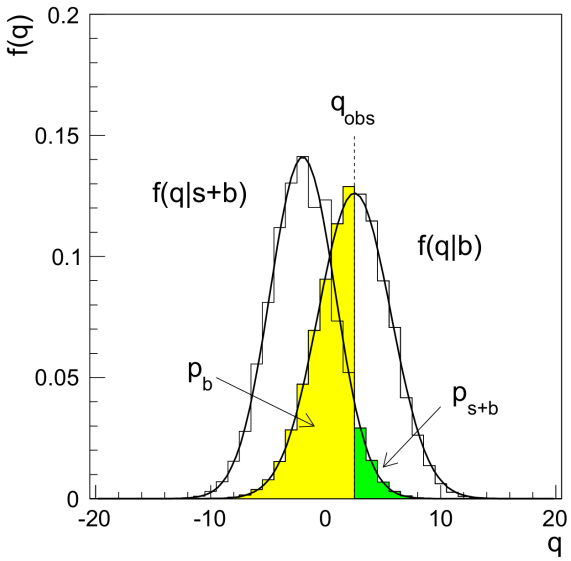

Figure 8.1: Distribution of the test statistic variable q assuming the $s + b$ and b hypothesis [88]. The p-values for the two hypotheses, as defined in equations 8.3 and 8.4, correspond to the yellow and green areas.

In this example, assuming an observed value of q_{obs} the p-value of the $s + b$ hypothesis is the probability to find a q greater than or equal to q_{obs} under the assumption of the $s + b$ hypothesis

$$p_{s+b} = P(q \geq q_{\text{obs}}|s + b) = \int_{q_{\text{obs}}}^{\infty} f(q|s + b)dq. \tag{8.3}$$

Similarly, the p-value of the background-only hypothesis is

$$p_b = P(q < q_{\text{obs}}|b) = \int_{-\infty}^{q_{\text{obs}}} f(q|b)dq. \tag{8.4}$$

The p-value p_{s+b} can be used to test the hypothesis e.g. to exclude it at a confidence level of $1-\alpha = 95\%$ if $p_{s+b} < \alpha$. A problem arises with this so-called CL$_{s+b}$ method if the sensitivity to the hypothesis is low or non-existent. This is illustrated in Figure 8.2.

For example if the expected number of signal events n_s is much smaller than the expected number of background events n_b, i.e. $n_b \gg n_s$ and if then the observed number of events due to statistical

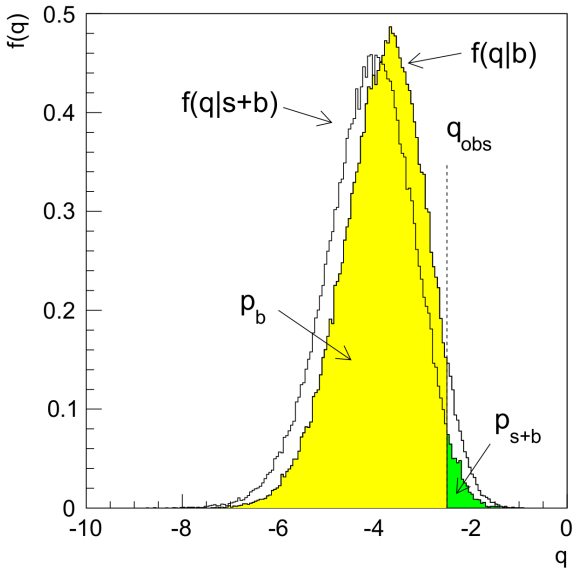

Figure 8.2: Distribution of the test statistic q assuming the $s+b$ and b hypothesis [88]. An experiment less sensitive to the hypothesis than the one illustrated in Figure 8.1 is indicated. The p-values for the two hypotheses, as defined in equations 8.3 and 8.4, correspond to the yellow and green areas.

fluctuations is smaller than the expected number $n_s + n_b$ (which is $\approx n_b$) this value of n_s leads to an exclusion, while intuitively one would like the probability to make an exclusion to be zero in this case.

In order to not exclude models that one is not sensitive to, the CL_s method is used. It excludes a signal model if

$$CL_s = \frac{p_{s+b}}{1 - p_b} < \alpha, \tag{8.5}$$

thus penalizing the p-value p_{s+b} by dividing it by $1 - p_b$, which is close to unity if the distributions $f(q|s + b)$ and $f(q|b)$ are well separated, i.e. the experiment is sensitive to the hypotheses. However, if the experiment is not sensitive and hence the distributions are close together $1 - p_b$ becomes small and the value of CL_s is increased, and therefore no exclusion can be made. In that sense the CL_s method is the more conservative method compared to the CL_{s+b} method as it excludes only a subset of the hypotheses that the later would exclude.

The distributions of q for various hypotheses can be obtained by simulating many experiments or by using asymptotic formulae, if the number of events in the signal region is sufficient, which is the case in this analysis.

8.2 Exclusion Limits

Using the methods described in Section 8.1 the MMC $m_{\tau\tau}$ distribution of the estimated backgrounds and the hypothetical signal are compared with the data and two different exclusion limits are set at the 95% confidence level:

1. Expected limit on the production cross section times branching ratio, $\sigma_\Phi \times BR(\Phi \to \tau\tau)$, for a generic Higgs boson Φ as a function of its mass m_Φ. The limit is shown for the gluon fusion and the b-associated production processes separately.

2. Exclusion limit in the $\tan\beta$-m_A plane in the MSSM interpretation.

8.2.1 Limit on the Cross Section Times Branching Ratio

Upper limits on the cross section times branching ratio $\sigma_\Phi \times BR(\Phi \to \tau\tau)$ as a function of the Higgs boson mass m_Φ are calculated for both production processes separately, assuming only one generic Higgs boson Φ. These results are independent of the MSSM theory predictions. In Figure 8.3 the resulting expected and observed limits for the gluon fusion and the b-associated production processes are shown. In addition, the expected limits from the summer 2011 analysis [7] that was performed with an integrated luminosity of 1fb^{-1} and the Standard Model theory prediction are shown for comparison. Besides the $m_\Phi = 100$ GeV point, where the b-associated production sample suffers from large statistical uncertainties, both production processes give similar results, as expected since the signal acceptance for both production processes is similar. An additional comparison of the limits for the two processes is shown in Figure A.1, where the resulting limits are shown separately, including the $\pm 1\sigma$ and $\pm 2\sigma$ uncertainties on the expected limits. The uncertainties are correlated to a large degree as the same background predictions and uncertainties are used. The difference between the two production processes is small.

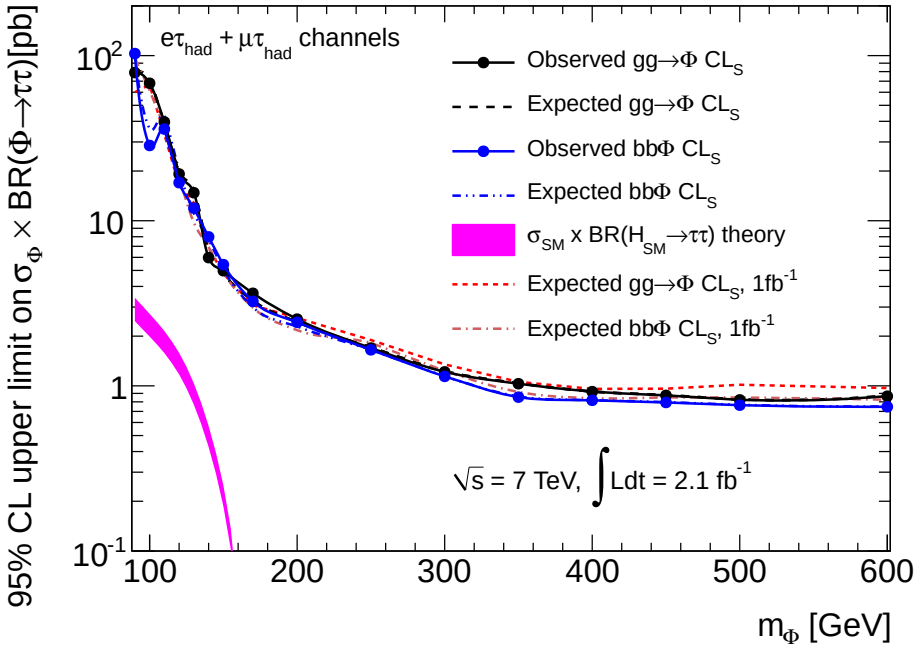

Figure 8.3: Upper limit on the production cross section times branching ratio, $\sigma_\Phi \times BR(\Phi \to \tau\tau)$, in dependence of the mass of a generic Higgs boson, m_Φ, at 95 % confidence level for the gluon fusion and the b-associated production processes. The black (blue) dashed and full lines are the expected and observed limit for the gluon fusion (b-associated) production process. For comparison, the expected limits from the summer 2011 analysis [7] (red/brown dashed) that was performed with an integrated luminosity of 1fb^{-1} are given, as well as the prediction for the Standard Model Higgs boson (magenta).

A nuisance parameter is defined for each of the systematic uncertainties[3] described in Section 8.1. The nuisance parameters are allowed to vary to find the smallest value of the log likelihood ratio.

[3] As a reminder: Included are uncertainties due to theory predictions, e.g. on the cross sections used, due to detector and reconstruction effects, e.g. on the jet energy scale, identification of τ_{had} candidates, due to the background estimates, e.g. the uncertainty on the QCD multi-jet estimate and due to the uncertainty on the luminosity.

In Figure 8.4 distributions of a few example nuisance parameters as a function of $\sigma_\Phi \times BR(\Phi \to \tau\tau)$ are shown for the point where the mass of the generic Higgs boson Φ is assumed to be $m_\Phi = 120$ GeV (more distributions are shown in Figure A.2). On the one hand the influence of the jet energy scale uncertainty is bigger than the one of the other two examples, i.e. the uncertainty on the τ_{had} identification and the inclusive Z cross section, and varies the most with changing signal strength $\sigma_\Phi \times BR(\Phi \to \tau\tau)$, on the other hand the uncertainty on the τ_{had} identification and the inclusive Z cross section have a much smaller impact on the exclusion limit and do not vary as much. None of the distributions show any pathological behavior, e.g. large fluctuations or discontinuities, indicating that the fitting procedure works. Accordingly the resulting log likelihood ratio in dependence of $\sigma_\Phi \times BR(\Phi \to \tau\tau)$ presented in Figure 8.5 looks as expected. This validates the limit setting procedure.

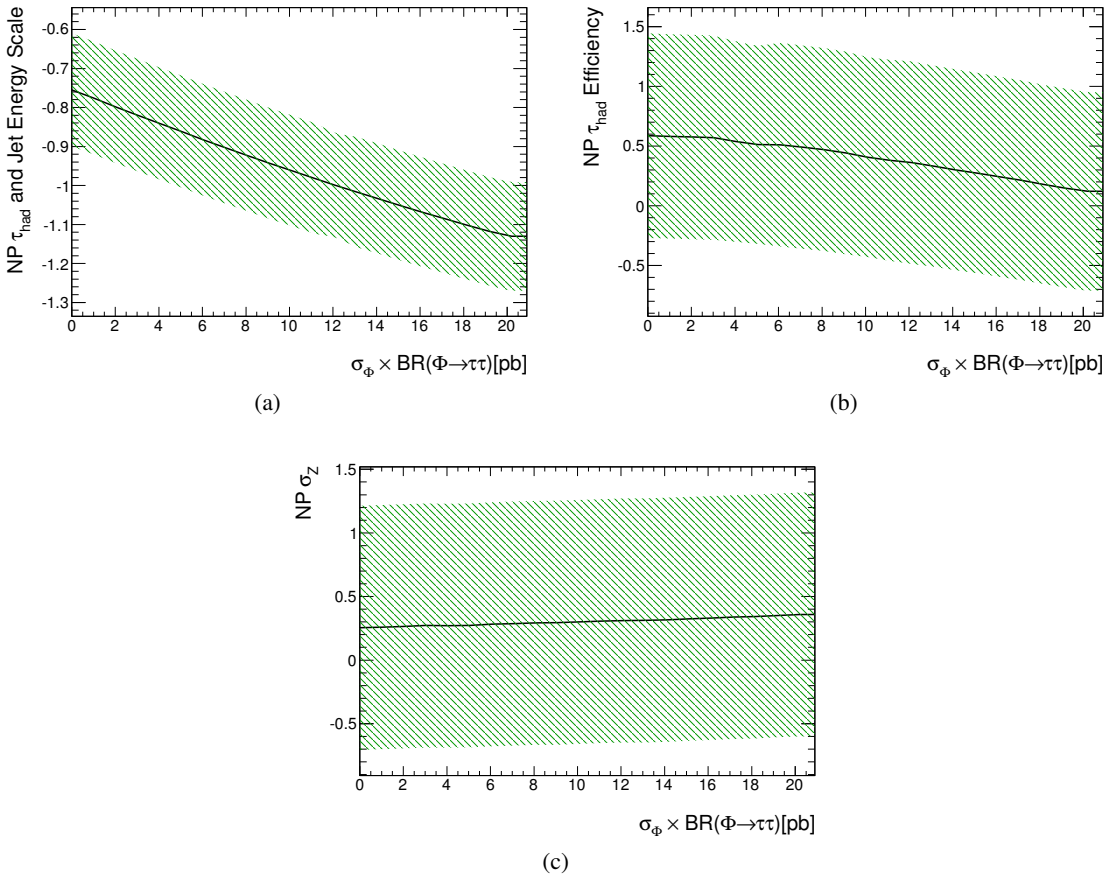

Figure 8.4: Distributions of fitted nuisance parameters (in units of standard deviations) as a function of $\sigma_\Phi \times BR(\Phi \to \tau\tau)$ for the limit on the generic Higgs boson Φ at a mass of $m_\Phi = 120$ GeV, including uncertainties (green band). The distributions shown are for the uncertainty on the jet energy scale (a), the τ_{had} identification efficiency (b) and the inclusive Z cross section (c).

Compared with the summer 2011 results the limits seem not to have improved by much, even though the integrated luminosity has doubled. This is mostly due to a change in the limit setting procedure. For the 2011 results it ignored statistical uncertainties of the background estimates. To illustrate the effect, the 1fb^{-1} expected limits compared with the 2.1fb^{-1} ones but with the statistical uncertainties of the backgrounds ignored for the later are shown in Figure 8.6. The new limits are improved for high masses

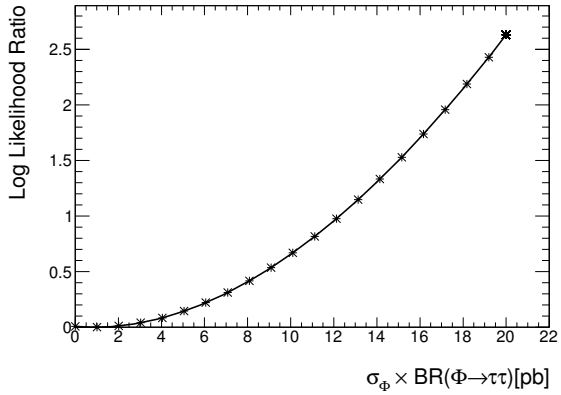

Figure 8.5: Distribution of the log likelihood ratio as a function of $\sigma_\Phi \times BR(\Phi \rightarrow \tau\tau)$ for the limit on the generic Higgs boson Φ at a mass of $m_\Phi = 120$ GeV.

m_Φ while they are comparable for low masses, where the systematic uncertainties from the $Z/\gamma^* \rightarrow \tau^+\tau^-$ background are dominant.

No useful constraints on the Standard Model prediction are possible, as the limits are more than a factor of ten away from the predicted value of $\sigma_\Phi \times BR(\Phi \rightarrow \tau\tau)$ for the Standard Model Higgs boson. The analysis has not been designed for the Standard Model Higgs search and newer results specifically aiming for discovering the Standard Model Higgs boson in the di-τ channel have recently been made public by ATLAS [89]. No significant excess over the expected background has been reported in this channel yet.

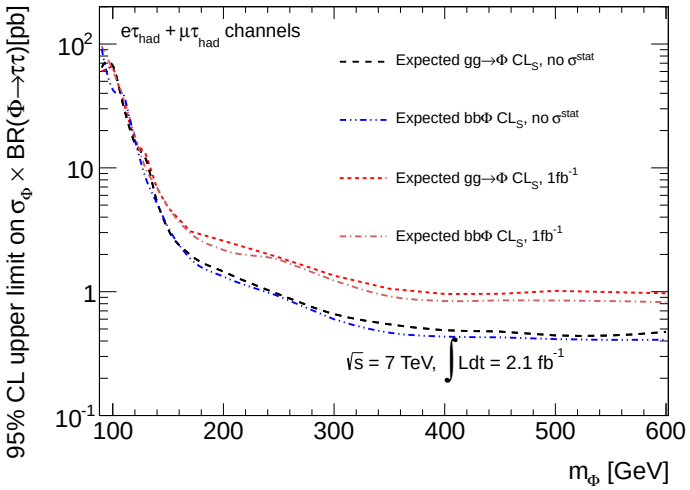

Figure 8.6: Expected upper limit on the production cross section times branching ratio, $\sigma_\Phi \times BR(\Phi \rightarrow \tau\tau)$, in dependence of the mass of a generic Higgs boson, m_Φ, at 95 % confidence level for the gluon fusion (black) and the b-associated (blue) production processes with an integrated luminosity of 2.1fb^{-1} and for the summer 2011 analysis [7] (gluon fusion in red, b-associated production in brown) that was performed with an integrated luminosity of 1fb^{-1}. The statistical uncertainties of the background estimation are neglected for the 2.1fb^{-1} analysis as well.

8.2.2 MSSM Limit

The MSSM interpretation of the results is presented in Figure 8.7. Shown are the limits in the m_A-$\tan\beta$ plane in the m_A range of 100 GeV to about 450 GeV in the $m_h^{\max}$ scenario. The observed and the expected limit with its $\pm 1\sigma$ and $\pm 2\sigma$ uncertainty are presented. For comparison, the expected limit from the summer 2011 analysis [7], and limits observed in direct searches by the LEP experiments [31] are shown (due to the changes discussed in the previous section the limit is not improved much compared to the previous results). Values of $\tan\beta$ ranging as low as 15 are excluded and the result is shown up to masses m_A of 420 GeV. For masses above $m_A \approx 400$ GeV the observed limit is above $\tan\beta = 60$, usually considered the highest $\tan\beta$ value allowed by theory. The LEP results exclude a complementary region at low values of $\tan\beta$. Checks on the limit setting procedure similar to the ones discussed in Section 8.2.1 have been performed and the resulting validation distributions can be found in Appendix A.

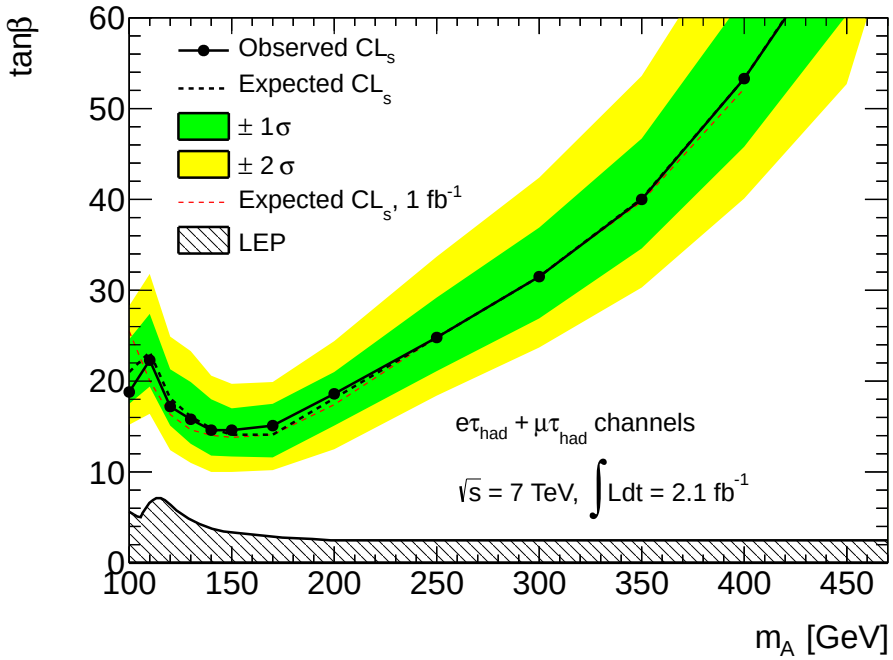

Figure 8.7: Expected and observed upper limits in the $\tan\beta$-m_A plane in the $m_h^{\max}$ scenario at 95 % confidence level. The black hashed and full lines are the expected and observed limit, the green and yellow bands are the $\pm 1\sigma$ and $\pm 2\sigma$ uncertainties on the expected limits, respectively. For comparison the expected limit from the summer 2011 analysis [7] (red) and the LEP limit [31] are given.

In Figures 8.8 and 8.9 similar exclusion limits from the combined results of the D0 and CDF experiments at the Tevatron [90] and from CMS [91] are shown. The results from the Tevatron are based on $p\bar{p}$ collision data corresponding to 1.8fb^{-1} and 2.2fb^{-1} of integrated luminosity collected with the CDF and D0 experiments at a center-of-mass energy of 1.96 TeV. The $e\tau_{\text{had}}$, $\mu\tau_{\text{had}}$ and the $e\mu$ final states were analyzed. The limit set by CMS shown in Figure 8.9 is based on an analysis using data corresponding to an integrated luminosity of 4.6fb^{-1} and reconstructing the $e\tau_{\text{had}}$, $\mu\tau_{\text{had}}$ and the $e\mu$ final states.

Since ATLAS aims at producing updates of the MSSM Higgs analysis quickly as the recorded ATLAS dataset increases, during the time of writing this thesis already the preliminary results of an analysis using the full 2011 dataset have recently been published [92]. The dataset used is equivalent to 4.7 –

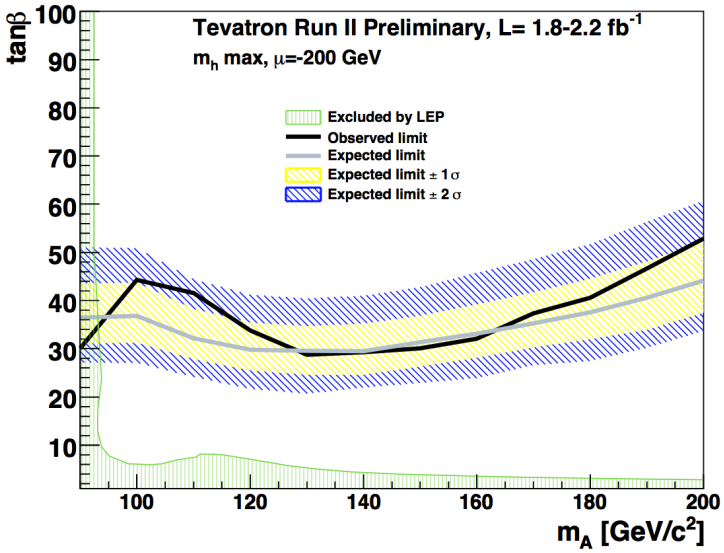

Figure 8.8: Expected and observed upper limits in the $\tan\beta$-m_A plane in the m_h^{max} scenario from the Tevatron experiments [90] at 95 % confidence level. The blue and black lines are the expected and observed limit, the yellow and blue bands are the $\pm 1\sigma$ and $\pm 2\sigma$ uncertainties on the expected limits, respectively. The LEP limit [31] is given in green.

4.8fb^{-1}, depending on the decay channel. While the analysis shares some features with this analysis it uses more channels ($e\tau_{\text{had}}$, $\mu\tau_{\text{had}}$, $e\mu$, $\mu\mu$ and $\tau_{\text{had}}\tau_{\text{had}}$) and is no longer jet inclusive, as it separates final states with and without b quarks using b tagging. The exclusion limits in the $\tan\beta$-m_A plane are shown in Figure 8.10.

In summary, the methods developed and the results obtained in this thesis have been important contributions to MSSM searches at the LHC and to the first exclusion limits on MSSM Higgs production at ATLAS resulting in limits that are significant improvements compared with previous results from LEP and the Tevatron experiments.

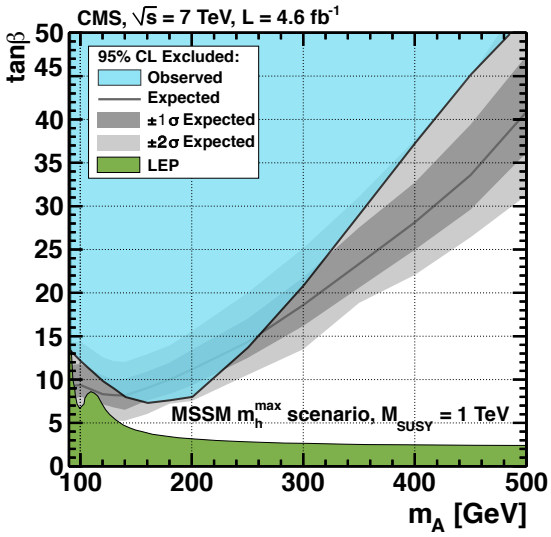

Figure 8.9: Expected and observed upper limits in the $\tan\beta$-m_A plane in the $m_h^{\max}$ scenario from the CMS experiment [91] at 95 % confidence level. The blue area is the observed excluded area, the fine black line is the expected limit with its $\pm1\sigma$ and $\pm2\sigma$ uncertainties indicated by the two grey bands. The LEP limit [31] is given in green.

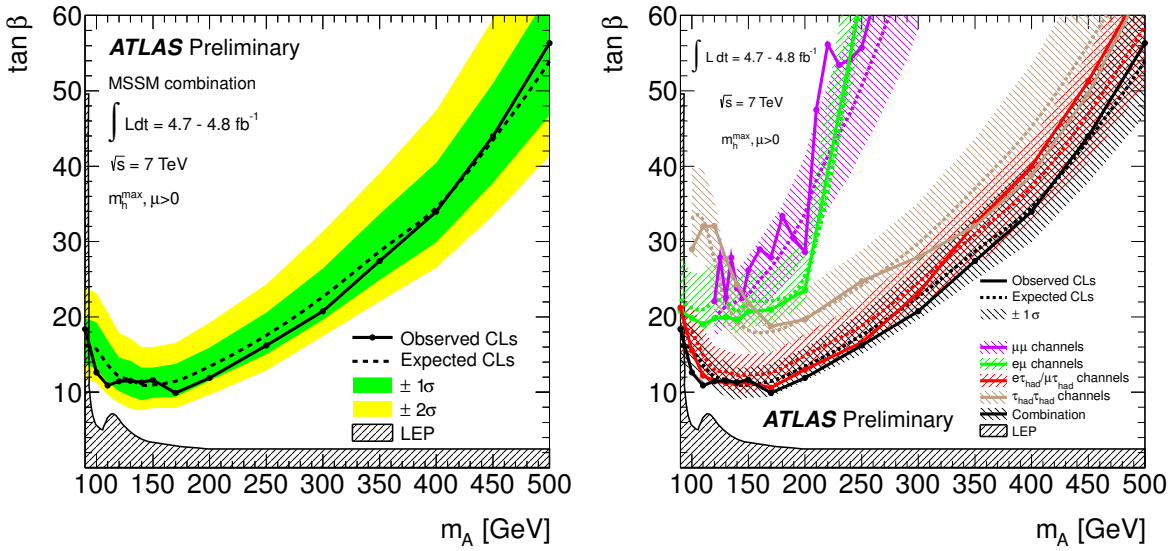

Figure 8.10: Latest expected (dashed black line) and observed (solid black line) upper limits in the $\tan\beta$-m_A plane in the $m_h^{\max}$ scenario from the ATLAS experiment [92] at 95 % confidence level using a dataset with an integrated lumiosity of $4.7-4.8\text{fb}^{-1}$. In the left figure the green and yellow bands are the $\pm1\sigma$ and $\pm2\sigma$ uncertainties on the expected limits, respectively. In the right figure the contributing channels are presented separately.

Chapter 9

Conclusions

In this thesis, a search for neutral MSSM Higgs bosons decaying into pairs of τ leptons has been presented. One of the final state τ leptons is reconstructed in a leptonic decay channel, the other in a hadronic one. The analysis has contributed to the first ATLAS result in this search channel using LHC data that was obtained on a dataset corresponding to an integrated luminosity of 36pb^{-1} and an update of it that has used a larger dataset (1fb^{-1}). In the course of this analysis, the dataset has been extended to a total integrated luminosity of 2.1fb^{-1}.

An event selection that relies on the identification of hadronically decaying τ leptons has been introduced. In total 4065 data events have been selected and the total signal selection efficiency has been estimated to be $\approx 0.7\%$ for $m_A = 120\,\text{GeV}$ and $\tan\beta = 20$. The di-τ mass is reconstructed using a novel likelihood based method [76] that takes the undetectable neutrinos into account via the missing transverse energy $E_{\text{T}}^{\text{miss}}$.

The contributions of the main background processes have been estimated using data driven methods. For the $Z/\gamma^* \rightarrow \tau^+\tau^-$ background an embedding method has been used that replaces the muons in reconstructed $Z/\gamma^* \rightarrow \mu^+\mu^-$ events with simulated τ leptons. The event yield of the W + jets background has been studied in a sideband control region and the simulation has been normalized to agree with the sideband data. The contribution from QCD multi-jet processes has been estimated from three data control regions.

Systematic uncertainties due to these background estimates have been identified and studied as well as systematic uncertainties affecting the simulated signal and background event samples. The dominating systematic uncertainty is due to the uncertainty on the energy scales of jets and τ_{had} candidates.

As no excess over the expected backgrounds has been observed, exclusion limits have been set on the $\sigma_\Phi \times BR(\Phi \rightarrow \tau\tau)$ of a generic Higgs boson Φ in dependence of its mass, m_Φ, and in the MSSM interpretation, i.e. in the m_A-$\tan\beta$ plane. The statistical treatment has been improved compared to the previous publications and the exclusion limits are stronger.

Results from ATLAS and CMS that use larger datasets have recently improved these limits. Due to the larger sample size these analyses can divide the signal region further, e.g. into regions differing by the number of reconstructed b jets. Thus these analyses can even more exploit features of the specific signal topologies, e.g. by reconstructing at least one of the b jets in the bbA final state.

Recent results from measurements of B-meson decays with $D^{(*)}\tau\nu$ final states [93] seem to disagree with the expectations from the Standard Model at the 3.4 σ level. A charged Higgs boson H^+ can potentially contribute to these decays. However, the excess cannot be explained by the charged Higgs boson within the Type-II two Higgs doublet models like the MSSM. The Belle collaboration has not yet published any results on this topic. A current theory publication [94] considers a possible explanation of the disagreement with the Standard Model with Type-III two Higgs doublet models. Therefore it is still useful to look for heavy Higgs bosons, in particular when exclusion limits on $\sigma_\Phi \times BR(\Phi \rightarrow \tau\tau)$ in dependence of the mass of a generic Higgs boson for different production processes are set, as presented in this thesis.

In the light of the recent discovery of a new particle with a mass of about 125 GeV by ATLAS [4] and CMS [5], which is so far consistent with a Standard Model Higgs boson, searches for the Standard Model Higgs boson in the di-τ final state are very important, as currently the evidence for the new particle has only been found in bosonic final states, e.g. $H \to \gamma\gamma$, $H \to ZZ$ and $H \to W^+W^-$. Therefore scenarios involving a fermiophobic Higgs boson [95–97], i.e. one that couples less strongly or not at all to fermions, cannot be excluded yet. As the Standard Model Higgs boson couples stronger to b quarks and τ leptons than to the much lighter fermions, the experimentally challenging $H \to b\bar{b}$ and the $H \to \tau^+\tau^-$ channels have the largest discovery or exclusion potential.

In summary, the work presented here has been an important part of one of the first searches for physics beyond the Standard Model using ALTAS data. The applied methods proved ground for current and future searches for di-τ resonances. Given the recent discovery of a new particle and the increasing dataset provided by the LHC, the next years will be very exciting for particle physics. The search for heavy non-Standard Model Higgs bosons will continue to be important to show if nature provides one or several Higgs bosons.

Appendix

Appendix A

Additional Limit Setting Validation Figures

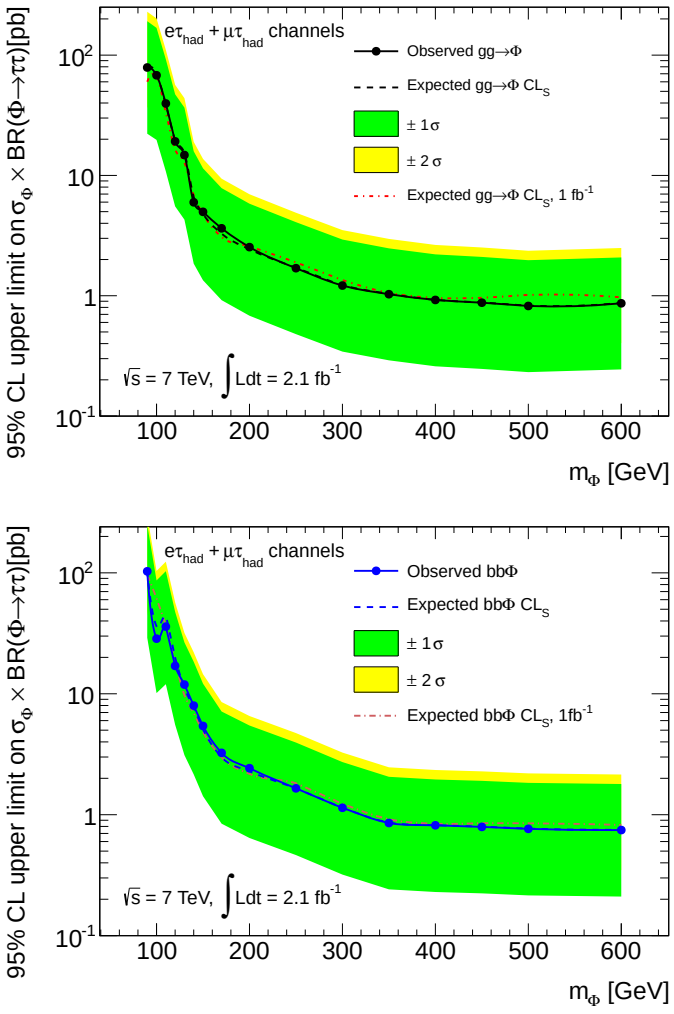

Figure A.1: Upper limit on the production cross section times branching ratio, $\sigma_\Phi \times BR(\Phi \to \tau\tau)$, in dependence of the mass of a generic Higgs boson, m_Φ, for the gluon fusion (top) and the b-associated (bottom) production processes. The black (blue) dashed and full lines are the expected and observed limit for the gluon fusion (b-associated) production process. The green and yellow bands are the $\pm 1\sigma$ and $\pm 2\sigma$ uncertainties on the expected limits, respectively. For comparison the expected limit from the summer 2011 analysis [7] (red) that was performed with an integrated luminosity of 1fb^{-1} is given.

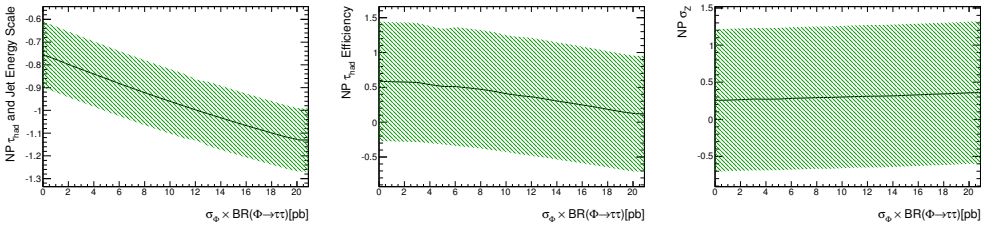

(a) Jet/τ_{had} energy scale (b) τ_{had} identification efficiency (c) σ_{Z}

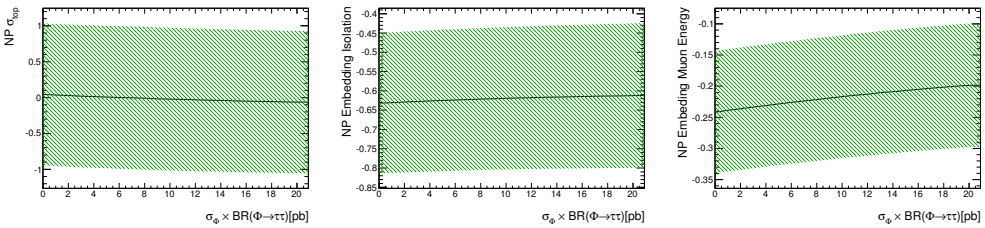

(d) σ_t (e) Embedding isolation (f) Embedding muon energy

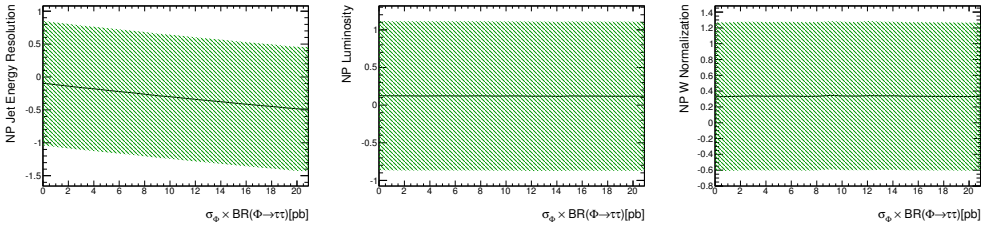

(g) Jet energy resolution (h) Luminosity (i) W + jets normalization

Figure A.2: Selected distributions of fitted nuisance parameters as a function of $\sigma_\Phi \times BR(\Phi \to \tau\tau)$ for the limit on the generic Higgs boson Φ at a mass of $m_\Phi = 120$ GeV, including uncertainties (green band).

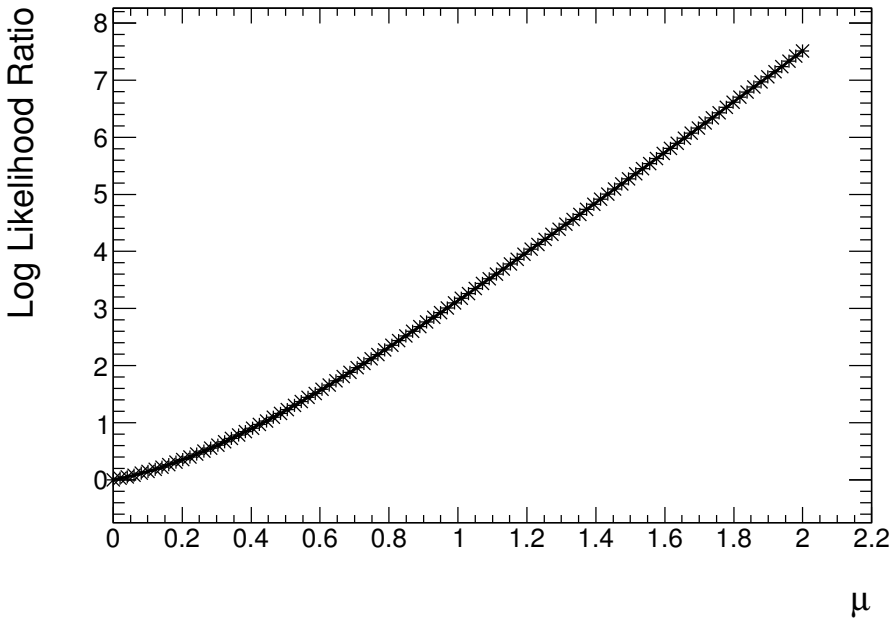

Figure A.3: Distribution of the log likelihood ratio in dependence of the signal strength μ for the MSSM limit interpretation, for $m_A = 120$ GeV and $\tan\beta = 20$.

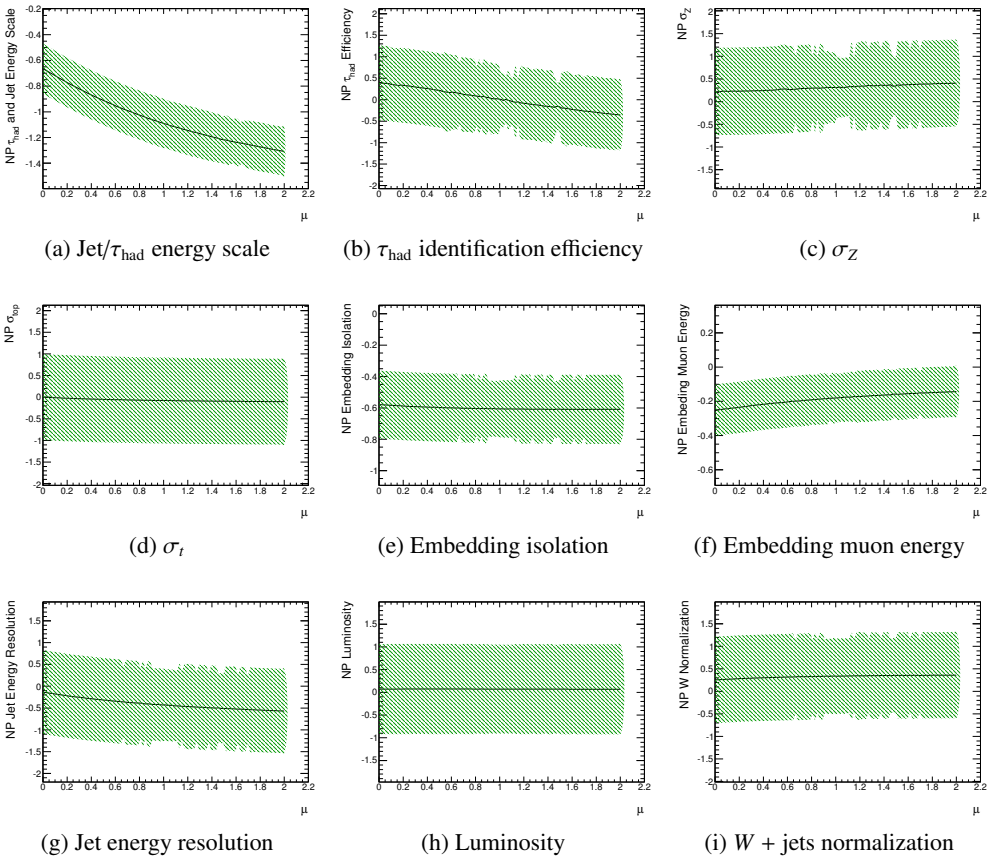

(a) Jet/τ_{had} energy scale (b) τ_{had} identification efficiency (c) σ_{Z}

(d) σ_t (e) Embedding isolation (f) Embedding muon energy

(g) Jet energy resolution (h) Luminosity (i) W + jets normalization

Figure A.4: Selected distributions of fitted nuisance parameters as a function of the signal strength μ for the limit in the MSSM interpretation, with $m_A = 120$ GeV and $\tan\beta = 20$, including uncertainties (green band).

Bibliography

[1] S. Abachi et al. 'Search for High Mass Top Quark Production in $p\overline{p}$ Collisions at $\sqrt{s} = 1.8$ TeV'. In: *Phys. Rev. Lett.* 74 (13 1995), pp. 2422–2426.

[2] F. Abe et al. 'Observation of Top Quark Production in $\overline{p}p$ Collisions with the Collider Detector at Fermilab'. In: *Phys. Rev. Lett.* 74 (14 1995), pp. 2626–2631.

[3] K. Kodama et al. 'Observation of tau neutrino interactions'. In: *Phys. Lett.* B504 (2001), pp. 218–224.

[4] The ATLAS Collaboration. 'Observation of a new particle in the search for the Standard Model Higgs boson with the ATLAS detector at the LHC'. In: *Phys. Lett.* B716 (2012), pp. 1–29.

[5] The CMS Collaboration. 'Observation of a new boson at a mass of 125 GeV with the CMS experiment at the LHC'. In: *Phys. Lett.* B716 (2012), pp. 30–61.

[6] The ATLAS Collaboration. 'Search for neutral MSSM Higgs bosons decaying to $\tau^+ \tau^-$ pairs in proton-proton collisions at $\sqrt{s} = 7$ TeV with the ATLAS detector'. In: *Phys. Lett.* B705 (2011), pp. 174–192.

[7] The ATLAS Collaboration. 'Search for neutral MSSM Higgs bosons decaying to $\tau^+\tau^-$ pairs in proton-proton collisions at $\sqrt{s} = 7$ TeV with the ATLAS detector'. ATLAS-CONF-2011-132. 2011.

[8] A. Djouadi. 'The Anatomy of electro-weak symmetry breaking. I: The Higgs boson in the standard model'. In: *Phys. Rept.* 457 (2008), pp. 1–216.

[9] A. Djouadi. 'The Anatomy of electro-weak symmetry breaking. II. The Higgs bosons in the minimal supersymmetric model'. In: *Phys. Rept.* 459 (2008), pp. 1–241.

[10] F. Englert and R. Brout. 'Broken Symmetry and the Mass of Gauge Vector Mesons'. In: *Phys. Rev. Lett.* 13 (9 1964), pp. 321–323.

[11] P. W. Higgs. 'Broken symmetries, massless particles and gauge fields'. In: *Phys. Lett.* 12 (1964), pp. 132–133.

[12] P. W. Higgs. 'Broken Symmetries and the Masses of Gauge Bosons'. In: *Phys. Rev. Lett.* 13 (1964), pp. 508–509.

[13] P. W. Higgs. 'Spontaneous Symmetry Breakdown without Massless Bosons'. In: *Phys. Rev.* 145 (1966), pp. 1156–1163.

[14] G. S. Guralnik, C. R. Hagen and T. W. B. Kibble. 'Global Conservation Laws and Massless Particles'. In: *Phys. Rev. Lett.* 13 (20 1964), pp. 585–587.

[15] J. Goldstone, A. Salam and S. Weinberg. 'Broken Symmetries'. In: *Phys. Rev.* 127 (3 1962), pp. 965–970.

[16] 'LEP Design Report: Vol. 2. The LEP Main Ring'. 1984.

[17] LEP Collaborations: ALEPH Collaboration, DELPHI Collaboration, L3 Collaboration, OPAL Collaboration, the LEP Electroweak Working Group, the SLD Electroweak, Heavy Flavour Groups. 'A Combination of Preliminary Electroweak Measurements and Constraints on the Standard Model'. hep-ph/0412015. 2004.

[18] T. Hambye, K. Riesselmann. 'Matching conditions and Higgs mass upper bounds revisited'. In: *Phys. Rev.* D55 (1997), pp. 7255–7262.

[19] Nilles, H. P. 'Dynamically Broken Supergravity and the Hierarchy Problem'. In: *Phys. Lett.* B115 (1982), p. 193.

[20] A. H. Chamseddine, R. Arnowitt and Pran Nath. 'Locally Supersymmetric Grand Unification'. In: *Phys. Rev. Lett.* 49.14 (1982), p. 970.

[21] E. Cremmer, Pierre Fayet and L. Girardello. 'Gravity Induced Supersymmetry Breaking and Low-Energy Mass Spectrum'. In: *Phys. Lett.* B122 (1983), p. 41.

[22] M. Dine and W. Fischler. 'A Phenomenological Model of Particle Physics Based on Supersymmetry'. In: *Phys. Lett.* B110 (1982), p. 227.

[23] L. Alvarez-Gaume, M. Claudson and M. B. Wise. 'Low-Energy Supersymmetry'. In: *Nucl. Phys.* B207 (1982), p. 96.

[24] Chiara R. Nappi and Burt A. Ovrut. 'Supersymmetric Extension of the $SU(3) \times SU(2) \times U(1)$ Model'. In: *Phys. Lett.* B113 (1982), p. 175.

[25] M. Dine and A. E. Nelson. 'Dynamical supersymmetry breaking at low-energies'. In: *Phys. Rev.* D48 (1993), pp. 1277–1287.

[26] M. Dine, A. E. Nelson and Y. Shirman. 'Low-energy dynamical supersymmetry breaking simplified'. In: *Phys. Rev.* D51 (1995), pp. 1362–1370.

[27] M Dine et al. 'New tools for low-energy dynamical supersymmetry breaking'. In: *Phys. Rev.* D53 (1996), pp. 2658–2669.

[28] S. P. Martin. 'A Supersymmetry primer'. hep-ph/9709356. 1997.

[29] M. Carena, S. Heinemeyer, C. E. M. Wagner, and G. Weiglein. 'Suggestions for benchmark scenarios for MSSM Higgs boson searches at hadron colliders'. In: *Eur. Phys. J.* C26 (2003), p. 601.

[30] F. Zwirner. 'The quest for low-energy supersymmetry and the role of high-energy e+ e- colliders'. hep-ph/9203204. 1991.

[31] ALEPH Collaboration, DELPHI Collaboration, L3 Collaboration, OPAL Collaboration, the LEP Higgs Working Group. 'Searches for the neutral Higgs bosons of the MSSM: Preliminary combined results using LEP data collected at energies up to 209-GeV'. hep-ex/0107030. 2001.

[32] K. Nakamura et al. (Particle Data Group). 'The Review of Particle Physics'. In: *J. Phys. G 37, 075021* (2010).

[33] I. Brock and T. Schörner-Sadenius. *Physics at the Terascale*. Wiley-VCH, 2011.

[34] P. M. Nadolsky et al. 'Implications of CTEQ global analysis for collider observables'. In: *Phys. Rev.* D78 (2008), p. 013004.

[35] A. D. Martin et al. 'Parton distributions for the LHC'. In: *Eur. Phys. J.* C63 (2009), pp. 189–285.

[36] J. M. Campbell et al. 'Hard Interactions of Quarks and Gluons: A Primer for LHC Physics'. In: *Rept. Prog. Phys.* 70 (2007), p. 89.

[37] M. Cacciari, G. P. Salam and G. Soyez. ‘ The anti-k_t jet clustering algorithm ’. In: *JHEP* 04 (2008), p. 063.

[38] M. Cacciari and G. P. Salam. ‘Dispelling the N^3 myth for the k_t jet-finder’. In: *Phys. Lett. B* 641 (2006), p. 57.

[39] O. S. Brüning et al. ‘LHC Design Report’. CERN-2004-003-V-1. 2004.

[40] The ATLAS Collaboration. ‘ATLAS: Technical proposal for a general-purpose pp experiment at the Large Hadron Collider at CERN’. CERN-LHCC-94-43. 1994.

[41] The CMS Collaboration. ‘CMS, the Compact Muon Solenoid : Technical proposal’. CERN-LHCC-94-38. 1994.

[42] The LHCb Collaboration. ‘LHCb : Technical Proposal’. CERN-LHCC-98-004. 1998.

[43] The ALICE Collaboration. ‘ALICE: Technical proposal for a Large Ion collider Experiment at the CERN LHC’. CERN-LHCC-95-71. 1995.

[44] P. Braun-Munzinger and J. Stachel. ‘The quest for the quark–gluon plasma’. In: *Nature* 448 (2007).

[45] P. Mouche. ‘Overall view of the LHC. Vue d’ensemble du LHC’. 2006. URL: `http://cdsweb.cern.ch/record/987579/`.

[46] The ATLAS Collaboration. ‘ATLAS Experiment at the CERN Large Hadron Collider’. In: *JINST 3* (2008).

[47] The GEANT4 Collaboration, S. Agostinelli et al. In: *Nucl. Instrum. Meth.* A506 (2003), p. 250.

[48] The ATLAS Collaboration. ‘The ATLAS Simulation Infrastructure’. In: *Eur. Phys. J.* C70 (2010), pp. 823–874.

[49] M. Frank et al. ‘The Higgs Boson Masses and Mixings of the Complex MSSM in the Feynman-Diagrammatic Approach’. In: *JHEP* 0702 (2007), p. 047.

[50] S. Dittmaier et al. ‘Handbook of LHC Higgs Cross Sections: 1. Inclusive Observables’. hep-ph/1101.0593. 2011.

[51] S. Alioli et al. ‘Higgs boson production in gluon fusion’. In: *JHEP* 02 (2009), p. 029.

[52] T. Gleisberg et al. ‘Event generation with SHERPA 1.1’. In: *JHEP* 0902 (2009), p. 007.

[53] M. Spira. ‘HIGLU: A program for the calculation of the total Higgs production cross-section at hadron colliders via gluon fusion including QCD corrections’. hep-ph/9510347. 1995.

[54] Harlander, R. and Kilgore, W. B. ‘Next-to-next-to-leading order Higgs production at hadron colliders’. In: *Phys. Rev. Lett.* 88 (2002), p. 201801.

[55] S. Kramer M. Dittmaier and M. Spira. ‘Higgs radiation off bottom quarks at the Tevatron and the CERN LHC’. In: *Phys. Rev.* D70 (2004), p. 074010.

[56] S. Dawson, C. B. Jackson, L. Reina and D. Wackeroth. ‘Higgs production in association with bottom quarks at hadron colliders’. In: *Mod. Phys. Lett.* A21 (2006), pp. 89–110.

[57] R. Harlander and W. B. Kilgore. ‘Higgs boson production in bottom quark fusion at next-to-next-to leading order’. In: *Phys. Rev.* D68 (2003), p. 013001.

[58] R. Harlander, M. Kramer and M. Schumacher. ‘Bottom-quark associated Higgs-boson production: reconciling the four- and five-flavour scheme approach’. hep-ph/1112.3478. 2011.

[59] M. L. Mangano et al. 'ALPGEN, a generator for hard multiparton processes in hadronic collisions'. In: *JHEP* 0307 (2003), p. 001.

[60] S. S. Frixione and B. R. Webber. 'Matching NLO QCD computations and parton shower simulations'. In: *JHEP* 0206 (2002), p. 029.

[61] B.P. Kersevan and E.Richter-Was. 'The Monte Carlo event generator AcerMC version 2.0 with interfaces to PYTHIA 6.2 and HERWIG 6.5'. hep-ph/0405247. 2004.

[62] G. Corcella et al. et al. 'HERWIG 6: An Event generator for hadron emission reactions with interfering gluons (including supersymmetric processes)'. In: *JHEP* 0101 (2001), p. 010.

[63] T. Binoth et al. 'Gluon-induced W-boson pair production at the LHC'. In: *JHEP* 0612 (2006), p. 046.

[64] J. M. Butterworth, J. R. Forshaw and M. H. Seymour. 'Multiparton interactions in photoproduction at HERA'. In: *Z. Phys.* C72 (1996), pp. 637–646.

[65] S. Jadach, Z. Was, R. Decker and J. H. Kuhn. 'The tau decay library TAUOLA: Version 2.4'. In: *Comput. Phys. Commun.* 76 (1993), pp. 361–380.

[66] P. Golonka, B. Kersevan, T. Pierzchala, E. Richter-Was, Z. Was and M. Worek. 'The Tauola photos F environment for the TAUOLA and PHOTOS packages: Release. 2.' In: *Comput. Phys. Commun.* 174 (2006), pp. 818–835.

[67] E. Barberio and Z. Was. 'PHOTOS: A Universal Monte Carlo for QED radiative corrections. Version 2.0'. In: *Comput. Phys. Commun.* 79 (1994), pp. 291–308.

[68] The ATLAS Collaboration. 'Expected electron performance in the ATLAS experiment'. ATL-PHYS-PUB-2011-006. 2011.

[69] The ATLAS Collaboration. 'Electron performance measurements with the ATLAS detector using the 2010 LHC proton-proton collision data'. In: *Eur.Phys.J.* C72 (2012), p. 1909.

[70] The ATLAS Collaboration. https://twiki.cern.ch/twiki/bin/view/AtlasPublic/Muon Performance-PublicPlots.

[71] W. Lampl et al. 'Calorimeter Clustering Algorithms : Description and Performance'. ATL-LARG-PUB-2008-002. 2008.

[72] The ATLAS Collaboration. 'Performance of the Reconstruction and Identification of Hadronic Tau Decays with ATLAS'. ATLAS-CONF-2011-152. 2011.

[73] A. Hoecker et al. 'TMVA: Toolkit for Multivariate Data Analysis'. In: *PoS* ACAT (2007), p. 040.

[74] The ATLAS Collaboration. 'Measurement of the $W \to \ell\nu$ and $Z/\gamma^* \to \ell\ell$ production cross sections in proton-proton collisions at $\sqrt{s}$ = 7 TeV with the ATLAS detector'. In: *JHEP* 1012 (2010), p. 060.

[75] The ATLAS Collaboration. 'Expected Performance of the ATLAS Experiment - Detector, Trigger and Physics'. hep-ex/0901.0512. 2009.

[76] A. Elagin et al. 'A New Mass Reconstruction Technique for Resonances Decaying to di-tau'. In: *Nucl. Instrum. Meth.* A654 (2011), pp. 481–489.

[77] The ATLAS Collaboration. 'Reconstruction and Calibration of Missing Transverse Energy and Performance in Z and W events in ATLAS Proton-Proton Collisions at 7 TeV'. ATLAS-CONF-2011-080. 2011.

[78] The ATLAS Collaboration. 'Muon Momentum Resolution in First Pass Reconstruction of pp Collision Data Recorded by ATLAS in 2010'. ATLAS-CONF-2011-046. 2011.

[79] The ATLAS Collaboration. 'Jet energy scale and its systematic uncertainty in proton-proton collisions at $\sqrt{(s)}$ = 7 TeV in ATLAS 2010 data'. ATLAS-CONF-2011-032. 2011.

[80] The ATLAS Collaboration. 'Validating the measurement of jet energies with the ATLAS detector using Z + jet events from proton-proton collisions at $\sqrt{s}$ = 7 TeV'. ATLAS-CONF-2011-159. 2011.

[81] The ATLAS Collaboration. 'Performance of the Missing Transverse Energy Reconstruction and Calibration in Proton-Proton Collisions at a Center-of-Mass Energy of 7 TeV with the ATLAS Detector'. ATLAS-CONF-2010-057. 2010.

[82] A.D. Martin, R.G. Roberts, W.J. Stirling, R.S. Thorne, 'MRST2001: Partons and α_s from precise deep inelastic scattering and Tevatron jet data'. In: *Eur. Phys. J.* C23 (2002), pp. 73–87.

[83] The ATLAS Collaboration. 'The ATLAS Simulation Infrastructure'. In: *Eur. Phys. J. C70* (2010).

[84] The ATLAS Collaboration. 'Luminosity Determination in pp Collisions at $\sqrt{(s)}$ = 7 TeV using the ATLAS Detector in 2011'. ATLAS-CONF-2011-116. 2011.

[85] G. Cowan, K. Cranmer, E. Gross and O. Vitells. 'Asymptotic formulae for likelihood-based tests of new physics'. In: *Eur. Phys. J.* C71 (2011), p. 1554.

[86] T. Junk. 'Confidence level computation for combining searches with small statistics'. In: *Nucl. Instrum. Meth.* A434 (1999), pp. 435–443.

[87] A. L. Read. In: *J. Phys.* G28 (2002), p. 2693.

[88] ATLAS Statistics Forum. 'The CLs method: information for conference speakers'. 2011.

[89] The ATLAS Collaboration. 'Search for the Standard Model Higgs boson in the H to $\tau^+\tau^-$ decay mode in $\sqrt{s}$ = 7 TeV pp collisions with ATLAS'. In: *JHEP* 1209 (2012), p. 070.

[90] The CDF Collaboration, The D0 Collaboration, The Tevatron New Physics Higgs Working Group (TEVNPHWG). 'Combined CDF and D0 upper limits on MSSM Higgs boson production in tau-tau final states with up to 2.2 fb-1'. hep-ex/1003.3363v3. 2010.

[91] The CMS Collaboration. 'Search for neutral Higgs bosons decaying to tau pairs in pp collisions at $\sqrt{s}$=7 TeV'. hep-ex/1202.4083. 2012.

[92] The ATLAS Collaboration. 'Search for Neutral MSSM Higgs bosons in $\sqrt{s}$ = 7 TeV pp collisions at ATLAS'. ATLAS-CONF-2012-094. 2012.

[93] J.P. Lees et al. 'Evidence for an excess of $\bar{B} \to D^{(*)}\tau^-\bar{\nu}_\tau$ decays'. In: *Phys. Rev. Lett.* 109 (2012), p. 101802.

[94] A. Crivellin, C. Greub and A. Kokulu. 'Explaining $B \to D\tau\nu$, $B \to D^*\tau\nu$ and $B \to \tau\nu$ in a 2HDM of type III'. In: *Phys. Rev.* D86 (2012), p. 054014.

[95] A. Barroso, L. Brucher and R. Santos. 'Is there a light fermiophobic Higgs?' In: *Phys. Rev.* D60 (1999), p. 035005.

[96] J. F. Gunion, R. Vega and J. Wudka. 'Higgs triplets in the standard model'. In: *Phys. Rev. D* 42 (5 1990), pp. 1673–1691.

[97] A. G. Akeroyd et al. 'Fermiophobia in a Higgs triplet model'. In: *Phys. Rev. D* 83 (9 2011), p. 095003.

List of Figures

List of Tables

Acknowledgements

Während der Jahre meiner Promotion bin ich vielen Menschen begegnet. Ich möchte mich hier bei allen bedanken, die ich in dieser Zeit kennenlernen durfte.

Ich bedanke mich besonders bei meinem Doktorvater Prof. Dr. Jochen Dingfelder für die Überlassung des Themas, für Erreichbarkeit und Engagement zu jeder Zeit, so wie für die stetige Motivation und immer gute Zusammenarbeit!
Des Weiteren danke ich Prof. Dr. Klaus Desch dafür, dass er sich die Zeit genommen hat, als Gutachter meine Arbeit zu bewerten.

Für die freundliche Aufnahme in ihren Gruppen danke ich Prof. Dr. Hans-Christian Schultz-Coulon, Prof. Dr. Karl Jakobs und Prof. Dr. André Schöning.

Mein Dank gilt außerdem allen Kollegen und Freunden, denen ich auf meinen Stationen in Heidelberg, Freiburg und Bonn und in der ATLAS Kollaboration begegnet durfte. Leider seid ihr zu viele um euch alle einzeln nennen zu können.
Direkt beteiligt am Erfolg meiner Arbeit und deswegen hier gesondert erwähnt: Sascha – Codinggenie; Markus und Julian – Limitexperten; Felix und Stefan – Hauptkorrekturleser; Michel – Büroteiler. Bei euch fand ich immer Unterstützung und Rat!

All das wäre natürlich nicht möglich ohne privaten Rückhalt, deswegen möchte ich meiner Familie, besonders meinen Eltern und meiner Ann-Marie danken!